REMOTE SENSING OF THE UPPER TROPOSPHERIC STATE OF STORMS USING SPACE-BORNE HIGH SPECTRAL RESOLUTION INFRARED MEASUREMENTS

by

Chian-Yi Liu

A dissertation submitted in partial fulfillment of
the requirements for the degree of

Doctor of Philosophy
(Atmospheric and Oceanic Sciences)

at the

UNIVERSITY OF WISCONSIN-MADISON

2010

ProQuest LLC
789 East Eisenhower Parkway
P.O. Box 1346
Ann Arbor, MI 48106-1346

A dissertation entitled

REMOTE SENSING OF THE UPPER TROPOSPHERIC STATE OF STORMS USING SPACE-BORNE HIGH SPECTRAL RESOLUTION INFRARED MEASUREMENTS

submitted to the Graduate School of the
University of Wisconsin-Madison
in partial fulfillment of the requirements for the
degree of Doctor of Philosophy

by

Chian-Yi Liu

Date of Final Oral Examination: 23 April 2010

Month & Year Degree to be awarded: **December** **May** **August** **2010**

****

Approval Signatures of Dissertation Committee

Wolfgang Paul Menzel

Matthew H. Hitchman

Ralph Bonnarty

Signature, Dean of Graduate School

Martin Cadwallader

Committee's Page. This page is not to be hand-written except for the signatures

Abstract

An investigation of the upper tropospheric state of the storm is conducted using space-borne high spectral resolution infrared remote sensing data. This is accomplished through an approach that synergistically uses an advanced sounder and a high spatial resolution imager, such as the Atmospheric Infrared Sounder (AIRS) and Moderate Resolution Imaging Spectroradiometer (MODIS), respectively. The cloud-free AIRS footprints are less than 10% globally, and the MODIS can be utilized to ensure optimal cloud-clearing of AIRS observation. This greatly improves the likelihood that atmospheric sounding retrievals will be cloud-free or cloud-corrected if it is partly cloudy. A case study shows that more than 24% of AIRS cloudy footprints are successfully cloud-cleared, which demonstrates the advantage of applying the optimal cloud-clearing approach. The successful rate is achieved in greater than 40% of partly cloudy footprints.

Analyzing the state of upper troposphere (UT) in clear or clear-equivalence footprints may not represent the UT structure completely. Therefore, the clear and cloudy soundings are developed and enhanced by synergistically using collocated MODIS clear-sky data as well. Evaluation of the retrieved profile is performed by comparisons between AIRS soundings, model analysis fields, and radiosonde observations. The results of these comparisons demonstrate the advantage of a synergistic use of AIRS and MODIS over using either system alone.

One month of collocated AIRS and MODIS data, along with hourly precipitation record, are analyzed using the enhanced synergistic retrieval procedure. It is found that a pre-existing

low UT stability is highly correlated with the subsequent mesoscale convection 6- to 12-hr later. Also a relatively low UT stability in the storm area, compared to the ambient area, shows no statistically significant change over time. Stronger mesoscale storm activities, in terms of more intense precipitation and greater coverage, are associated with lower UT stability. This may give a possible explanation for nocturnal convection without well defined boundary-layer forcing. Furthermore, the use of high spectral resolution observations is a more effective detection scheme for the troposphere penetrating convection (TPC) compared to using observations from a broadband imager. The estimated precipitation intensity using collocated imager data within the identified TPC footprints is in good agreement with past studies.

Acknowledgments

First and foremost I would like to sincerely thank my research and academic advisors, Dr. Jun Li and Professor Steven A. Ackerman, for providing me the chance to pursue my Ph.D., and for their guidance, inspiration, patience, and trust throughout every stage of the process. Whenever I meet problem and feel frustrated, my advisors always give me support, discussion, encouragement, suggestions, and confidence. It would not be possible for me to realize my dream, being a Ph.D., without my advisors' effort.

I sincere thanks also go to one of my committee, Professors Ralf Bennartz, Matt Hitchman, W. Paul Menzel, and Pao-Kuan Wang. With their valuable comments and insight on my research during these years, and consistent warm encouragement, I made important breakthrough in this dissertation.

Drs. Elisabeth Weisz, Jinlong Li, Zhenglong Li, Xin Jin are all appreciated because they constantly help the only Ph.D. student in the group, who is without solid remote sensing background. I feel very fortunate having the chance to work with them in the past 6 years, and I would like to applaud them for the team work. I want to thank Maria Vasys, Connie Linehan, Don Moskowitz, and Angel Skram for their support during the past years.

I would like to express my gratitude to the following AOS, CIMSS, CWB, CMA, NOAA people for their help in all kinds of ways to the completion of this dissertation: Yinghui Liu, Mark Kulie, Brent Maddux, Aronne Merrelli, Agnes Lim, Xuanji Wang, Allen Huang, Kathy Strabala, Wenhua Wu, Hong Zhang, Longtao Wu, Wei Zhou, Wei Liu, Li Bi, Yun Liu,

Guangshang Chen, Shu Wu, Fuyao Wang, Fang Wang, Yafang Zhong, Peng Zhang, Peter K. H. Wang, Mei-Hui Liao, Chang-Hwan Park, Justin Sieglaff, Jiaxu Zhang, Shih-Hao Su, Chiou-Ju Chen, Emily Niebuhr, Hester Leung, Erin Wagner, Tim Wagner, Tom Achtor, Tim Schmit, Jim Nelson, Mat Gunshor, and Bormin Huang.

I can not thank enough to my wife, Ching-Ju Liu, for her unending supports, sacrifice and endless love. Her patient and supports always give me confidence. Last, but not the least, I would like to express my sincere gratitude to my parents for their patience with me.

Financial support for this research was by NOAA GOES-R program NA06NES4400002 at CIMSS.

Dedication

For my wife, for her love and understanding,

and my parents, who always made me believe I could succeed.

Table of Contents

List of Tables

List of Figures

Chapter 1 Introduction

Short-range forecasting (< 12-hr) of mesoscale storm systems is one of the most challenging problems in meteorology. Storms develop quickly and appear throughout the year over many parts of the globe [*Barnes* 2001]. They cause more than 400 deaths as well as about two to five billion dollars of economic losses in the United States annually [*Moller*, 2001; *Riebsame et al.*, 1986]. Those numbers increase if storm-induced hail, high wind, lightening and flash flooding statistics are included. The initiation of convective storms by an organized line of convergence in the boundary layer has been recognized for some time. Geostationary satellite imagery, ground-based radar observations and surface weather stations have enabled detailed studies of the role of large scale forcing and surface convergence in convective initiation of mesoscale storm systems [*Purdom*, 1976; *Purdom*, 1982; *Wilson and Schreiber*, 1986]. The state of upper troposphere (UT) and its relationship with the pre-storm environment has not received as much attention. This is primarily because of the sparse temporal and spatial distribution of radiosonde observations and the relatively low UT resolution in numerical models.

Although the *in-situ* observations of the UT are mainly conducted by routine launching of the radiosondes, the utilizing of satellite data and products become an important method to further explore the UT. Since September 2002, the high-spectral resolution infrared measurements from the Atmospheric Infrared Sounder (AIRS; http://airs.jpl.nasa.gov/) onboard National Aeronautics and Space Administration's (NASA's) Earth Observation System (EOS) *Aqua* satellite cover the 3.7 – 15.4 μm spectral region with 2378 spectral channels and a spectral

resolution of $\nu/\Delta\nu = 1200$, where ν is the wavenumber and $\Delta\nu$ is the width of a band. The AIRS has more than 100 times the resolving power of previous satellite borne IR sounders such as High Resolution Infrared Sounder (HIRS) and Geostationary Operational Environmental Satellite (GOES) Sounder [*Pagano et al.*, 2001], thus providing the needed global observations to retrieve enhanced three-dimensional maps of atmospheric thermodynamic structure and cloud properties. Therefore, AIRS provides accurate information on the vertical structure of atmospheric temperature and moisture [*Chahine et al.*, 2006]. With the improvement of atmospheric profiling algorithms in both clear and cloudy scenes (e.g., *Smith et al.* [2005]; *Weisz el al.*, [2007a, 2007b], *Liu et al.* [2008]), we have a new opportunity to study the UT atmospheric state and its relation to convective storms. In this dissertation, the state of the UT along with its signatures, in particular associate mesoscale convections, using high spectral resolution measurements are investigated. The goals are to understand the convective storm environment, identify tropopause penetrating convection (TPC), and estimate precipitation intensity of these TPCs.

The dissertation is structured as follows. Chapter 2 presents an overview of the mesoscale convection processes, focusing on the initiation stage. Chapter 3 presents a description of the instruments used in the inferring of atmospheric thermodynamic profiles. Chapter 4 introduces the handling of high spectral resolution infrared radiances including the synergistic use of high spatial resolution imager observations and derived product as part of the dissertation research. The improved retrieval algorithm is designed specifically with the inclusion of high spatial resolution imager information in the high spectral resolution measurements. Inferring atmospheric profiles using high spectral resolution infrared sounder

measurements alone, and with the inclusion of high spatial resolution imager data for the sounding enhancement are discussed in Chapter 5. The retrieved atmospheric profiles are then used to further derive the UT state. In Chapter, 6 the synergistic atmospheric retrievals are applied to AIRS and MODIS measurements over the CONUS. The pre-storm UT state, the detection of TPCs and the estimation of TPC precipitation intensity are also investigated in this chapter. Chapter 7 summarizes the dissertation results and discusses future research plans.

Chapter 2 Background

2.1 Storm Initiation Processes

Convective storms are mesoscale phenomena, and severe storms are accompanied by tornados, hailstorms, high winds or flash floods events [*Johnson and Mapes*, 2001]. While the large-scale flow establishes environmental conditions favorable for severe weather, processes of initiation and evolution of mesoscale convection are challenging problems in meteorology. A number of mesoscale processes are involved in severe weather, ranging from environmental preconditioning to storm initiation to feedback of convection on the environmental structure. The range of mesoscale processes associated with convective system is numerous. Therefore, to provide focus, this dissertation explors the mesoscale processes according to whether they are conductive generating convection (in terms of *preconditioning*), and high spectral resolution infrared spectra signatures for convections which penetrate the tropopause.

Johnson and Mapes [2001] suggested a list of common mesoscale convection preconditioning processes, which are summarized in Table 2.1. In most instances, these factors serve to gradually lower the stability in the ambient environment and modify the wind shear profile, and hence they set the stage for convective storms. They also proposed if the destabilization occurs within a rapid manner, some of these processes may actually trigger convection.

The mesoscale processes in Table 2.1 have been categorized as local, advective, and dynamical. Atmospheric boundary layer mixing, the interactions between the atmosphere and terrain, and differential boundary contrasts due to various surface properties are considered as local preconditioning processes. Advective processes consist of the transport of air masses. Advection is an important preconditioning process in the pre-storm environment (e.g., the convergence of humid air masses). Mesoscale dynamical processes are difficult distinguished from the response of synoptic-scale circulations as discussed in most studies (e.g., upper-level jet streaks and low-level jets have long been associated with convective system due to ageostrophic adjustments) [*Uccellini and Johnson*, 1979; *Bluestein and Thomas*, 1984]. These processes are important in pre-storm environments and inside the convection systems.

Table 2.1 Mesoscale preconditioning processes for convection (After *Johnson and Mapes* [2001]).

Local	Advective	Dynamical
Boundary layer processes • deepening the mixed layer • deepening the moisture layer • convergence along dryline • nocturnal inversion, low-level jet formation Terrain effects • creation of convergence zone • development of slow flows • modification of hodograph Surface effects • evaporation, heating • surface, discontinuities - soil moisture - roughness	Differential advection • creation of capping, inversion • destabilization • formation of deep, dry PBL (leading to microbursts) Convergence lines • fronts • drylines • sea/land/lake breezes • mountain/valley breezes Moisture advection • increase CAPE, lower LFC • local cumulus moistening	Secondary circulations • geostrophic adjustment • jets Gravity currents, waves • cold pool lifting • localized reduction of CIN • modification of vertical shear Mesoscale instabilities Boundary layer processes • horizontal convective rolls • inertial oscillation (low-level jets)

2.2 The Remote Sensing of Storms

Over the past several decades, there have been major advances in understanding the basic mechanisms for severe storms through observational studies and idealized numerical simulations. Despite this progress, forecasting severe storms remains a major challenge. Many of the difficulties stem from mesoscale processes being inadequately observed and not fully understood. Previous studies were based on dense networks of anemometers, such as *Byers and Braham* [1949] who observed surface convergence 30 minutes prior to radar echo appearance during the Thunderstorm Project. Rapid advances in remote sensing technologies in recent years – for example, wind profilers, surface and airborne Doppler radars, Raman lidars – have greatly enhanced our capability to observe the environment of convective storms.

The role of radars, wind profilers and surface weather measurements in observing preconditioning processes is mainly focused on the boundary convergence lines in initiating deep convection [e.g., *Wilson and Carbone*, 1984; *Szoke et al.*, 1985; *Schreiber*, 1986]. The state of UT in preconditioning processes does not receive much focus for several reasons. Sparse spatial distribution and instrumental limitations are two of them. Satellite observations may provide an opportunity to explore the upper level structure of the pre-storm environment from a top down perspective.

There are two important satellite instruments for observing and monitoring the weather and environment: the sounder and the imager. The sounder has better spectral resolution and more spectral channels for atmospheric sounding with high vertical resolution and accuracy, while the imager has finer spatial resolution and broader bands. The imager is usually applied to forest fire, clouds/fog, pollution, volcanic eruption and ice/snow cover research. The primary

application of the sounder is vertical profiling of the atmospheric soundings. *English et al.*, [2000] evaluated sounding products from the TIROS-N Operational Vertical Sounder (TOVS) [*Smith et al.*, 1979] and the Advanced TIROS Operational Vertical Sounder (ATOVS), and showed that a 20% and 5% forecast error reduction in Southern Hemisphere and Northern Hemisphere, respectively, can be achieved.

Satellite imagery, in particular from the geostationary satellite such as the Geostationary Environmental Satellite (GOES), has shown that cloud arc lines were often generated by outflows from convective storms and other convergent wind phenomena [*Purdom*, 1976, 1982; *Weaver et al.* 1994, 2000, 2002; *Bikos et al.* 2002]. The convergence lines, or arc lines, observed in the satellite imager often triggered intensive convection. *Purdom and Marcus* [1982] found that 73% of the afternoon thunderstorms in the south-eastern United States developed as the result of such interactions. Figure 2.1 shows a GOES imagery example of a storm that formed along a dryline and is moving into a region of cloud streets. The overlaid radar data conform that a well-defined mesoscale circulation is associated with the southernmost storm in this line [*Weaver and Lindsey*, 2004]. The remote sensing from both satellite and radar enables the improvement of convective storm forecasting and nowcasting capability if the atmosphere exposed in certain criteria such as that listed in Table 2.1.

With the spaceborne high spectral resolution infrared AIRS measurements, which samples at coarser spatial resolution than an imager, the chance for an AIRS footprint being completely clear is less than 10% statistically [*Huang and Smith*, 2004]. However, the UT signatures of convective storms require an accurate temperature profile from each single field-of-view under both clear and cloudy skies are desired. Proper handling of the high spectral

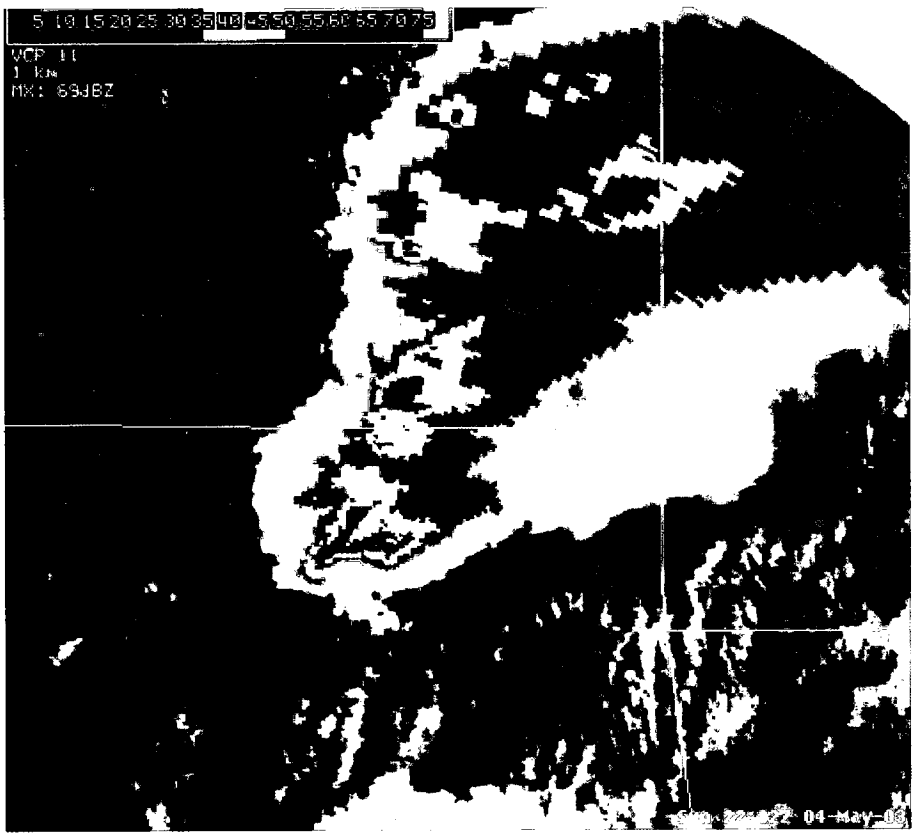

Figure 2.1 GOES visible satellite image from 2202 UTC on 4 May 2003 over northeastern Oklahoma with Tulsa, OK, WSR-88D radar base reflectivity overlaid. (After *Weaver and Lindsey*, [2004]).

resolution measurements is therefore a priority for accurate retrievals of atmospheric soundings and the inferring of the atmospheric state.

Chapter 3 Instruments, Radiance Measurement, and Radiative Transfer Models for Atmospheric Sounding Product

This chapter introduces the most used spaceborne high spectral resolution infrared sounder and high spatial resolution broadband imager on board the NASA's Earth Observing System (EOS) *Aqua* satellite, the Atmospheric Infrared Sounder (AIRS) and the Moderate Resolution Imaging Spectroradiometer (MODIS). The third of this chapter summarizes the community developed radiative transfer models, which are used for forward calculations and atmospheric sounding iterative retrievals.

3.1 The High Spectral Resolution Sounder – AIRS

The AIRS onboard the NASA's EOS Aqua satellite is a high spectral resolution infrared spectrometer/radiometer with 2378 channels. Figure 3.1 shows an example of an AIRS brightness temperature (BT) spectrum. AIRS radiances are in the infrared (IR) wavelength range between 3.74 μm – 15.4 μm (650 – 2700 cm^{-1}) [*Aumann et al.*, 2003], and the spectral coverage includes, in particular, two strong CO_2 absorption bands (near 15.5 μm and 4.3 μm), and part of the strong water vapor absorption band centered at 6.3 μm. Finite spectral signatures result from O_3, CH_4, N_2O, CO and SO_2 absorption regions. Being a grating spectrometer, the spectral resolution of AIRS is dependent on the wavelength and defined by $\nu/\Delta\nu = 1200$, where ν is the wavenumber and $\Delta\nu$ is the width of a band. The observed high spectral resolution infrared radiances enable the retrieval of vertical profiles of atmospheric temperature and water

vapor from earth's surface to an altitude of 40 km. AIRS scans the earth in the cross-track direction between ±49.5° incident angles with a swath of 1650 km, and a field-of-view (FOV) of 1.1° correlation to a nadir surface footprint of approximately 13.5 km. The Aqua satellite is in sun synchronous,

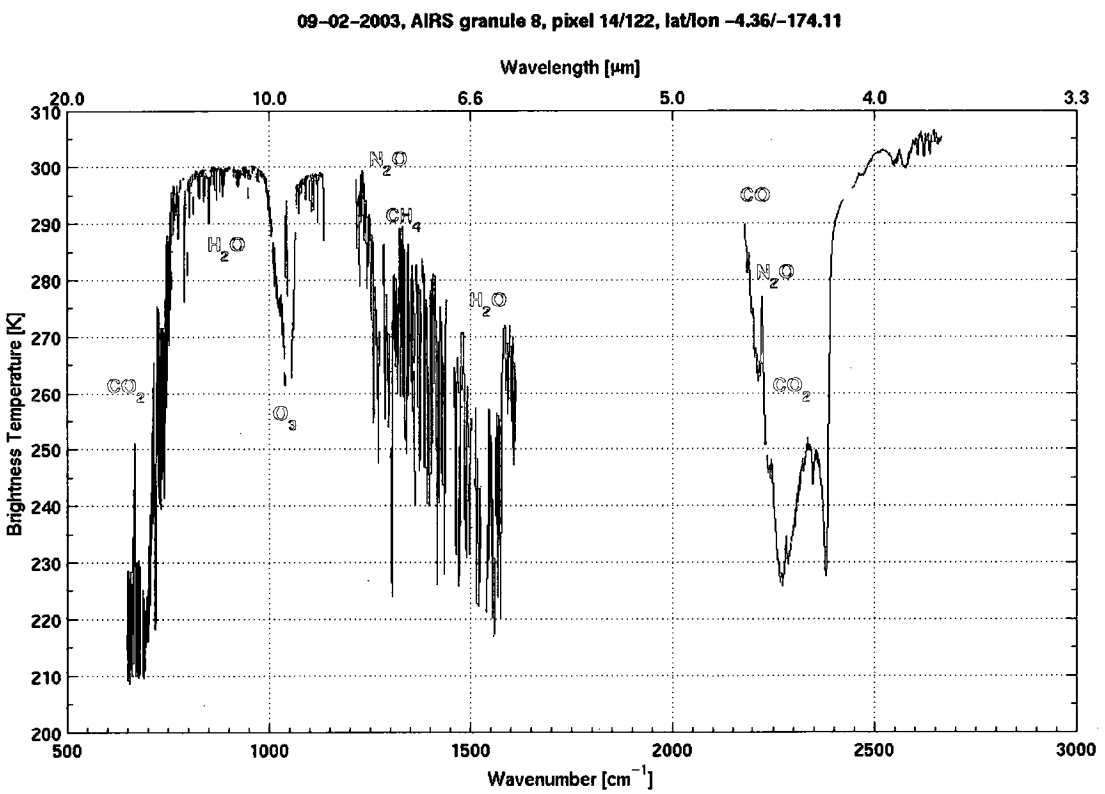

Figure 3.1 Daytime AIRS brightness temperature spectrum as a function of wavenumber (granule 8, 02 September 2003, footprint 14, scan-line 122).

near polar orbit at an altitude of 705 km resulting in a period of 99 minutes. The AIRS instrument specifications are given in Table 3.1. A set of 6 minutes of AIRS data is called a

granule which comprises 135 scan-lines with 90 footprints per scan-line. There are 240 granules per day available with a global coverage obtained twice (day and night).

Table 3.1 AIRS instrument specifications

Specification	**Value**
Spectral Range	3.74 μm – 15.4 μm
Spectral Resolution	$\nu/\Delta\nu = 1200$
Field-of-View	1.1° (13 km at nadir)
Swath Width	99°
Calibration	0.2 K at 250 K
Orbital Period	99 minutes

AIRS uses an array of 17 cooled HgCdTe detectors. Each detector has between 94 – 192 elements. Energy dispersed from the diffraction grading is imaged onto the arrays. There are two pixels sensed separately per spectra channel (for redundancy purposes), and each spectral channel has a weighting function that peaks of a region in altitude and is sensitive to a certain height in the atmosphere. The large number of channels and relatively high spectral resolution provide coverage of the whole atmosphere and enable the retrieval of vertical temperature and humidity profiles with high vertical resolution as well as cloud-top properties and amounts of greenhouse gases. AIRS radiometric calibration is well characterized with a relative radiometric accuracy of 0.2 K at 205 K [*Fetzer et al.*, 2003]. The absolute calibration is 3% for brightness temperatures between 190 K and 330 K [*Fetzer et al.*, 2003]. Global temperature and humidity

soundings with high accuracy (~1 K/1 km layer for temperature and ~15%/2 km layer for moisture in the troposphere) as well as surface parameters (surface skin temperature and surface IR emissivities) have been used for applications in various research activities, climate modeling, monitoring and numerical weather (NWP) prediction. This study uses the atmospheric profile retrievals and spectral signatures from AIRS to investigate UT structures, and utilizes the advantage of high spectral resolution observations to distinguish the convection penetrating the tropopause as well as the estimated precipitation intensity.

3.2 The High Spatial Resolution Imager – MODIS

MODIS is a key instrument of the EOS Terra and Aqua satellites for conducting global environmental change research. It is a scanning radiometer and provides global observations of earth's land, oceans, and atmosphere in 36 visible, near infrared, and infrared regions of the spectrum from 0.415 μm – 14.235 μm [*King et al.*, 2003; *Platnick et al.*, 2003]. The nadir spatial resolution is dependent on the spectral channel and ranges between 250 – 1000 meters. An overview of the MODIS instrument characteristics is given in Table 3.2. Only EOS Aqua polar orbiting MODIS allows for continuous coincident measurement with AIRS. In this dissertation, operational MODIS level-1B infrared radiances and Level 2 cloud mask product are utilized for the enhancement of AIRS retrieval algorithm.

MODIS cloud products include, but are not limited to, the cloud mask, which provides each MODIS 1 km pixel with cloud indices; cloud phase indices; and cloud top pressure (CTP) and effective cloud amount (ECA) from MODIS CO_2 band measurements with a 5 km spatial

resolution [*King et al.*, 2003; *Platnick et al.*, 2003]. The MODIS cloud mask uses a variety of spectral tests, using as many as 20 channels, and is discussed in more detail in *Ackerman et al.*,

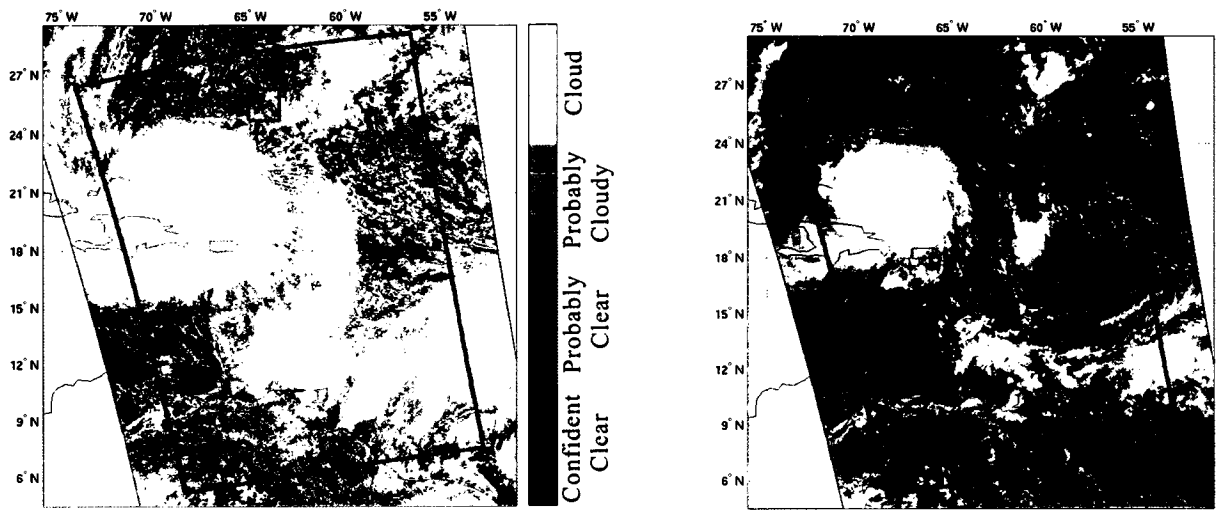

Figure 3.2 (Left panel) The MODIS cloud mask with 1-km spatial resolution of Hurricane Ike from 1730 – 1745 UTC on 06 September 2008. (Right panel) The corresponding composited true color image using *Aqua* MODIS reflectance bands 1, 4, 3 as red, green, and blue, respectively. The collocated spatial coverage of AIRS Granule 176 is overlaid using thick blue lines.

Table 3.2 MODIS instrument specifications

Specification	**Value**
Spectral Range	0.47 μm – 14.24 μm
Number of Channels	36
Spatial Resolution (nadir)	250 m (0.65 μm and 0.86 μm) 500 m (0.47, 0.56, 1.24, 1.63, and 2.13 μm) 1000 m for the other 29 channels
Swath Width	2330 km
Scan Rate	20.3 rpm
Orbital Period	99 minutes

[1998], *Frey et al.*, [2008], *Ackerman et al.*, [2008]. Further nighttime polar cloud detection has been improved by *Liu et al.*, [2004]. The MODIS cloud mask has four classifications confident clear, probably clear, uncertain/probably cloudy, or cloud. For example, Hurricane Ike (2008) MODIS cloud mask with 1-km spatial resolution from 1730 – 1745 UTC on 06 September 2008 is shown in the Figure 3.2. This product is designed to be clear sky conservative [*Platnick et al.*, 2003], meaning that it will determine a pixel clear only if the spectral test indicates a high probability that clouds are not present.

3.3 Radiative Transfer Models

The radiative transfer model (RTM) is used to simulate the observed radiances on the top-of-atmosphere (TOA) by an instrument. The current weather conditions are the starting point for all computer weather prediction models, and satellite observations provide most of the needed input data. But satellites do not measure weather variables directly. They measure reflected sunlight and emitted radiation from the earth at different spectral wavelengths. The intensity and spectral distribution of this radiation depends on important weather variables, for example, atmospheric temperature, humidity, cloudiness, precipitation, and surface properties. A radiative transfer model is the glue that connects the remote satellite observations to the weather conditions. It is a complex numerical model that, given surface and atmospheric conditions, permits calculation of the radiation, and, given measurements of the radiation, enables extraction of information on the surface and atmosphere. The radiative transfer model must not only be accurate but must be computational efficient to enable assimilation of millions of satellite observations in a matter of minutes. Since the AIRS is a high spectral resolution instrument

with more than 2300 spectral channels, the RTM costs the most CPU-intensive part of the operational processing. Therefore, the requirements for the AIRS RTM must be fast, and the RTM forward calculation accuracy approaches the nominal noise level of the instrument.

Table 3.3 SARTA/PFAAST Pressure Levels

Level Number	Pressure [hPa]	Level Number	Pressure [hPa]	Level Number	Pressure [hPa]
1	0.0050	35	47.1882	69	374.7241
2	0.0161	36	51.5278	70	390.8926
3	0.0384	37	56.1260	71	407.4738
4	0.0769	38	60.9895	72	424.4698
5	0.1370	39	66.1253	73	441.8819
6	0.2244	40	71.5398	74	459.7118
7	0.3454	41	77.2396	75	477.9607
8	0.5064	42	83.2310	76	496.6298
9	0.7140	43	89.5204	77	515.7200
10	0.9753	44	96.1138	78	535.2322
11	1.2972	45	103.0172	79	555.1669
12	1.6872	46	110.2366	80	575.5248
13	2.1526	47	117.7775	81	596.3062
14	2.7009	48	125.6456	82	617.5112
15	3.3398	49	133.8462	83	639.1398
16	4.0770	50	142.3848	84	661.1920
17	4.9204	51	151.2664	85	683.6673
18	5.8776	52	160.4959	86	706.5654
19	6.9567	53	170.0784	87	729.8857
20	8.1655	54	180.0183	88	753.6275
21	9.5119	55	190.3203	89	777.7897
22	11.0038	56	200.9887	90	802.3714
23	12.6492	57	212.0277	91	827.3713
24	14.4559	58	223.4415	92	852.7880
25	16.4318	59	235.2338	93	878.6201
26	18.5847	60	247.4085	94	904.8659
27	20.9224	61	259.9691	95	931.5236
28	23.4526	62	272.9191	96	958.5911
29	26.1829	63	286.2617	97	986.0666
30	29.1210	64	300.0000	98	1013.9476
31	32.2744	65	314.1369	99	1042.2319
32	35.6505	66	328.6753	100	1070.9170
33	39.2566	67	343.6176	101	1100.0000
34	43.1001	68	358.9665		

The Stand-alone Radiative Transfer Algorithm (SARTA v1.07) [*Strow et al.*, 2003] is used to simulate the AIRS clear sky radiances. The SARTA RTM is widely used in the community because of its better consideration of the spectroscopy for atmospheric transmittances computation, and the quality of the fast RTM transmittance parameterization. It has 100 pressure-layer (101 pressure levels) vertical coordinates from 0.005 to 1100 hPa (Table 3.3). The calculations take into account the satellite zenith angle, absorption by well-mixed gases (including nitrogen, oxygen, etc.), water vapor (including the water vapor continuum), ozone, and carbon dioxide.

Through the joint efforts of the University of Wisconsin-Madison and Texas A&M University, a fast radiative transfer cloud model for hyperspectral infrared sounder measurements has been developed [*Wei et al.*, 2004]. The cloudy RTM calculation is simplified with two cloud phases: ice and liquid water. For ice clouds, the bulk single-scattering properties of ice crystals are derived by assuming droxtals for small particles (0 – 50 μm), hexagonal geometries for moderate particles (50 – 300 μm), and aggregates for large particles (> 300 μm) [*Yang et al.*, 2000, 2003]. For liquid water clouds, spherical water droplets are assumed, and their single scattering properties are computed through the classical Lorenz–Mie theory. In the model input, the cloud optical thickness is specified in terms of its visible optical thickness at 0.55 μm. The infrared cloud optical thickness for each AIRS channel i can be derived through the following relationship:

$$\tau_i = \frac{\langle Q_e \rangle}{2} \tau_{vis} \quad , \tag{3.1}$$

where τ is the cloud optical thickness and $\langle Q_e \rangle$ is the bulk mean extinction efficiency. Given the visible cloud optical thickness (τ_{vis}) and cloud particle size, the infrared cloud optical thickness, the single-scattering albedo, and the asymmetry factor can be obtained from a pre-described parameterization of the bulk radiative properties of ice clouds and water clouds. The detailed parameterization scheme has been reported in previous work [*Wei et al.*, 2004]. The cloudy radiance for a given AIRS channel i can be computed by coupling the clear sky optical thickness and the cloud optical effects. The cloud optical effects are accounted for by using a pre-computed lookup table of cloud reflectance and transmittance on the basis of fundamental radiative transfer principles.

The clear radiative transfer calculation of the MODIS spectra band radiances is performed by using a transmittance model called Pressure-Layer Fast Algorithm for Atmospheric Transmittance (PFAAST) [*Hannon et al.*, 1996]. PFAAST is based on the line by line radiative transfer model (LBLRTM) version 8.4 [*Clough and Iacono*, 1995] and the high-resolution transmission molecular absorption database-2000 (HITRAN-2000) [*Rothman et al.*, 1992] with updates (aer_hitran_2000_updat_01.1). This model has 100 pressure-layers (101 pressure levels), identical to the pressure levels as used in SARTA, vertical coordinates from 0.05 to 1100 hPa. The new 101-level PFAAST calculates the radiances with better accuracy and less model bias then the old 42-level one. The calculations of this model also accounts for the satellite zenith angle, absorption by well-mixed gases (including nitrogen, oxygen, and carbon dioxide), water vapor (including the water vapor continuum) and ozone.

Chapter 4 The Handling of High Spectral Resolution Radiance

Obtaining the correct atmospheric profiles is the foundation for conducting the analyses of the atmospheric state from satellite measurements. Due to the relatively large spatial resolution of the sounder, it is very often that a given sounder footprint often includes clouds. This chapter will address the handling of high spectral resolution spectra, in particular the cloudy scene, which includes the optimal use of imager data to derive clear-equivalence radiance.

4.1 Traditional Cloud-clearing of the Cloud Contaminated Infrared Radiances

The chance of an AIRS footprint being completely clean is less than 10% statistically due to the relative poor spatial resolution of 13.5 km at nadir [*Huang and Smith*, 2004]. Therefore, getting atmospheric temperature and moisture vertical profiles under cloudy skies becomes very important. *Smith et al.* [2004] suggested that there are essentially three ways to deal with cloudy radiances in the sounding process:

(1) Assume opaque cloud conditions and retrieve the profile above the cloud;

(2) Cloud-clear the radiance to obtain the clear-equivalent radiances, and retrieve the profile following the clear sky procedure using the cloud-cleared radiances; and

(3) Make use of a physically based radiative transfer model in the retrieval.

To perform cloud-removal or clearing on the AIRS cloudy radiance spectrum is the most effective among these three approaches, because this procedure does not require modeling the radiative transfer in cloudy conditions and is, therefore, a computationally cost-effective method of handling infrared cloudy scenes.

For example, using microwave data for AIRS cloud-clearing is considered very robust due to the loss of spatial gradient for certain meteorological applications. The cloud-clearing on an AIRS cloudy footprint is superior for resolving the mesoscale weather phenomena than at the microwave spatial resolution, and will benefit for numerical weather predication. *Smith et al.* [2004] combined MODIS infrared clear radiances and AIRS cloudy radiances for cloud-clearing using the traditional single-band N^* approach, where N^* is determined from MODIS infrared clear radiance at a single infrared window (11 μm) band. Once N^* is determined, the AIRS cloud-cleared radiances can be obtained by simply applying N^* to the cloudy radiances from two adjacent AIRS footprints.

Traditional single-band cloud-clearing is based on the linear relationship in radiances between clear and overcast scenes. Given that R_ν^1 (the principle footprint) and R_ν^2 (the supplementary footprint) are the AIRS cloudy radiance spectra as a function of wavenumber ν from two adjacent footprints, we assume that these two footprints have:

(1) The same atmospheric temperature and moisture profiles;

(2) The same surface skin temperatures and surface infrared emissivity spectrum; and

(3) The same cloud properties (e.g., cloud top height),

while the only difference is the effective cloud emissivities, in terms of $N\varepsilon_c$ - the product of the cloud emissivity (ε_c) and the cloud fraction (N). The cloudy radiance spectra of the primary and supplementary footprints can be expressed as

$$R_\nu^1 = (1 - N^1\varepsilon_{\nu c}^1)R_\nu^{clr} + N^1\varepsilon_{\nu c}^1 R_\nu^{ovc} \tag{4.1}$$

$$R_\nu^2 = (1 - N^2\varepsilon_{\nu c}^2)R_\nu^{clr} + N^2\varepsilon_{\nu c}^2 R_\nu^{ovc} \tag{4.2}$$

where subscript c denotes the cloud, and R_ν^{clr} and R_ν^{ovc} are the clear and overcast column radiance spectra, respectively. Equations (4.1) and (4.2) can be rewritten as

$$R_\nu^1 - R_\nu^{clr} = N^1\varepsilon_{\nu c}^1(R_\nu^{ovc} - R_\nu^{clr}) \tag{4.3}$$

$$R_\nu^2 - R_\nu^{clr} = N^2\varepsilon_{\nu c}^2(R_\nu^{ovc} - R_\nu^{clr}) \tag{4.4}$$

From equation (4.3) and (4.4), we have

$$\frac{R_\nu^1 - R_\nu^{clr}}{R_\nu^2 - R_\nu^{clr}} = \frac{N^1\varepsilon_{\nu c}^1}{N^2\varepsilon_{\nu c}^2} = N^*. \tag{4.5}$$

Equation (4.5) gives the definition of N^*, which is made independent of wavenumber by assuming $\varepsilon_{\nu c}^1 = \varepsilon_{\nu c}^2$. If N^* is known or estimated, then the AIRS cloud-clear radiances spectrum R_ν^{cc} can be retrieved by

$$R_\nu^{cc} = \frac{R_\nu^1 - R_\nu^2 N^*}{1 - N^*} \tag{4.6}$$

The key question is how to best determine N^*. In order to determine N^*, one needs to know the clear radiance at a certain wavenumber with good accuracy. *Smith et al.* [2004] used the MODIS IR window spectral band (11 μm; band 31) clear radiance together with convolved AIRS cloudy radiances with MODIS 11 μm spectral response function within the two adjacent footprints to determine N^*, i.e.,

$$N^* = \frac{f_{31}(R_\nu^1) - R_{M_{31}}^{clr}}{f_{31}(R_\nu^2) - R_{M_{31}}^{clr}} \tag{4.7}$$

where f_i is the SRF for MODIS infrared band i, and $R_{M_i}^{clr}$ is the averaged observed clear radiance for MODIS infrared spectral band i for the two adjacent AIRS footprints. Once N^* is determined by Equation (4.7), the AIRS clear column radiance spectrum for this footprint then can be derived by Equation (4.6).

Equation (4.7) is the traditional method to estimate N^* using a single infrared window spectral band. Although the equation provides a straight forward way to calculate N^*, and therefore cloud-cleared radiances using Equation (4.6), it poses a new question of how to determine the averaged observed clear radiance for MODIS infrared spectral band i for a given AIRS footprint ($R_{M_i}^{clr}$).

4.2 Collocation of the Sounder and Imager Observations

Table 4.1 lists the MODIS spectral band specifications, while Figure 4.1 shows the MODIS spectral response functions (SRFs) overlaid with an AIRS brightness temperature (BT)

Table 4.1 MODIS spectral band specification. The numbers in this table are cited from http://modis.gsfc.nasa.gov/about/specs.html

Primary use	Band	Bandwidth[1]	Spectral radiance[2]	Required SNR[3]
Land/Cloud/Aerosols Boundary	1	620-670	21.8	128
	2	841-876	24.7	201
Land/Cloud/Aerosols Properties	3	459-479	35.3	243
	4	545-565	29.0	228
	5	1230-1250	5.4	74
	6	1628-1652	7.3	275
	7	2105-2155	1.0	110
Ocean Color/Phytoplankton/Biogeochemistry	8	405-420	44.9	880
	9	438-448	41.9	838
	10	483-493	32.1	802
	11	526-536	27.9	754
	12	546-556	21.0	750
	13	662-672	9.5	910
	14	673-683	8.7	1087
	15	743-753	10.2	586
	16	862-877	6.2	516
Atmospheric Water Vapor	17	890-920	10.0	167
	18	931-941	3.6	57
	19	915-965	15.0	250
Primary use	**Band**	**Bandwidth[1]**	**Spectral radiance[2]**	**Required NEΔT[4](K)**
Surface Temperature	20	3.660-3.840	0.45 (300 K)	0.05
	21	3.929-3.989	2.38 (335 K)	2.00
	22	3.929-3.989	0.67 (300 K)	0.07
	23	4.020-4.080	0.79 (300 K)	0.07
Temperature profile	24	4.433-4.498	0.17 (250 K)	0.25
	25	4.482-4.549	0.79 (300 K)	0.25
Cirrus Clouds/water vapor	26	1.360-1.390	6.00	150 (SNR)
	27	6.535-6.895	1.16 (240 K)	0.25
Primary use	**Band**	**Bandwidth[1]**	**Spectral radiance[2]**	**Required SNR[3]**
	28	7.175-7.475	2.18 (250 K)	0.25
	29	8.400-8.700	9.58 (300 K)	0.05
Ozone	30	9.580-9.880	3.69 (250 K)	0.25
Surface Temperature	31	10.780-11.280	9.55 (300 K)	0.05
	32	11.770-12.270	8.94 (300 K)	0.05
Temperature profile	33	13.185-13.485	4.52 (260 K)	0.25
	34	13.485-13.785	3.76 (250 K)	0.25
	35	13.785-14.085	3.11 (240 K)	0.25
	36	14.085-14.385	2.08 (220 K)	0.35

[1]Bands 1 to 19 are in nm, and bands 20 to 36 are in μm; [2]Spectral radiance values are (W $m^{-2}sr^{-1}\mu m^{-1}$); [3]SNR = Signal-to-noise ratio; [4]NEΔT = Noise-equivalent temperature difference

spectrum. It shows there is a direct relationship between AIRS and MODIS spectral observations. From this, we assume that both instruments observe an identical atmospheric column for a given AIRS footprint collocated with MODIS pixels.

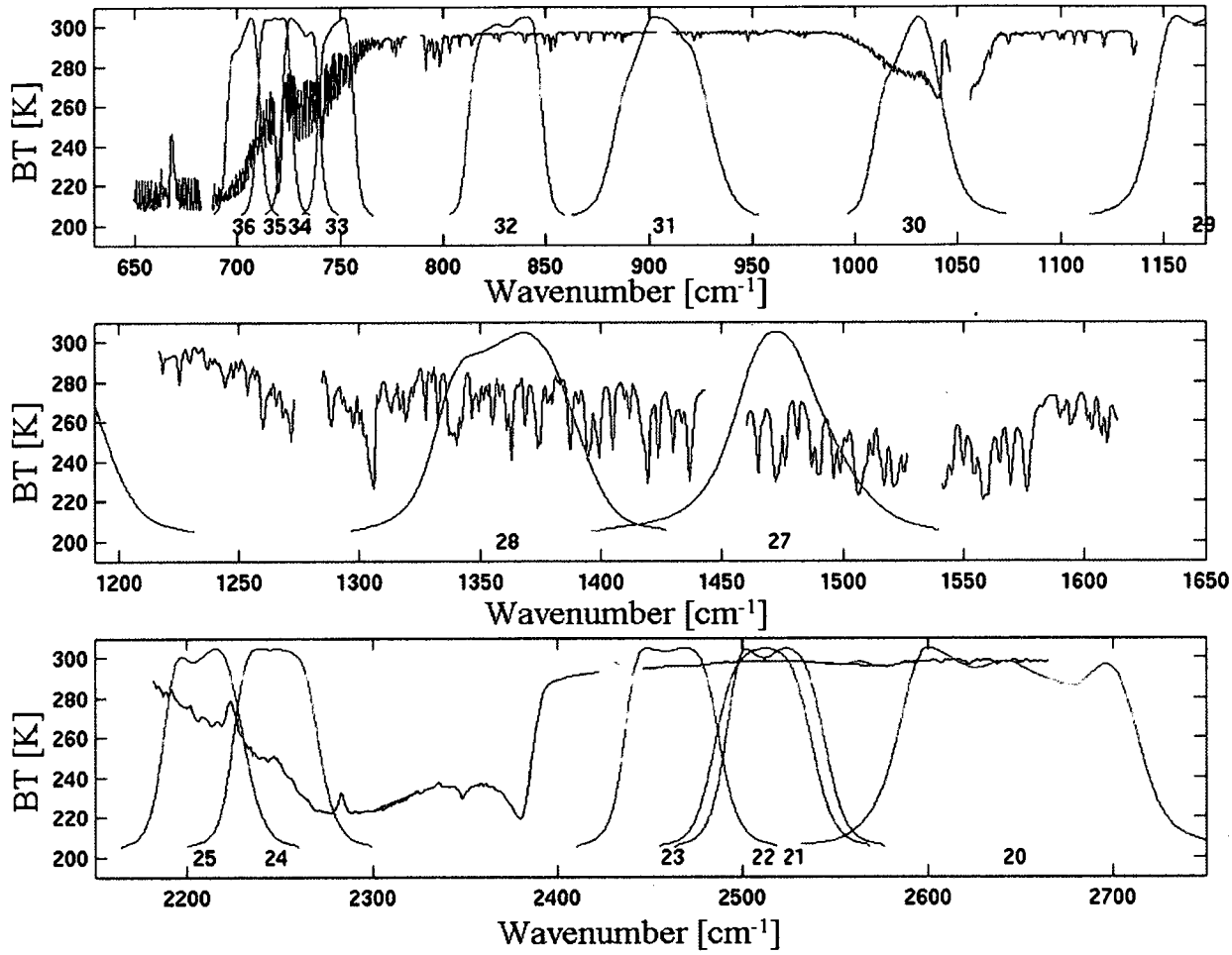

Figure 4.1 MODIS spectral response functions (red curves) overlaid with an AIRS brightness temperature spectrum (black curves). The units of the abscissa and ordinate are wavenumber (cm^{-1}) and brightness temperature (K), respectively.

The AIRS spatial distribution is used in the geolocation collocation between the MODIS and AIRS measurements, which is the first step for the combined use of both instruments. Several collocation algorithms have been developed that are based on the scanning geometry of two instruments flown on the same satellite [*Aoki*, 1985; *Nagle*, 1998]. The collocation designates the instrument with the larger field-of-view (FOV) as the principle instrument, in this

case the AIRS, and the collocation method then locates all of the secondary instrument's FOVs that fall within each principle FOV. For this application, the instruments are located on the same platform (NASA's EOS *Aqua* satellite), simplifying the inverse navigation needed for the collocation. Meanwhile, for a set of AIRS earth-located observations, the footprint of each AIRS observation describes a shape that is circular at nadir, quasi-ellipsoidal at intermediate scan angles, and ovular at extreme scan angles.

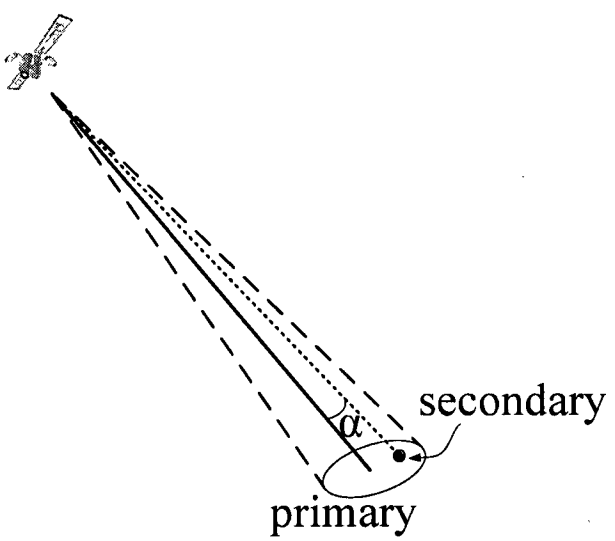

Figure 4.2 The primary (AIRS) and the secondary (MODIS) instruments collocation procedure is illustrated. The primary field of view is defined as the half angular field of view of the AIRS. The angle between the secondary instrument (MODIS) geolocation and the center axis of the AIRS footprint is designated α in this figure. If α is less than the half angular field of view of the primary footprint, the secondary pixel is considered to be within the field of view of the AIRS.

The AIRS and MODIS collocation procedure uses a simplification described in Figure 4.2. The procedure finds all secondary (MODIS) pixels with angle α, measured between the

secondary pixel geolocation and the center of the principle (AIRS) footprint, are less than half the angular width of the principle instrument. The instrument time is used to narrow the search region for finding collocated secondary pixels, but is not used in the actual collocation. The diameter of the AIRS footprint at nadir is approximately 13.5 km. Depending on the angular difference between the AIRS and MODIS slant range vectors, a weight (w) is assigned to each MODIS pixel collocated to AIRS, which is proportional to the inverse of the distance to the center of principle foorptint: 1 if the MODIS pixel lies at the center of the AIRS oval, and 0 if at the outer edge. The collocation is modeled correctly if the algorithm provides an accuracy better than 1 km, provided that the geometry information from both instruments is accurate.

Once the MODIS pixels are collocated with the AIRS footprints, the cloud properties within the AIRS FOV can be characterized using the result from the MODIS cloud mask and cloud phase mask products [*King et al.*, 2003; *Platnick et al.*, 2003]. The AIRS cloud mask, and cloud phase mask, as well as the cloud-layer information mask, can be generated from MODIS products with a 1-km spatial resolution [*Li et al.*, 2004]. For each AIRS footprint, a cloud fraction mask (0 – 1) is created by accounting for the percentage of MODIS pixels without the confident clear and probably clear indices within the footprints as

$$CldFrac = 1 - \left(\frac{n^{clr}_{confident} + n^{clr}_{probably}}{n^{all}} \right) \tag{4.8}$$

where n^{all}, $n^{clr}_{confident}$, and $n^{clr}_{probably}$ stand for the total number of MODIS 1-km pixels, confident clear pixels, and probably clear pixels, respectively, within the AIRS footprint. Figure 4.3 is an

example of AIRS cloud fractions derived from MODIS cloud mask with a 1-km spatial resolution.

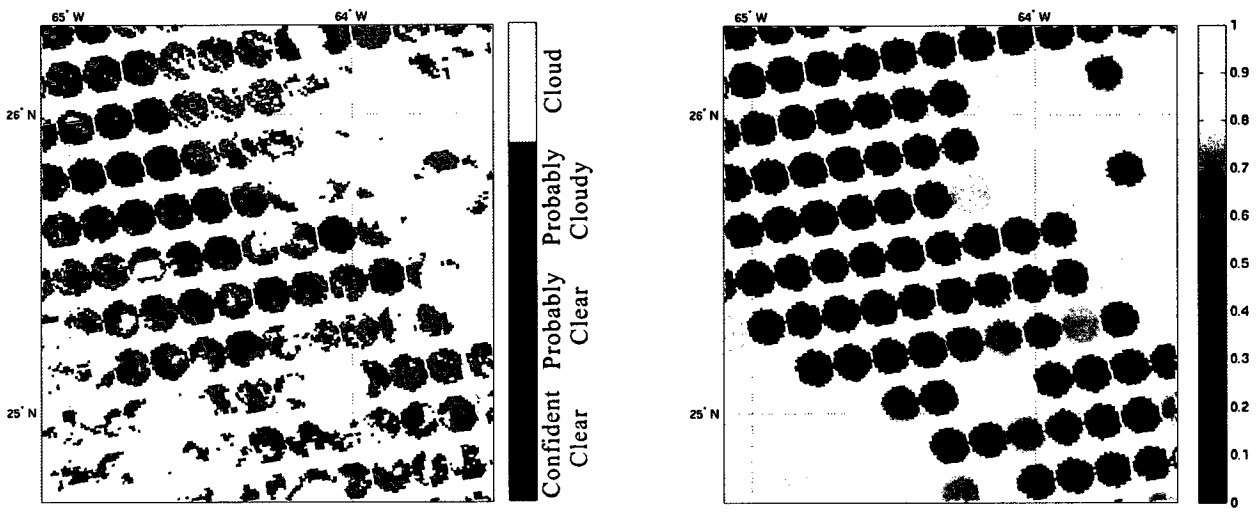

Figure 4.3 (Left panel) MODIS cloud mask with 1-km spatial resolution superimposed to the AIRS footprints from a small area approximately 7° north of Puerto Rico (see the 1.5° by 1.5° red box on the left panel of Figure 3.2). (Right panel) The corresponding AIRS cloud fraction (see color bar) derived from MODIS 1-km cloud mask product on the left panel.

Only confident clear MODIS pixels within the AIRS footprint are averaged as observed clear radiance for a MODIS infrared spectral band i for a given AIRS footprint ($R_{M_i}^{clr}$) as

$$R_{M_i}^{clr} = \frac{\sum_{l=1}^{np} w_l R_{M_i}^{clr,l}}{\sum_{l=1}^{np} w_l} \tag{4.9}$$

where $R_{M_i}^{clr,l}$ is the MODIS spectral band i radiance of confident clear pixel l, np is the number of confident clear pixels within the AIRS footprint, and w_l is the weight of pixel l within the AIRS footprints as described in Chapter 4.1.

4.3 Optimal Cloud-clearing of the Cloud Contaminated Radiances

The cloud-clearing algorithm described in Chapter 4.1 determines N^* from a single MODIS spectral band. Using different MODIS infrared window spectral bands, the result may yield different cloud-cleared spectra. The results are highly dependent on the quality control for the single-band N^* cloud-clearing.

To obtain an optimal N^* value and make the cloud-clearing result dependent on an objective quality control based on all MODIS spectral bands, *Li, Liu and co-authors*, [2005a] developed an optimal cloud-clearing methodology. In the optimal AIRS/MODIS cloud-clearing, Equation (4.5) is adopted for the definition of N^*; however, the N^* value is determined by simultaneously minimizing the differences between the MODIS infrared observations and the convolved AIRS cloud-cleared radiances with SRFs for all nine MODIS infrared spectral band within primary AIRS footprint.

The cost function for the optimal cloud-clearing is defined as

$$J(N^*) = \sum_i \frac{1}{\sigma_i^2}\left[\left(R_{M_i}^{clr} - f_i(R_v^{cc})\right)\right]^2. \qquad (4.10)$$

Since the cloud-cleared radiances spectrum, R_v^{cc}, is a function of N^* [see Equation (4.6)], Equation (4.10) becomes

$$J(N^*) = \sum_i \frac{1}{\sigma_i^2} \left[\left(R_{M_i}^{clr} - f_i\left(\frac{R_v^1 - R_v^2 N^*}{1 - N^*}\right) \right) \right]^2 \tag{4.11}$$

where σ_i is the radiance detector noise (NEdR) for MODIS band i. Given that the spectral response function f_i is a linear operator for MODIS infrared spectral band, Equation (4.11) becomes

$$J(N^*) = \sum_i \frac{1}{\sigma_i^2} \left[\left(R_{M_i}^{clr} - \frac{1}{1 - N^*} f_i(R_v^1) + \frac{N^*}{1 - N^*} f_i(R_v^2) \right) \right]^2 . \tag{4.12}$$

Therefore, the first-order derivation of $J(N^*)$ with respect to N^* can be derived from Equation (4.12) as

$$\frac{\partial J(N^*)}{\partial N^*} = \frac{2}{(1 - N^*)} \sum_i \frac{1}{\sigma_i^2} \left[R_{M_i}^{clr} - \frac{1}{1 - N^*} f_i(R_v^1) + \frac{N^*}{1 - N^*} f_i(R_v^2) \right] \left[f_i(R_v^1) - f_i(R_v^2) \right]. \tag{4.13}$$

We may have the solution for Equation (4.13) by minimization of the cost function $J(N^*)$ as

$$\frac{\partial J(N^*)}{\partial N^*} = 0 . \tag{4.14}$$

N^* can be analytically solved from Equation (4.14) in the form of

$$N^* = \frac{\sum_i \frac{1}{\sigma_i^2}\left[f_i(R_v^1) - R_{M_i}^{clr}\right]\left[f_i(R_v^1) - f_i(R_v^2)\right]}{\sum_i \frac{1}{\sigma_i^2}\left[f_i(R_v^2) - R_{M_i}^{clr}\right]\left[f_i(R_v^1) - f_i(R_v^2)\right]}. \quad (4.15)$$

Once N^* is determined by Equation (4.15), the cloud-cleared AIRS radiance spectrum, arbitrarily located at the location of the principal footprint, can be retrieved by applying N^* to Equation (4.6).

In this dissertation, nine MODIS infrared spectral bands (bands 22, 24, 25, 28, 30, 31, 32, 33, and 34) are used. MODIS spectral bands 20, 23, 27, and 29 are not used because the convolution error introduced by the spectral gaps in the AIRS measurements (Figure 4.1), while band 21 is not used because the larger detector noise (Table 4.1). There is spectral response function calibration error in MODIS infrared spectral bands 35 and 36 [*Tobin et al.*, 2006a], both bands are not applied in this dissertation, either.

The advantage of Equation (4.15) is that the multiple MODIS spectral bands are weighted in the N^* calculation. There are two weighting factors, the detector noise accounts for the observation error in the N^* calculation, while the radiance contract between the two adjacent footprints accounts for the cloud height effect in the N^* calculation. For example, if the pair contains low clouds, the MODIS middle and upper level bands 33 and 34 will have less weight due to small value of $f_i(R_v^1) - f_i(R_v^2)$. However, when the pair contains middle or upper clouds, bands 33 and 34 will influence the N^* calculation. Beside the cloud height effect, cloud fraction is another factor contributing the spectral weighting that maximizes the information content of the optimal cloud-clearing approach.

4.4 Application of Optimal Cloud-clearing

AIRS and MODIS Level-1B data and Level-2 products from Hurricane Ike (2008) are used to demonstrate the optimal cloud-clearing study. The AIRS cloud fraction mask is derived from the MODIS cloud mask product with 1-km spatial resolution. A fractional coverage (0 – 1) is derived to represent clear ($CldFrac = 0$) to cloudy ($CldFrac = 1$) for a given AIRS footprint. The AIRS footprints or fields-of-view can then be classified as fully cloudy (overcast), partly cloudy, and clear (Figure 4.4). Only AIRS footprints classified as partly cloudy are used in

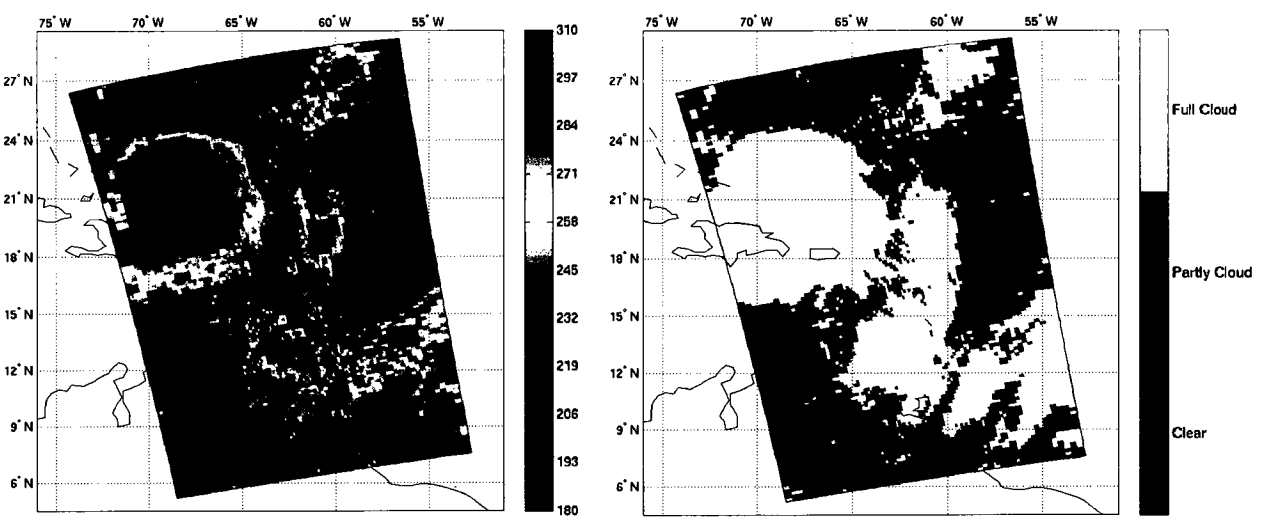

Figure 4.4 (Left panel) AIR brightness temperature image of channel 770 (911.235 cm^{-1}, approximately 11 μm on September 06, 2008). (Right panel) The AIRS coverage of clear, partly cloudy, and overcast footprints according to the collocated MODIS pixels.

cloud-clearing. The left of Figure 4.4 shows the AIRS brightness temperature image of channel 770 (911.235 cm^{-1}) on September 06, 2008 (AIRS granule 176); the presence of clouds is indicated by the blue (cold) colors. The right panel of Figure 4.4 shows the coverage of clear, partly cloudy and overcast cloudy footprints derived from the MODIS cloud mask with 1-km spatial resolution (see left panel of Figure 3.2). Note that the color bars have different definitions in the two panels.

Figure 4.5 shows the diagram of the principle (center) footprint and its eight surrounding supplementary footprints. The steps of optimal cloud-clearing are as follows.

(1) For each partly cloudy AIRS footprint (principle footprint l), find its eight nearby cloudy footprint in any direction (maximum eight nearby cloudy footprints) k ($k = 1,2,3,...,8$).

(2) For each pair (l, k), calculate $N^*(k)$, ($k = 1,2,3,...,8$) using Equation (4.15).

(3) Calculate $R_v^{cc}(k)$ ($k = 1,2,3,...,8$) from Equation (4.6).

(4) Calculate $RES(k) = \sum_i \left(\frac{1}{\sigma_i}\right)\left[R_{M_i}^{clr} - f_i\left(R_v^{cc}(k)\right)\right]^2$.

(5) Find k_m, which makes $RES(k_m) = \min RES(k)$.

(6) Apply quality control to the selected $R_v^{cc}(k_m)$ and calculate

$$TB_{RMS} = \sqrt{\frac{1}{I}\sum_i \left[T_b\left(R_{M_i}^{clr}\right) - T_{bi}\left(f_i\left(R_v^{cc}\left(k_m\right)\right)\right)\right]^2} \qquad (4.16)$$

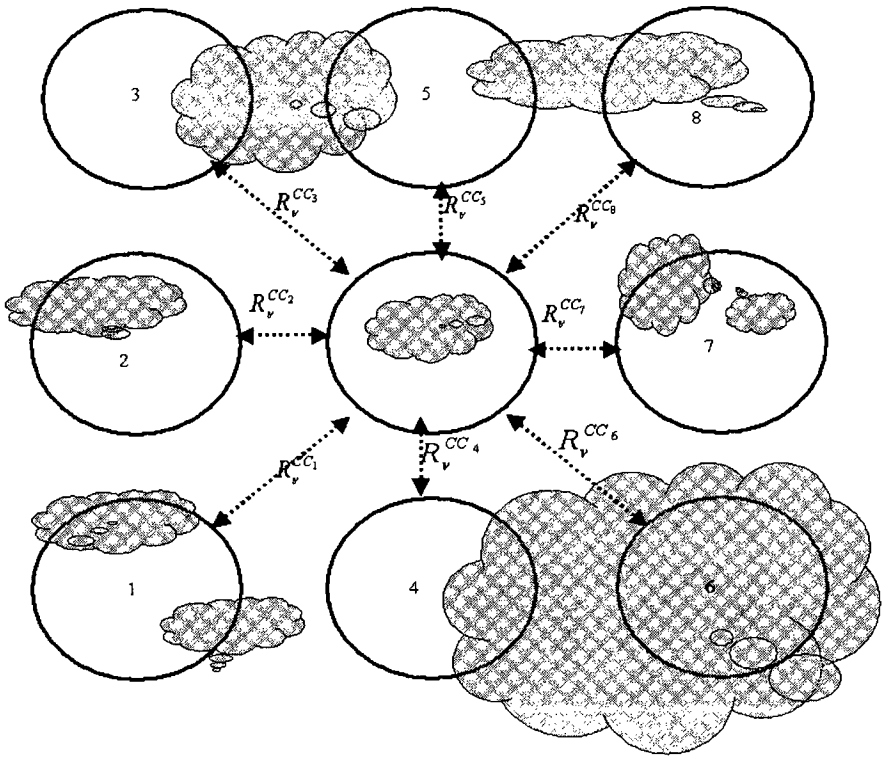

Figure 4.5 Diagram of the principle footprint and its eight surrounding supplementary footprints in the optimal cloud-clearing procedure.

where I is the total number if MODIS spectral bands used for quality control, T_{bi} is the function that converts the radiances to brightness temperature for MODIS spectral band i. The optimal cloud-clearing is successful only when $TB_{RMS} < 0.5$ K; otherwise, the cloud-clearing for this principle footprint is rejected. The same nine MODIS infrared bands used for N^* determination [see Equation (4.15)] are also used for the quality control.

The cloud-cleared radiance spectrum $R_v^{cc}(k_m)$ is the final clear column radiance spectrum for the cloudy footprint l (the principle footprint). The footprint index l starts from the first footprint to the last footprint of the AIRS granule. In order to make accurate cloud-

cleared radiances, quality control must be applied to $R_\nu^{cc}(k_m)$. If the root mean square difference between the MODIS infrared clear brightness temperature observations and convolved AIRS cloud-cleared brightness temperatures (from $R_\nu^{cc}(k_m)$) with MODIS spectral response functions within the principle footprints is greater than 0.5 K [as defined in Equation (4.16)], the cloud-cleared radiance spectrum is rejected.

The optimal cloud-clearing method is applied to all AIRS footprints that are partly cloudy. The optimal cloud-clearing is not performed if the number of the MODIS clear pixels is less than 10% of the total number of MODIS pixels within this partly cloudy AIRS footprint. Figure 4.6 shows BT images of MODIS band 28 (7.3 μm) convolved from the AIRS clear footprints (the most left panel); the MODIS clear BT observations with 1-km spatial resolution (the second panel from the left); the averaged MODIS clear BT observations at collocated AIRS footprints (the third panel from the left); and the one convolved from AIRS clear plus successful cloud-cleared footprints (the most right panel). The cloud-cleared footprints fill many areas where clear AIRS FOVs are not available, especially over northeast and southwest quadrants of the hurricane, which illustrates that clear and clear-equivalent soundings, or data assimilation are achieved over certain regions and their nearby oceanic areas from AIRS cloudy radiance measurements with help from high spatial resolution of MODIS. In addition, the cloud-cleared radiances are also available over land areas within Venezuela and Guyana. Figure 4.7 shows the percentage of clear AIRS footprints, AIRS footprints with successful optimal cloud-clearing that also pass the quality control (CC-Successful), AIRS footprints with optimal cloud-clearing fail (CC-Fail), and overcast AIRS (cloud-clearing not performed). It can be seen that 4.6% of AIRS

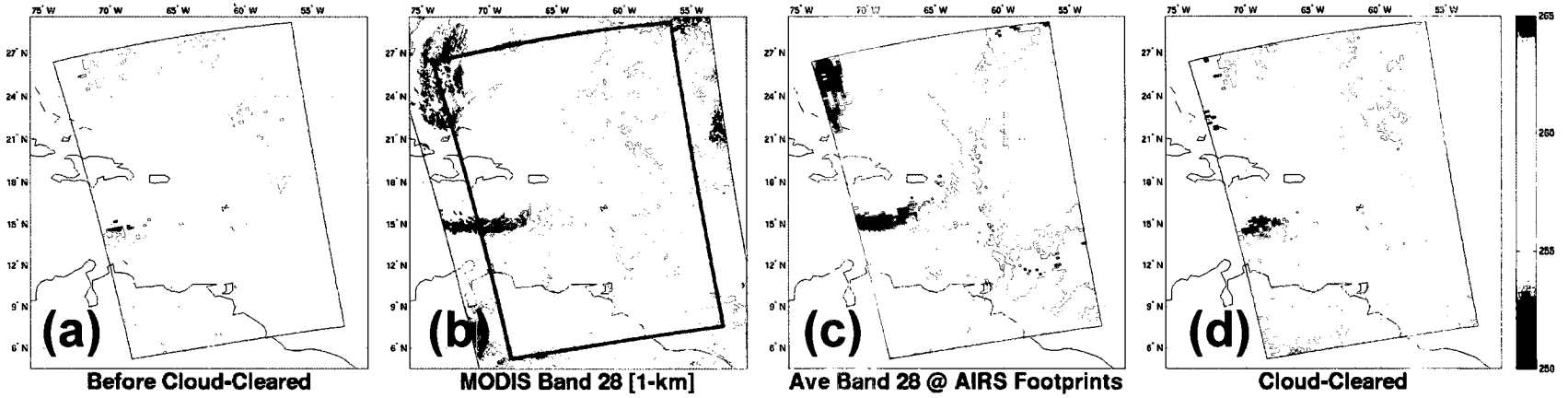

Figure 4.6 (a) Brightness temperature image of MODIS band 28 (7.3 μm) convolved from the AIRS clear footprints. (b) The MODIS band 28 clear brightness temperature observations at 1-km spatial resolution. (c) The averaged MODIS clear band 28 brightness temperature collocated at AIRS footprints. (d) Brightness temperature image of the convolved AIRS clear plus successful cloud-cleared footprints

footprints (each AIRS granule contains 135 scan lines, each scan lines has 90 footprints) are successfully clear, while 20.4% of AIRS cloudy footprints are successfully cloud-cleared. Since only partly cloudy footprints are used for cloud-clearing attempts, the success rate is more than 40% in this particular case.

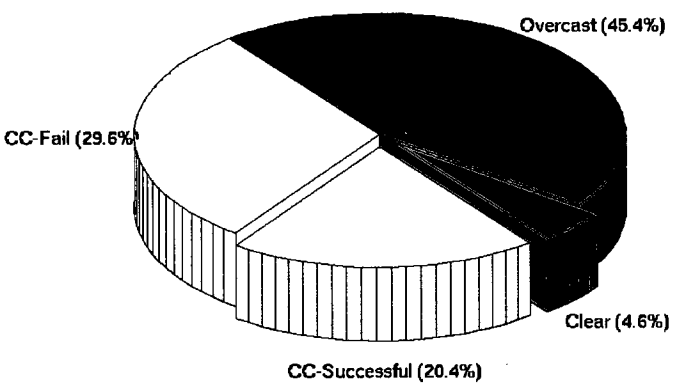

Figure 4.7 The percentage of clear AIRS footprints (Clear), AIRS footprints with optimal cloud-clearing successful (CC-Successful), AIRS footprints with optimal cloud-clearing fail (CC-Fail), and the overcast AIRS footprints (Overcast).

The traditional single-band N^* cloud-clearing method is also applied to this example; MODIS spectral 31 (11 μm) is used for N^* determination while the nine MODIS infrared spectral bands 22, 24 25, 28, 30, 31, 32, 33, and 34 are used for quality control and similar successful rate of optimal cloud-clearing is achieved. Figure 4.8 shows the bias and standard deviation between the MODIS clear BT observations and convolved AIRS cloud-cleared BTs

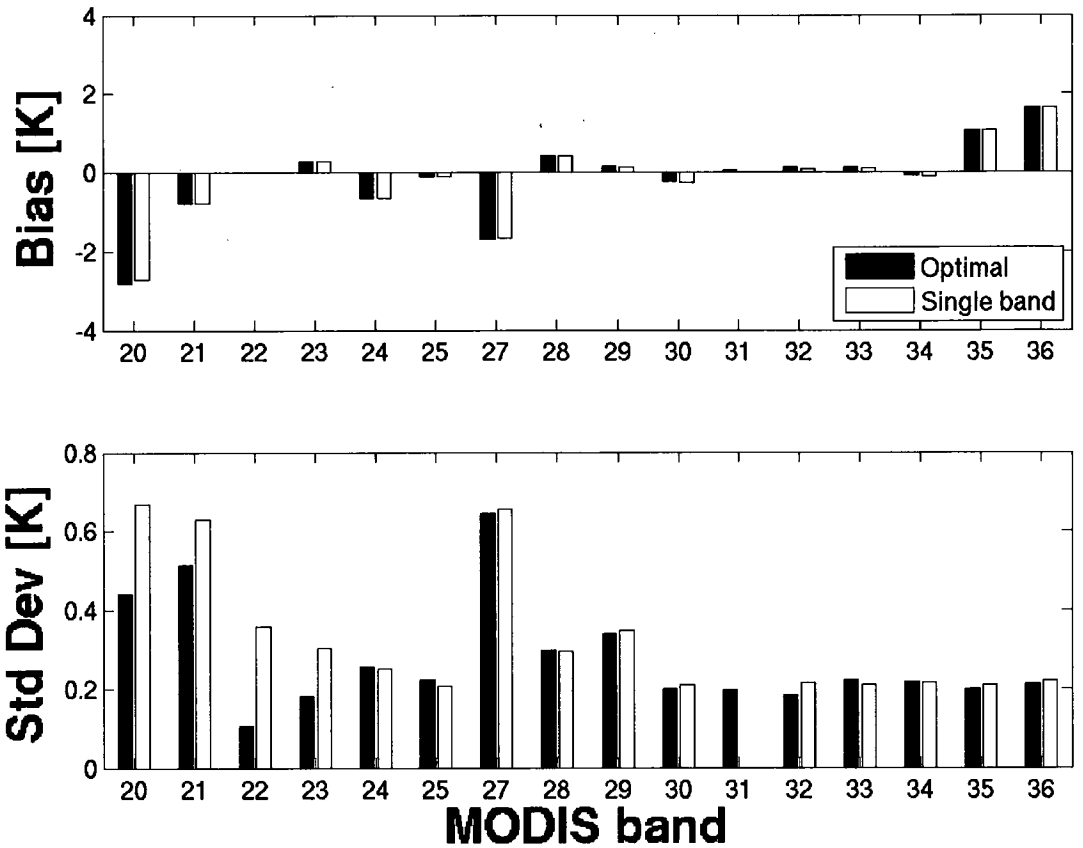

Figure 4.8 Bias and standard deviation between the MODIS clear brightness temperature observations and convolved AIRS cloud-clearing brightness temperatures from all footprints with both the optimal cloud-clearing and the single-band N^* cloud-clearing successful.

from all footprints with cloud-clearing successfully performed. Results from traditional single-band N^* cloud-clearing approach and optimal cloud-clearing method are shown in the figure. For optimal cloud-clearing method, the cloud-clearing bias for MODIS bands 22, 23, 25 and 30 through 34 are small (less than 0.25 K); the bias for bands 24 and 28 are slightly larger but still less than 0.5 K. However, bias for bands 20, 27, 35, and 36 are relative large (greater than 1.0 K) due to the convolution bias [*Tobin et al.*, 2006a]. The AIRS popping channels and/or the AIRS

channel gap in the spectral region cause the convolution bias. MODIS bands 35 and 36 might also have a spectral response function calibration bias. Those biases are removable provided that the reliable estimates are available. The standard deviation is very small (less than 0.5 K) for almost all the MODIS infrared spectral bands (only band 27 is slightly larger than 0.5 K), which indicates the good agreement between the MODIS clear BT observations and AIRS cloud-cleared BTs. For traditional single-band N^* cloud-clearing approach, the bias between the MODIS clear BT observations and AIRS cloud-cleared BTs is similar to that from the optimal cloud-cleared method; however, the standard deviations for MODIS shortwave bands 20 through 23 are worse than that of the optimal cloud-clearing method. Traditional single-band N^* approach is better in longwave infrared window region (11 μm) than the optimal cloud-clearing method because it uses MODIS 11-μm spectral band for N^* calculation. The two methods have similar performance for the other middle- and longwave spectral bands expect for bands 22 and 23 where the optimal approach performs better. Although the success rate of cloud-clearing is similar between the two methods, optimal cloud-clearing results are much closer to the MODIS clear observations for MODIS shortwave spectral bands. This is because only band 31 (11 μm) is used for N^* calculation in the traditional single-band N^* cloud-clearing method, and the infrared shortwave spectral effects might not be fully accounted for N^* estimation. With the optimal cloud-clearing method, nine MODIS infrared spectral bands are used simultaneously to balance the N^* spectrally, therefore, cloud-clearing results should be optimal when compared with the MODIS clear observations.

Figure 4.9 is a scatterplot between the MODIS infrared clear BT observations and the convolved AIRS cloud-cleared BTs with the traditional single-band N^* cloud-clearing approach

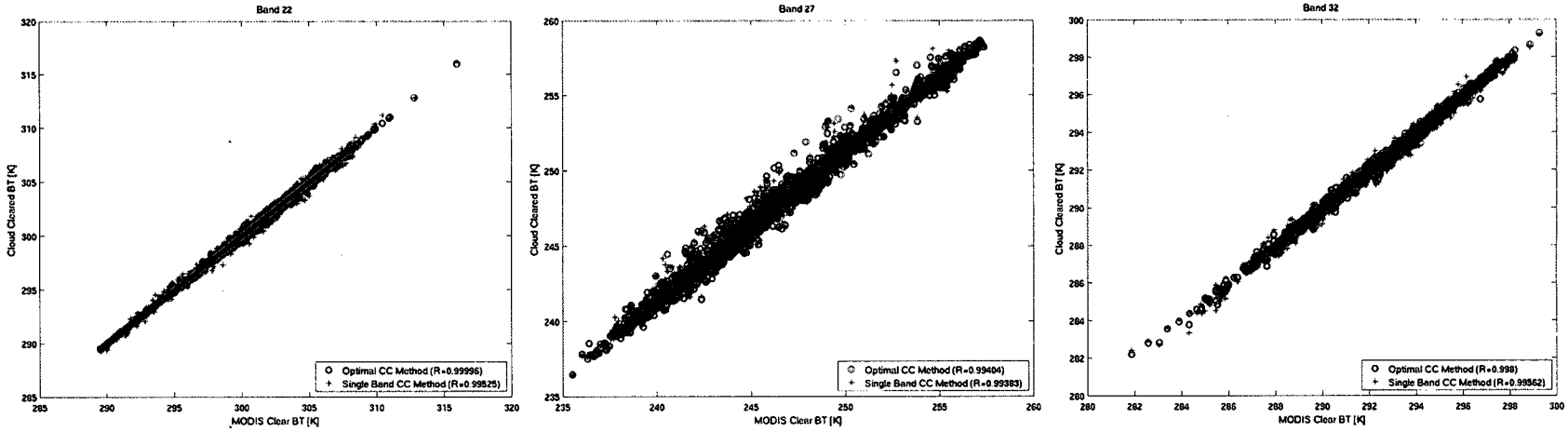

Figure 4.9 Scatterplot between the MODIS infrared clear brightness temperature observations and the convolved AIRS cloud-cleared brightness temperature with the traditional single-band N^* approach and optimal cloud-clearing method for MODIS spectral bands 22 (left panel), 27 (middle panel), and 32 (right panel).

and the optimal cloud-clearing method for MODIS spectral band 22 (left panel), 27 (middle panel), and 32 (right panel). Approximately 2400 AIRS partly cloudy footprints are included in the analysis. The optimal clear-clearing method creates less scatter and has a larger correlation with MODIS infrared clear observations for MODIS infrared spectral band 22 (3.95 μm).

Comparing the AIRS cloud-cleared BT spectrum with a nearby clear footprint BT spectrum also helps to evaluate the performance of cloud-clearing [*Huang and Smith*, 2004; *Li et al.*, 2005b]. The upper panel of Figure 4.10 shows the standard deviation between the AIRS cloud-cleared BT spectra and their nearby clear footprint BT spectra over water where the atmosphere and surface are assumed homogenous between the two clear adjacent footprints. The standard deviation of AIRS cloud-cleared BTs is less than 1 K for most spectral regions. Part of the standard deviation is due to the atmospheric non-homogeneity difference between the two adjacent footprints. The lower panel of Figure 4.10 shows the root mean square difference (RMSD) between the two-adjacent clear AIRS footprint pairs over water of the entire granule. The BT difference can be 1 K in the shortwave spectral region due to the non-uniformity of the atmospheric and surface between the two adjacent clear AIRS footprints. Therefore, the actual standard deviation of the AIRS cloud-cleared BT should be much smaller than that shown in the upper panel of Figure 4.10.

This chapter focused on improving the cloud-clearing algorithm using the imager/sounder data. The results have demonstrated the advantage of optimal cloud-clearing over the traditional single-band N^* cloud-clearing. Comparisons between imager/sounder cloud-clearing and microwave/infrared sounder for cloud-clearing are beyond the scope of this dissertation. *Huang and Smith* [2004] have compared the traditional single-band N^* cloud-

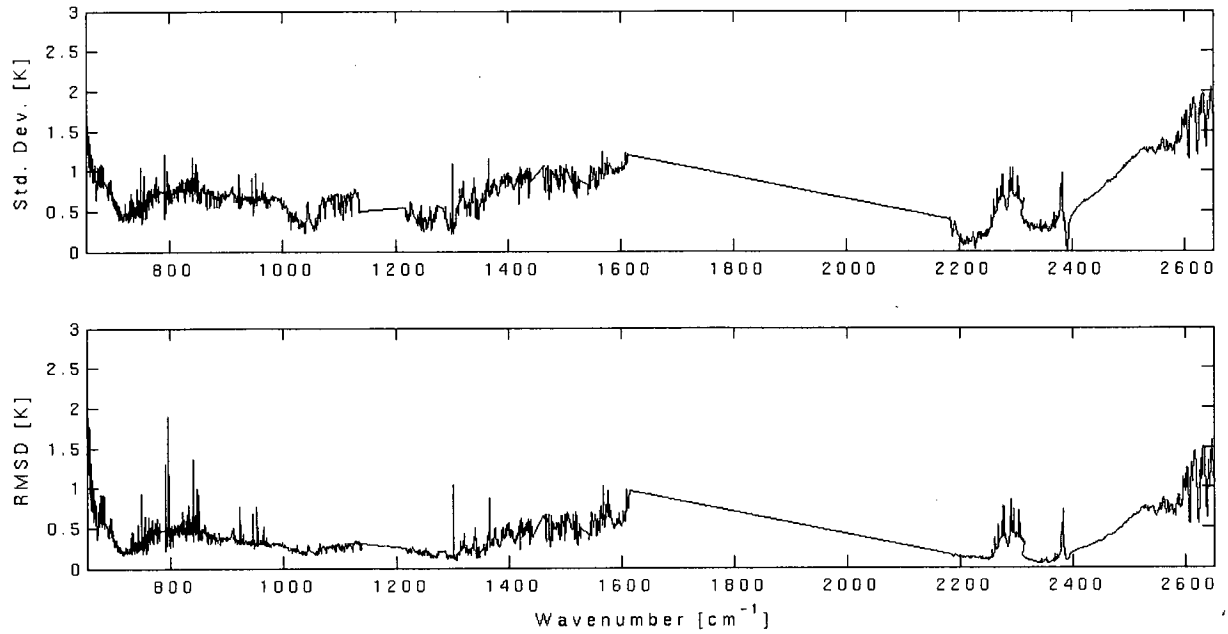

Figure 4.10 (Upper panel) Standard deviation between the AIRS cloud-cleared brightness temperature spectra and their nearby clear brightness temperature spectra along with the root mean square difference between the two-adjacent clear AIRS footprint pairs over the water of the granule (lower panel).

clearing approach with the operational Advanced Microwave Sounding Unit (AMSU)/AIRS cloud-clearing products. They found that MODIS is also very useful for the quality control of the operational AMSU/AIRS cloud-cleared brightness temperature spectrum. The imager/sounder cloud-clearing approach has the advantage that the infrared surface spectral information is implicitly being added to the calculation. If MODIS clear detection fails then the microwave approach has the advantage of not being susceptible to low uniform clouds.

Unlike using AMSU in AIRS cloud-clearing, the imager and sounder measure radiances at the same infrared spectral regions (Figure 4.1). There exists a direct relationship between an

imager infrared radiance, and a sounder infrared radiance spectrum for a given imager spectral band provides unique advantages for imager/sounder cloud-clearing. The advantages of imager/sounder cloud-clearing are:

(1) It is easier to find clear pixels in the smaller FOV of the imager within the sounder footprint, which is critical for the N^* calculation and the quality control on cloud-cleared radiances;

(2) Cloud-clearing can be achieved on a single-footprint basis (hence maintaining the spatial gradient information); and

(3) Imager infrared clear radiances provide tropospheric atmospheric information that enhances the effectiveness of cloud-clearing for infrared sounder cloudy radiances.

However, there are also limitations: (1) the cloud-clearing can only be done with partly cloudy footprints; (2) N^* has to be constant for the whole infrared spectrum; and (3) the surface and the atmospheric profile must be homogeneous within the pair of two adjacent footprints.

The cloud-clearing might fail when one of the above assumptions fails. For example, in the presence of ice clouds, the cloud-clearing might give spectrally inconsistent results due to N^* not being constant in the IR spectral region. In addition, when the radiance contrasts in the IR window region is too small, N^* tends to be 1 and the cloud-clearing can amplify noise rather than remove the cloud effects on the measurements. However, all these failures will be filtered by the quality control procedure [see Equation (4.16)]. The quality control is very important to assure that the final cloud-cleared radiances representing the clear part of the principal footprint

fit the MODIS infrared clear radiance observations in all infrared spectral regions simultaneously.

The cloud-clearing results a dependent on several factors. The operational MODIS cloud mask with 1-km spatial resolution used for determining the MODIS clear infrared radiances within the principal AIRS footprint is critical for the success of the cloud-clearing algorithm. Only confident clear MODIS pixels should be selected to determine the MODIS infrared clear-sky radiances. The daytime MODIS cloud mask is more accurate than the nighttime mask because of the use of visible and near-infrared bands [*Ackerman et al.*, 2008]. MODIS/AIRS collocation is also very important to assure the success of the cloud-clearing; mis-collocated MODIS clear pixels with the AIRS footprint may result in additional cloud-clearing errors. A reliable algorithm is necessary to provide good imager/sounder collocation. The time difference between the imager and sounder is another factor in cloud-clearing. Since MODIS and AIRS are in the same spacecraft, the time difference between MODIS and AIRS for a given AIRS footprint is small enough to assure the same clouds and atmospheric measurements are observed. The convolution error due to the AIRS spectral gaps or bad channels that are excluded in the calculation is another error source for MODIS/AIRS cloud-clearing. *Tobin et al.* [2006a, 2006b] characterized the bias due to the AIRS spectral gaps or bad channels; they found that window region bands 22, 31, and 32 have less bias, longwave CO_2 bands 33 through 36 have mean biases increasing to 1 K for band 36, and water vapor bands 28 and 27 have mean biases of 0.48 and 1.05 K, respectively. Those biases have not been taken into account yet when applying MODIS spectral response functions. The spectral response function and gap issues could be mitigated if a forward model for both instruments is used

[*Tobin et al.*, 2006b]. MODIS and AIRS calibration errors are the final factor to be considered when interpolating and using the MODIS/AIRS cloud-cleared radiances.

4.5 Summary

In this chapter, optimal cloud-clearing for sounder cloudy radiances using imager infrared clear radiances has been successfully demonstrated the advantages using collocated AIRS and MODIS observations. The necessary geolocation collocation of both sounder and imager are described, as well as the derivation of cloud fraction in the AIRS footprint using MODIS cloud product. About 20% of AIRS cloudy footprints (or 40% of the partly cloudy footprints) are successfully cloud-cleared with the help of MODIS high spatial resolution data. In the optimal imager/sounder cloud-clearing, the imager provides a cloud mask for sounder footprints while the multispectral imager infrared provides clear radiance observations to synergistically determine N^* and to be used as quality control. The conclusions of the handling cloudy high spectral radiances are as following:

(1) MODIS infrared spectral bands 22, 24, 25, 28, and 30 through 34 are used to determine N^* and quality control; more than 24% cloudy footprints are successfully cloud-cleared with the help of MODIS. The success rate is greater than 40%.

(2) The convoluted AIRS cloud-cleared radiances are compared with MODIS infrared clear radiance observations. The bias is less than 0.25 K for most MODIS infrared spectral bands, while the standard deviation is less than 0.5 K for almost all the MODIS infrared spectral

band. These numbers may be smaller when the statistics are performed with calibrated MODIS observations.

(3) Cloud-cleared radiances are compared with their nearby clear AIRS radiances. The standard deviation is within 1 K for most AIRS channels. Part of the standard deviation is due to the natural (atmospheric and surface) variability of the two clear adjacent footprints.

There are several further applications when the cloud effects in spectra are removed. For example, the clear-equivalent radiances can be used to retrieve atmospheric profiles following clear-sky procedure, or to be assimilated into the advanced numerical weather simulations. However, as mentioned above, the possible of noise amplification, and various quality control procedures applied on same cloudy spectrum may result in different cloud-cleared radiances. It is the best procedure to obtain the atmospheric profiles from both clear and cloudy radiances, and will be discussed in the followed chapter.

Chapter 5 The Inferring of Atmospheric Profiles from High Spectral Resolution Radiances

Atmospheric sounding from high spectral resolution radiances enables a study of the UT in pre-convective environments. The retrieval processes can be developed from a regression-based principle component analysis (PCA) scheme. The advantages of choosing regression PCA are a thinning of the high dimensional data, quality control, and appropriate noise filtering and estimation. This chapter establishes a clear radiance PCA algorithm, which is the foundation for cloudy retrieval in the second section. The third section focuses on the sounding enhancement by incorporating imager data. The inter-comparison between the retrieved profiles and model analysis fields as well as preliminary validation with co-located radiosonde observations (RAOB) are shown in the fourth section.

5.1 Atmospheric Profiling Scheme (I) – Clear Scene

The clear-sky sounding in this dissertation is based on the procedure of the International MODIS and AIRS Processing Package (IMAPP) [*Huang et al.*, 2004; *Weisz et al.*, 2007a] with refinements. The IMAPP is developed at Cooperative Institute for Meteorological Satellite Studies (CIMSS), University of Wisconsin-Madison, is a Direct Broadcast (DB) algorithm for efficiently processing raw data to Level-1B (calibrated radiances) and to Level-2 (retrieval) products in real-time. This processing software package was first released in 2000, and it is been used for a variety of application, including environmental monitoring, weather forecasting,

resources management, and education. The IMAPP AIRS retrieval process is based on a principle component regression (PCR) scheme, in which a set of regression coefficients are obtained through the principle component analyzed radiances and the atmospheric state. The desired parameters are retrieved by applying these coefficients to any AIRS radiance spectrum.

The retrieved parameters consist of atmospheric temperature, water vapor mixing ratio, and ozone mixing ratio profiles at 101 pressure levels from 0.005 to 1100 hPa listed in Table 3.3. In addition to the atmospheric profiles, the surface properties (e.g., surface skin temperature, and surface emissivity) are also included in the retrieval outputs. All these parameters are retrieved at AIRS single field-of-view (FOV) spatial resolution, which is 13.5 km at nadir. Since this retrieval process is designed to be performed for a clear-sky scene, it assumes that the AIRS footprint is clear if the derived cloud fraction (*CldFrac*) is less than 0.01. For those AIRS footprints with the *CldFrac* between 0.01 and 1 (overcast), a cloudy retrieval procedure will be applied, as introduced in Chapter 5.2. It should be noted that the collocated MODIS 1-km spatial resolution cloud mask product (MYD35) is used to derive the cloud fraction for each AIRS footprints (see Chapter 4.2).

A statistical eigenvector regression retrieval is used to obtain a fast and accurate first estimation of the atmospheric state in the clear sky. The complicated non-linear relationship between radiances and atmospheric parameters is described by the radiative transfer equation. If scattering by the atmosphere is neglected the infrared spectral region in clear skies, the true clear radiance R_ν exiting the earth-atmosphere system for a given AIRS infrared wavenumber, ν, is estimated by

$$R_\nu = \varepsilon_{s,\nu} B_{s,\nu} \tau_{s,\nu} - \int_0^{p_s} B_\nu d\tau_\nu(0,p) + (1-\varepsilon_{s,\nu}) \int_0^{p_s} B_\nu d\tau_\nu^* + R_\nu^{'} \quad , \tag{5.1}$$

where ε is the surface emissivity, B is the Planck radiance, which is dependent on temperature and wavenumber ν, $\tau(0,p)$ is the total transmittance from the top of the atmosphere to the atmospheric pressure p, the subscript s denotes the surface, $\tau^* = \tau_s^2/\tau$ is the downwelling transmittance, and $R_\nu^{'}$ represents the contribution of reflected radiation. Note that the transmittance is a function of the absorption coefficient, which in turn depends on the atmospheric temperature, pressure, and absorber amount. When the distribution of one atmospheric constituent is constant and well known (e.g., CO_2), one can solve Equation (5.1) for the temperature profile, and the remaining gas amounts can be estimated in a similar way. This is an ill-posed problem, which can usually be solved by a regression method.

To simplify the problem, it is assumed that a linear relationship between the atmospheric state vector [$X(nl,ns)$, deviation from the mean value $\bar{X}$] and the measurements [$Y(ns,nd)$, deviation from the mean value $\bar{Y}$]:

$$X = CY^T \quad , \tag{5.2}$$

where $C(nl,nd)$ is the matrix of the regression coefficients, nl stands for the number of levels, ns stands for the number of samples in the training datasets, and nd is the dimension of the measurements (i.e., the number of high spectral resolution channels used for retrieval). According to the method of least-squares the best fitting solution is the one minimizes the sum of the squared deviations from the data, i.e., $\sum\left(X - CY^T\right)^2$, and minimization yields

$C = XY(Y^T Y)^{-1}$. Here, the superscript T stands for the transpose of a matrix, and the superscript -1 stands for the matrix inversion.

In this study, the retrieval methodology utilized a principal component regression algorithm, i.e., an eigenvector regression algorithm [*Smith and Woolf*, 1976; *Huang and Antonelli*, 2001; *Goldberg et al.*, 2003; *Weisz et al.*, 2007a, 2007b]. This principal component statistical regression is used the following relationship instead:

$$X = CA^T \quad , \tag{5.3}$$

where the dimension of C is now (nl, npc) and

$$A = YU \quad . \tag{5.4}$$

The $A(ns, npc)$ stands for the matrix of compressed measurements, which are commonly called projection coefficients or principal component score, npc is the number of eigenvectors of the measurements, and $U(nd, npc)$ is the matrix containing the first few (npc) eigenvectors of the covariance matrix of Y. In the least squares solution, the minimization of $\sum\left(X - CA^T\right)^2$ results in the regression coefficients C:

$$C = X_{tr} A_{tr} \left(A_{tr}^T A_{tr}\right)^{-1} \quad , \tag{5.5}$$

where subscript tr refers to training data. Then the atmospheric parameters (X_{retr}) are retrieved according to

$$X_{retr} = \bar{X} + CA_{obs}^T \quad , \tag{5.6}$$

where A_{obs} is the matrix of the compressed observation from high spectral resolution measurements.

In this study, the input and output vectors for Y and X_{retr} in Equations (5.2) and (5.6) as predicators and predictands, respectively, consist of 1444 and 304 elements, which are listed in Table 5.1. Note the retrieval algorithm does not use the full set of AIRS channels, which has 2378 channels. The selection of subset channels is based on some instrument technical issues, which will be described later in this section.

Table 5.1 The predictors and predictands in the clear AIRS retrievals. Units are specified in the table.

Element No.	**Predictors**
1 – 1443	Used AIRS radiances [mW/m^2/cm^{-1}/ster] for PCR
1444	Surface pressure [hPa]
Element No.	**Predictands**
1 – 101	Temperature [K]
102 – 202	Moisture mixing ratio [g/kg]
203 – 303	Ozone mixing ratio [ppmv]
304	Surface skin temperature [K]

The key component in the principle component regression algorithm is obtaining the regression coefficients C, which are computed from compressed radiances. The eigenvector, or principle components (PCs), are obtained from the covariance matrix of simulated radiances, which are computed from the training profiles. For training the regression purpose, the SeeBor database [*Borbas et al.*, 2005] is used in the AIRS clear scene retrieval algorithm. The SeeBor database contains more than 15000 global profiles of temperature, moisture and ozone from

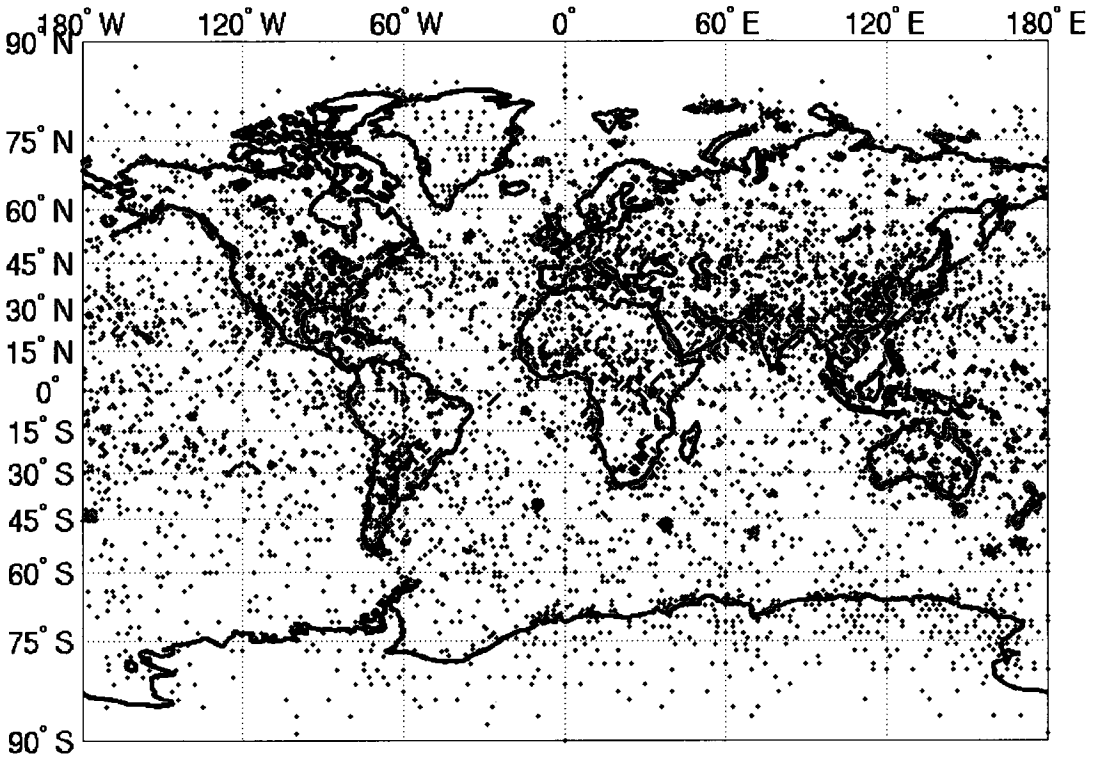

Figure 5.1 The spatial distributions of the SeeBor training database. The total number of the sample is 15704.

National Oceanic and Atmospheric Administration (NOAA)-88, ECMWF, the Thermodynamic Initial Guess Retrieval (TIGR)-3, ozonesondes and desert radiosondes, and a characterization of the elevation, ecosystem International Geosphere-Biosphere Programme (IGBP) classifications, and surface skin temperature. The surface emissivity at ten wavelengths (3.7, 4.3, 5.0, 5.8, 7.6, 8.3, 9.3, 10.8, 12.1, and 14.3 μm) are also included in this database by matching MODIS (MOD11) surface emissivities with laboratory measurements. Surface skin temperature over land has been assigned to each pixel in the training set using the established relationships between solar and azimuth angles at nadir and their surface air temperature. The ocean surface

skin temperature has been defined randomly as a function of sea surface temperature with zero mean and a standard deviation of 4 K. This database is wildly used at CIMSS for various instruments clear-sky regression retrievals for skin temperature, surface emissivities, and atmospheric profiles, when there is no real match-up data. The spatial distributions of the SeeBor database are shown in Figure 5.1, while the histograms of the months spread in both hemispheres are in Figure 5.2. It suggests the retrievals are globally applicable throughout the year.

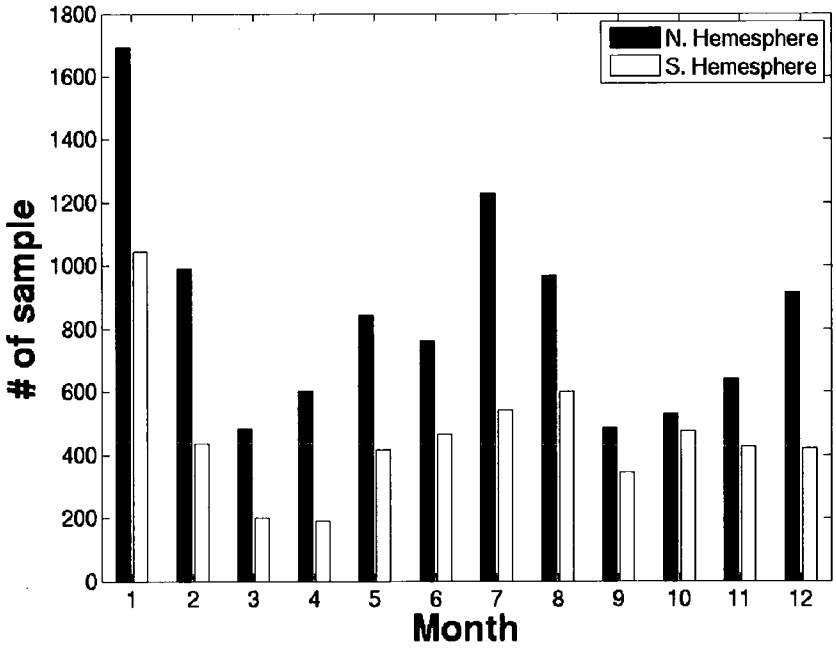

Figure 5.2 The histograms of the months of Northern and Southern hemispheres in Seebor database. The total numbers of the Northern and Southern hemispheres are 10142 and 5562, respectively.

There are several ways to determine the number of principle components to be retained. The most common way is to examine the eigenvalues, which are proportional to the amount of variance in the data, and retain only the leading factors (e.g., those with eigenvalues ≥ 1) [*Goldberg et al.*, 2003]. The number of the leading factors is often referred to as the number of independent pieces of information. In the experiments (simulated and non-simulated), it was found that the first eigenvalue accounts for 70% to 95% of the variability and all of the variance is explained by the first ten or so eigenvectors. However, ten eigenvalues are insufficient to reconstruct the radiances within the instrument noise level. *Goldberg et al.* [2003] commented that more than ten eigenvectors (but less than 100) are needed to properly reconstruct the measurements within the instrument noise level.

To exam the number of principle components can be optimized for both the reconstructed radiances within the instrument noise level and retrieval performance, a simulation for exploring these has been conducted. Because AIRS detectors may not work properly or consistently (e.g., a detector is not responding, or has high noise), those associated *bad* channels should not include in the retrieval. The individual channel properties of each AIRS channel can be archived online at http://disc.sci.gsfc.nasa.gov/AIRS/documentation/documentation.shtml. A set of 1688 NOAA National Environmental Satellite Data and Information Services (NESDIS) pre-selected channels is used in the simulations and retrieval process. AIRS Algorithm Theoretical Basis Document (ATBD) provides Noise Equivalent delta Temperature (NEdT) at a reference temperature 250 K for each channel. Because AIRS detectors have the channels with NEdT < 1 K with Gaussian noise characteristics, the channel with NEdT > 1 is considered a bad channel

and is not used in the retrieval. Those channels with wavenumber above 2400 cm^{-1} (i.e., wavelength less than 4.1667 μm) are not used due to the uncertainties caused by the reflected solar radiance during daytime. These result in a total of 1443 AIRS channels in the simulations and retrievals.

The surface pressure from the National Centers for Environmental Prediction (NCEP) Global Data Assimilation System (GDAS) is also used as a predicator. Through SeeBor database and the simulated radiances from forward model calculation of SARTA (see Chapter 3.3) at nadir, these retrieved parameters and radiances are paired and could be used for the evaluation of the number of PCs and the performance of retrieval results.

Figure 5.3 shows the root mean square error (RMSE) of the retrieved temperature and moisture vertical profiles versus the number of PCs used to compress the spectrum. The RMSE of certain variable at given pressure level is calculated as

$$RMSE\left(\hat{\phi},\phi\right)=\sqrt{\frac{\sum_{i=1}^{n}\left(\hat{\phi}_i-\phi_i\right)^2}{n}} \tag{5.7}$$

where $\hat{\phi}$ and ϕ are the value of retrieved parameter and the truth, respectively, and n is the number of the total samples in the calculation of RMSE. The RMSE of atmospheric temperature is generally lower than 1 K above 850 hPa beyond 75 PCs [Figure 5.3(a)], while the RMSE of relative humidity is lower 14% within the atmospheric boundary layer when 100 or more principle components are used [Figure 5.3(b)]. The vertical averaged RMSE for atmospheric temperature (from surface to 100 hPa) and moisture (from surface to 200 hPa)

along with the skin temperature versus the number of PCs used is shown in Figure 5.4(a). It is obvious that a greater RMSE reduction occurs when the first ten to twenty PCs is applied; the

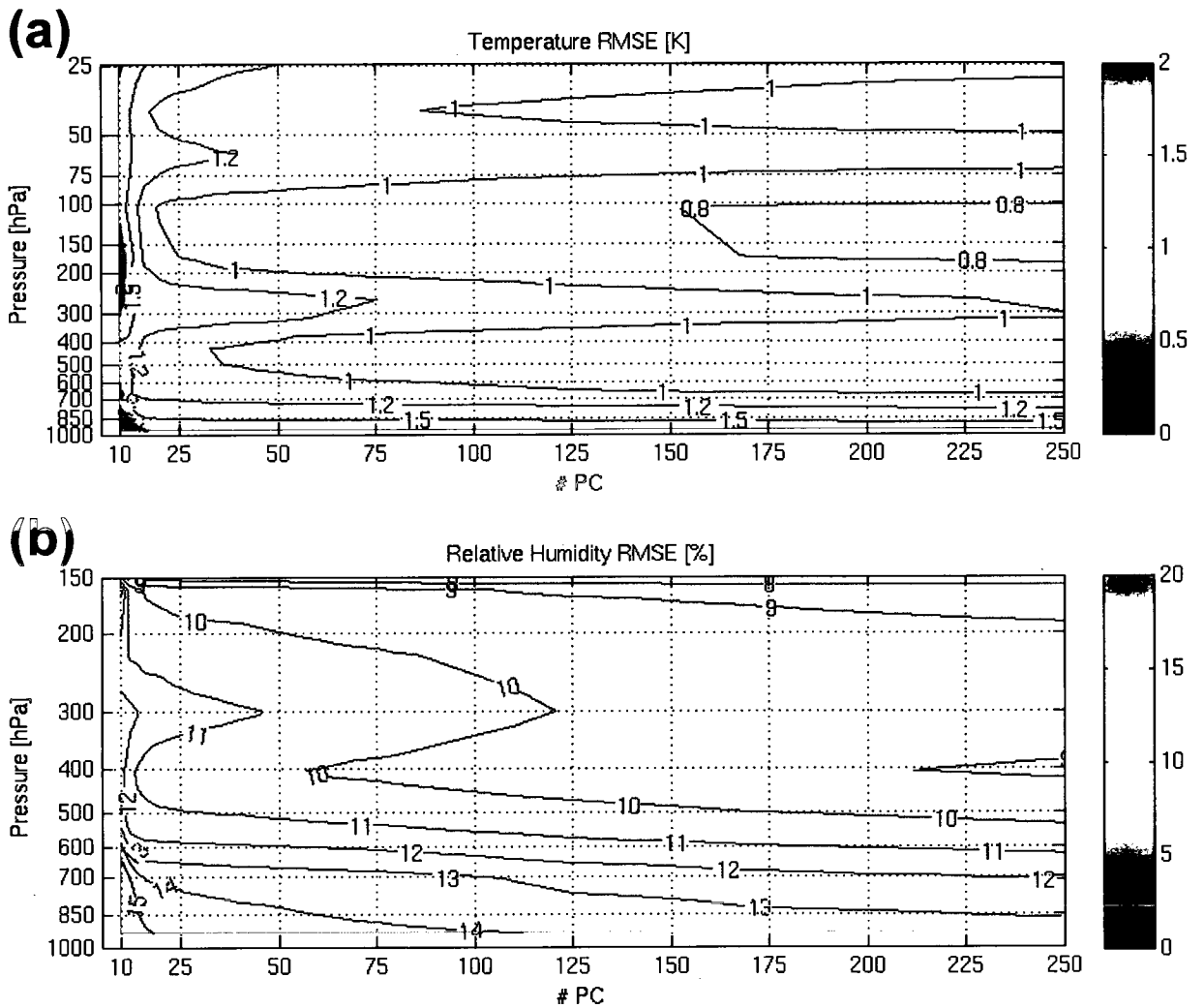

Figure 5.3 The RMSE of retrieved temperature [K] (a) and relative humidity [%] (b) using different number of principle components in the simulations. The retrievals were performed for the scanning angel at nadir view.

RMSE of these three variables do not have significant reduction beyond the using more PCs. The larger value of vertical averaged RMSE of temperature and moisture (greater than 1 K and 10% generally) are primarily due to the larger values in the lower troposphere (see Figure 5.3), and scaled relative humidity RMSE is shown in Figure 5.4. To further quantify the RMSE reduction verses the number of PCs, the RMSE gradient ($\overrightarrow{RMSE}$) is defined as

$$\overrightarrow{RMSE}_k = \frac{\|RMSE_k\| - \|RMSE_{k-1}\|}{npc_k - npc_{k-1}} \quad , \tag{5.8}$$

where $\|RMSE_k\|$ and $\|RMSE_{k-1}\|$ denote the vertical averaged RMSE for two retrievals which the total numbers of used PCs are npc_k and npc_{k-1}, respectively. The retrieval performance will consider to be saturated when the RMSE gradient ($\overrightarrow{RMSE}$) does not change with the increasing the total number of PCs.

Figure 5.4(b) indicates the RMSE gradient of temperature, relative humidity and skin temperature using Equation (5.8). A negative gradient corresponds to a reduction of the vertical averaged RMSE in Figure 5.4(b), and vice versa. The gradient is close to 0 when more than 60 principle components are used. This infers the use of 60 or more principle components may have similar retrieval performance in terms of RMSE.

A spectra-based principle component analysis (PCA) for the reconstruction of radiances is also conducted. A random noise in Gaussian distribution with zero mean and NEdT (converted to radiance units) as the standard deviation for each AIRS channel has been added to the simulated AIRS radiances. The normalized radiance using noise can be interpreted as the signal-to-noise ratio (SNR). When the SNR falls below unity, the noise has larger contribution

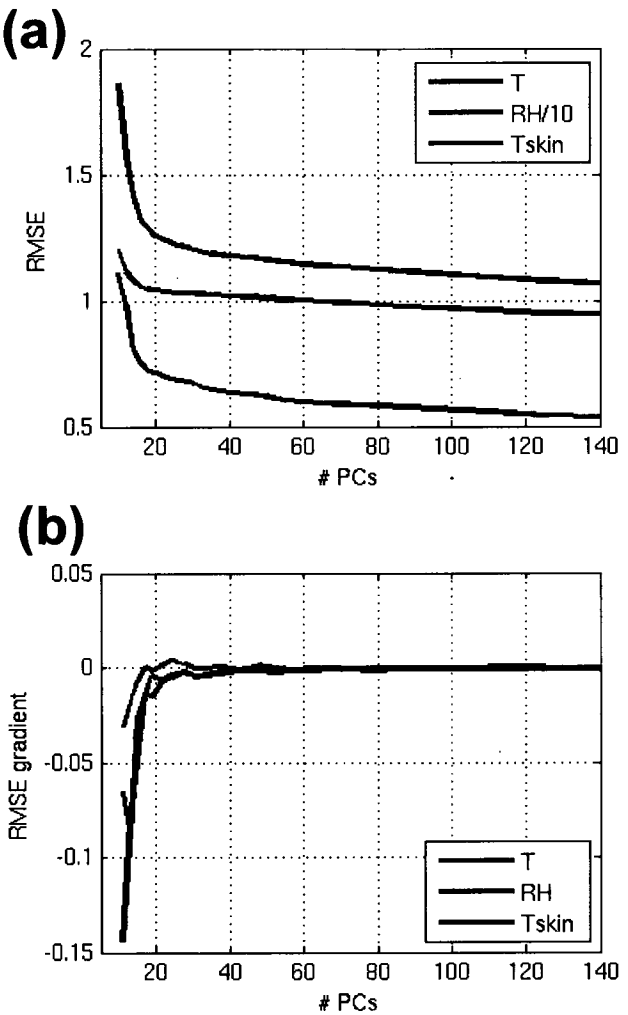

Figure 5.4 (a) The vertical averaged RMSE in Figure 5.3 for temperature [K] (blue curves), relative humidity [%] (scaled by 10, green curves), and surface skin temperature [K] for the first 140 principle components. The averaged RMSE for temperature and relative humidity are 100 hPa and 200 hPa to the surface, respectively. (b) The RMSE gradients for temperature, relative humidity and surface skin temperature in (a).

than the signal. An objective reconstruction score is introduced to evaluate how well the principle components reconstruct the original data. The reconstruction score (RS) is defined as

$$RS = \sqrt{\frac{1}{N}\sum_{i=1}^{N}\left(R_i - \hat{R}_i\right)^2} \quad , \tag{5.9}$$

where R_i and $\hat{R}_i$ are the noise-scaled radiances and reconstructed noise-scaled radiances for the AIRS ith channel, respectively, and N is the total number of channels used in the principle component analysis. A lower RS indicates a better noise filtering, and the unity RS suggests the full depiction of the noise. The noise reduction rate is simply equal to $(1-RS)$, and can be understood more intuitively as: 0 is no noise reduction while larger values tend to be more effective in noise elimination.

Both Figures 5.5(a) and 5.5(b) show the reconstruction score (blue curve) and noise reduction rate (red curve) between the leading principle component and up to the 1440 principle components. It is not surprising that the first few leading PCs do explain the most variance of original radiances. The noise reduction rate is up to 60% in the leading 200 principle components. The advantage of using more PCs gradually vanishes. Figure 5.5(b) expresses the detail of the leading 250 PCs, which is within the target range for this study. The noise reduction rate has the upper limit about 80% when 40 PCs are used in the simulations. The noise reduction rate is still above 75% and 70% if 80 and 100 PCs are applied, respectively. Both the reconstruction scores are considered at the reasonable levels because they are below the e-folding scale (i.e., 0.3679).

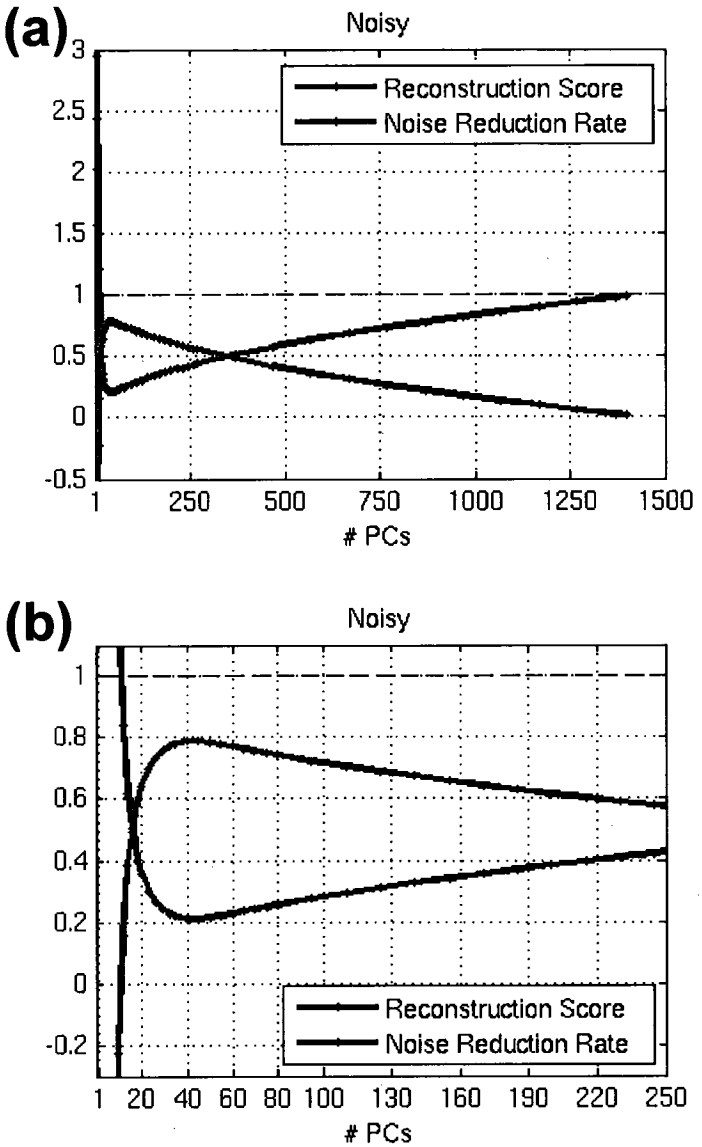

Figure 5.5 The reconstruction score (blue curves) and the noise reduction rate (red curves) between the leading principle component and up to (a) 1440 (b) 250 principle components.

Optimally choosing the number of PCs used should consider several factors, including the explanation of significant variability, the suppression of random noise, and the accurate estimation of the retrieved parameters. In this dissertation, 80 PCs is chosen for the eigenvector

regression retrieval algorithm because it reconstructs a reasonable estimate of the original radiance spectrum, limits the random noise in the reconstructed radiances (see Figure 5.5), and retains acceptable accuracy of the retrieved parameters (see Figure 5.4).

As the desired goal of this study is global application, different sets of regression coefficients for various surface and atmospheric conditions as well as the characteristics of optical geometry are suitable for resulting better retrievals than a single set of coefficients. The surface properties are categorized into over land and over water. In each category, the training dataset of radiances is divided into six classes on the basis of the averaged 11 brightness temperatures, which are all in the longwave window region and centered at 910 cm^{-1}. To reduce the impact of misclassification, an overlap of 1.5 K in the upper and lower neighboring classes is incorporated. The thresholds of each class for training the regressions are listed in the second column of Table 5.2. The regression coefficients are computed separately in these six classes, and further applied to the corresponding class of window brightness temperatures in the third column of Table 5.2.

Table 5.2 The classifications of brightness temperature (BT) for training the regressions and retrievals. The BT is the mean of eleven window channels centered at 910 cm^{-1}, and has the unit in Kelvin [K].

Class	Training	Retrieval
1	$BT \leq 256.5$	$BT \leq 255$
2	$253.5 < BT \leq 266.5$	$255 < BT \leq 265$
3	$263.5 < BT \leq 276.5$	$265 < BT \leq 275$
4	$273.5 < BT \leq 286.5$	$275 < BT \leq 285$
5	$283.5 < BT \leq 296.5$	$285 < BT \leq 295$
6	$293.5 < BT$	$295 < BT$

The AIRS has a scanning angle between –49.5° and +49.5° as described in Chapter 3.1. It will be a slant path for those scanning angles if not equal to zero, whereas the nadir view has a minimum atmospheric pathlength. The increasing atmospheric pathlength affects the radiance measurements due to the increased absorption of radiation before it reaches a satellite sensor, and the effects due to the differential slant paths are various from channel to channel. Therefore, besides categorized surface properties and classified brightness temperatures in the window region, classification based on the sensor scanning angle is considered as well. Regression coefficients are calculated for different scanning angles between 0° and 49.5°. A set of 20 scanning angles, α, which are pre-defined as

$$\sec(\alpha) = 1 + \Delta i \tag{5.10}$$

with $\Delta = \left(\sec(49.5^0) - \sec(0^0)\right)/10 = 0.027$, and $i = 0,1,2,...,19$ are used. The retrieved parameters ($X_{retr,1}$ and $X_{retr,2}$) are calculated for the upper and the lower neighboring scanning angle α_1 and α_2, respectively. The final retrieval (X_{retr}) resulting from the actual scanning angle α is obtained according to

$$X_{retr} = X_{retr,1} + \beta X_{retr,2} \tag{5.11}$$

where $\beta = \left(\sec(\alpha) - \sec(\alpha_1)\right)/\left(\sec(\alpha_2) - \sec(\alpha_1)\right)$.

To summarize, eigenvector regression or principle component regression with only a few principle components reduces the dimension of the regression problem, as well as the impact of

random noise while containing most of the information of the original data. Regression coefficients have been computed for two different surface properties (over land and over water), six brightness temperature classifications (Table 5.2), and 20 scanning angles. A total of 240 sets of regression coefficients have been generated for refining the outputs and optimizing the retrieval performance. The advantage due to the brightness temperature classifications has been given in *Weisz et al.*, [2007a].

Alternatively, a variational retrieval (e.g., *Rodgers* [2000]) can be included either as a stand-alone retrieval or used in combination with a statistical retrieval, where the regression provides the first guess for the variational approach. The variational retrieval implemented is a simultaneous iterative retrieval seeking the maximum posterior probability solution for the minimization of a cost function

$$J = \left(y(x) - y^m\right) \cdot E^{-1} \cdot \left(y(x) - y^m\right)^T + \left(x - x^b\right) \cdot B^{-1} \cdot \left(x - x^b\right)^T , \tag{5.12}$$

where x is the atmospheric state vector as calculated iteratively, x^b is the background atmospheric state, B is the covariance matrix associated with the background, y^m is the measurement vector, $y(x)$ is the forward model operator at a given state x, and E is the combined measurement and forward model error covariance. This physical-based retrieval approach can be sped up using an iterative convergence by introducing the discrepancy principle algorithm (e.g., *Li and Huang*, [1999]; *Li et al.*, [2000]).

5.2 Atmospheric Profiling Scheme (II) – Cloudy Scene

The AIRS measured infrared radiances are typically not used for sounding retrievals under cloudy-sky scenes because of the strong absorption and emission by clouds. However, the probability of an AIRS footprints being completely clear is about 10%, due to the relative poor spatial resolution of 13.5 km at nadir [*Huang and Smith*, 2004]. To extend the sounding retrievals from clear to cloudy conditions, cloudy-sky retrieval is developed to explore the performance of AIRS under both thin and thick cloud conditions. In this section, thin clouds are defined as the cloud optical thickness (COT) less than 1.5, and all the other cloud cases are considered as optical thick clouds.

The cloudy retrieval algorithm is based on *Weisz et al.*, [2007b] with refinements, and is similar to the clear-sky retrieval algorithm as described in Chapter 5.1. It is also a principle component regression scheme, in which a set of regression coefficients are obtained through the principle component analyzed cloudy radiances, the atmospheric state, and cloud optical properties. The desired parameters can be retrieved by applying these coefficients to any spectrum of AIRS cloudy radiance measurements.

In the training process, the AIRS cloudy infrared radiances are calculated with given atmospheric profiles of temperature, moisture and ozone, sensor's scanning angle, surface skin temperature, surface pressure, cloud top pressure, cloud optical thickness at 0.55 μm, effective cloud particle size using the equation for radiative transfer [*Zhou et al.*, 2007]

$$R_\nu^c = R_{0,\nu} F_{T,\nu} \tau_{tc,\nu} + R_{c,\nu} \tau_{tc,\nu} + R_\nu^* + R_\nu^{*\downarrow} F_{R,\nu} \tau_{tc,\nu} \tag{5.13}$$

where R_ν^c is exiting radiance at the top of the atmosphere. $R_{0,\nu}$, $R_{c,\nu}$, R_ν^*, and $R_\nu^{*\downarrow}$ are upwelling emission below the cloud, emission from the cloud, upwelling emission from the atmosphere above the cloud, and downwelling emission from the atmosphere above the cloud, respectively. $F_{T,\nu}$ and $F_{R,\nu}$ are the cloud transmissive and reflective functions. The subscript ν denotes the given AIRS wavenumber. The upwelling emission $R_{0,\nu}$ includes the surface emission, the atmospheric upwelling below the cloud, and the downwelling emissions by the cloud and the atmosphere (both above and below the cloud), which are reflected back to the space by the surface.

In the SeeBor training database [*Borbas et al.*, 2005], most profiles are collected and pre-quality controlled in clear-sky conditions. To establish the cloudy profiles, clouds are added at selected a pressure level according to their relative humidity between 100 and 900 hPa. This results in a cloudy-sky training dataset of approximately 6200 profiles. Among these profiles, ~2160 profiles are suitable for ice clouds (those cloud top pressure < 500 hPa), while ~4010 profiles are for liquid water clouds (cloud top pressure > 400 hPa).

The ice clouds are assigned with COT values as 0.04, 0.16, 0.36, 0.64, 1.0, 1.44, 1.96, and 2.56, whereas the liquid water cloud are given COT for 0.06, 0.24, 0.54, 0.96, 1.5, and 2.16. For ice clouds, *Heymsfield et al.*, [2003] suggested a relationship between the cloud effective particle size in diameter (CDe):

$$CDe = \frac{A\tau^\alpha}{\tau - B\tau^\alpha} \tag{5.14}$$

with the empirical constants $A = 18.7652$, $B = 0.32522$, and $\alpha = 1.1905$. The τ stands for the COT at 0.55 μm in Equation (5.14). *Li et al.* [2005] suggested a 10% random variation is added to *CDe*. Therefore, a range of *CDe* between 10 and 40 μm was obtained for ice clouds. For liquid water clouds, *Li et al.* [2005] also recommended the *CDe* could be randomly assigned between 5 and 35 μm, with a mean of 30 μm and a standard deviation of 10 μm. These conducts a training dataset with ~17000 and ~24000 profiles for ice and liquid water clouds at given sensor's scanning angle.

A set of cloudy radiances can be calculated through the cloudy radiative transfer model using the cloudy-sky profiles above. The cloud optical thickness at visible 0.55 μm is in the model input, while the infrared COT for each AIRS channel can be derived from the visible COT. The cloudy radiance for a given AIRS channel can be computed by coupling the clear-sky optical thickness and the cloud effect. The clear-sky optical thickness is derived from the fast radiative transfer model SARTA as outlined in Chapter 3.3. Follow the procedure for obtaining the clear regression coefficients in Chapter 5.1, the cloudy regression coefficients are obtained by using Equation (5.5). The six classifications using averaged brightness temperature in longwave window region (Table 5.2) and scanning angle classifications are still applied. However, there is no separation in surface properties for over land and over water because the spectrum is more sensitive to the cloud parameters. The coefficient sets are computed instead for ice and liquid water clouds independently. Note the retrieved parameters (i.e., predictands) are with additional cloud properties (CTP, COT, and *CDe*), and are updated in Table 5.3. The assignment of COT and *CDe* to a profile is similar to *Weisz et al.*, [2007b] and *Zhou et al.*, [2005].

Table 5.3 The predictors and predictands in the cloudy AIRS retrievals. Units are specified in the table.

Element No.	Predictors
1 – 1443	Used AIRS radiances [mW/m^2/cm^{-1}/ster] for PCR
1444	Surface pressure [hPa]
Element No.	**Predictands**
1 – 101	Temperature [K]
102 – 202	Moisture mixing ratio [g/kg]
203 – 303	Ozone mixing ratio [ppmv]
304	Surface skin temperature [K]
305	Cloud top pressure [hPa]
306	Cloud optical thickness at 0.55 μm
307	Effective cloud particle size in diameter [μm]

When a given AIRS radiance spectrum is determined to have a fractional cloud cover of greater than 0.01 (i.e., *CldFrac* > 0.01), the cloudy regression coefficients are applied to the AIRS BT spectrum, and the retrieval is performed as the clear algorithm in Chapter 5.1. In the cloudy scene, a cloud phase detection method based on an infrared technique [*Strabala et al.*, 1994] is applied to the AIRS BT spectrum for identifying ice cloud, liquid water clouds or mixed phase clouds. After the cloud phase is determined, the appropriate set of coefficients is applied for cloudy sounding retrieval. The clouds are treated as ice clouds if the footprint is identified as mixed phase. If the retrieved COT is less than 1.5 (i.e., optically thin cloud), the sounding parameters including temperature, humidity, and ozone profiles as well as surface skin temperature in Table 5.2 are output from the top of the atmosphere down to the surface. In all other cloud cases (i.e., optically thick clouds), the sounding parameters are retrieved down to the CTP level.

Although the cloud forward model is still undergoing, the cloudy sounding can be developed from the experience in the clear regression retrievals. The cloudy principle

component regression algorithm provides a fast estimation of atmospheric profiles, cloud and surface properties. The preliminary inter-comparisons have shown good agreement between the atmospheric profiles from AIRS retrieved result and ECMWF model analysis, and the cloud top heights from AIRS, MODIS, CloudSat and Cloud-Aerosol Lidar and Infrared Pathfinder Satellite Observation (CALIPSO) (e.g., *Weisz et al.*, [2007b, 2007c]). Therefore, the retrieved products can be used to explore certain meteorological phenomena.

5.3 The Enhancement of Clear and Cloudy Soundings

The operational AIRS sounding product is based on 3 × 3 FOVs [*Susskind et al.*, 2003], which is useful for numerical predication and climate studies, but this spatial resolution lacks the capability to address certain meteorological applications such as preserving spatial gradients for monitoring and predicting mesoscale features. Since the AIRS footprints may contains not only a clear scene but also a cloudy one, sounding retrievals using AIRS-alone measurements for all sky conditions is quite challenging. Although the cloud-clearing algorithm (see Chapter 4) may increase the footprints with clear-equivalence radiances, the retrieval procedure may encounter the amplified noise problem.

It is commonly found that MODIS clear observations are within a given AIRS cloudy footprint, as sketched in Figure 5.6. Synergistic use of AIRS cloudy measurement and MODIS clear observations is an extension of cloud-clearing approach, where MODIS determined clear-sky pixels provide additional information to the AIRS measurement. The main differences between the AIRS-alone sounding algorithm [*Zhou et al.*, 2007; *Weisz et al.*, 2007a, 2007b] and

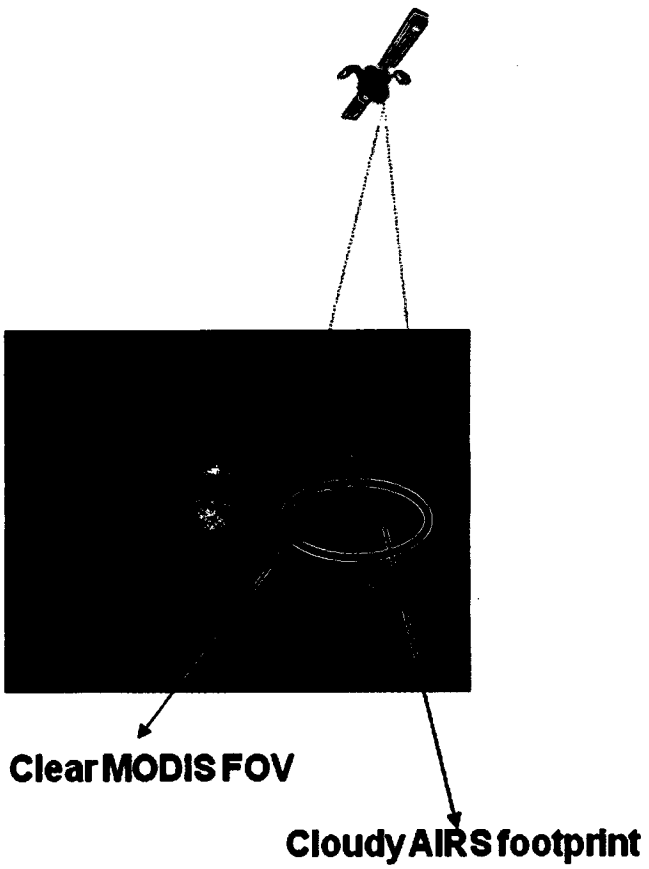

Figure 5.6 Sketch diagram for a sample AIRS partly cloudy footprint with clear MODIS observations within the collocated AIRS FOV. Note: the picture was taken from an aerial view, and the diagram is not to scale.

AIRS/MODIS synergistic sounding algorithm presented in this section. They are (1) adding MODIS clear-sky infrared brightness temperature information when the AIRS single FOV is only partially cloudy as determined by MODIS cloud mask [*Li et al.*, 2004; *Liu et al.*, 2008], (2) separate regression coefficients for sounding retrievals based on the cloud properties or cloud phases, and (3) assigning the cloud microphysical properties in terms of COT and effective cloud particle diameter (CDe) to compute a large training dataset of cloudy radiances. High

spectral resolution infrared alone algorithms (see Chapter 5.1 and 5.2) have been developed for clear and cloudy sky conditions. Sounding below cloud is less accurate due to limited information below the cloud base and the uncertainty of cloudy radiative transfer model. Inclusion of MODIS clear infrared radiances can help in the definition of the cloud parameters and condition the structure of sounding below the clouds and increase the accuracy of the solution.

To obtain a fast and accurate first estimate of the atmospheric state, a statistical eigenvector regression based on AIRS high spectral resolution measurements with high spatial resolution MODIS observations as additional predicators (i.e., synergistic AIRS and MODIS retrieval algorithm) was developed. The synergistic algorithm starts with the AIRS stand-alone clear and cloudy retrieval software (see Chapters 5.1, and 5.2), which retrieves atmospheric conditions, surface parameters and cloud-top height. The regression training set [*Borbas et al.*, 2005] consists of 15704 global profiles of temperature, moisture and ozone at 101 vertical levels from 0.005 to 1100 hPa, as well as the surface skin temperature and surface emissivity. The associated clear-sky radiances at AIRS spectra were simulated using Stand-alone Radiative Transfer Algorithm (SARTA) [*Strow et al.*, 2003], while the cloudy radiances were computed with a fast high spectral cloudy radiative transfer model developed under the joint efforts of the University of Wisconsin- Madison and Texas A&M University [*Wei et al.*, 2004]. The clear radiative transfer calculation of the MODIS spectral band radiances was performed by using a transmittance model called Pressure-Layer Fast Algorithm for Atmospheric Transmittance (PFAAST) [*Hannon et al.*, 1996]. All these three radiative models have been introduced in Chapter 3.

To train the cloudy-sky regression, the AIRS cloudy radiances were simulated using a large number of atmospheric profiles with the following combinations of cloud properties. Each cloudy profile of the training set is assigned a cloud-top pressure (CTP) between 100 and 900 hPa based on the relative humidity profile; where CTP < 500 hPa are assumed to be ice clouds and CTP > 400 hPa are assumed to be liquid water clouds. For the cloud properties assignments of ice and water clouds, they are followed the procedures in Chapter 5.2.

Once the AIRS BTs have been calculated, a regression is generated relating the brightness temperatures to the profiles. In the synergistic algorithm, besides the AIRS eigenvectors, eleven clear synthetic MODIS infrared spectral band brightness temperatures and associated quadratic terms [*Seemann et al.*, 2003] are added as additional predicators. In clear scenes, the coefficients are calculated for over water and land separately. Due to the spectral complexity of clouds, the coefficients are done for liquid water and ice cloud phases separately. In addition these classifications are based on the surface type or cloud phase; the training set is also classified based on the averaged AIRS brightness temperature in the longwave window region that has 11 channels centered at 910 cm^{-1}, and 20 AIRS sensor scan angles. The surface pressure from the NCEP GDAS is also used as a predicator. Table 5.4 summarized the predicators and predictands in the synergistic AIRS and MODIS retrieval algorithm.

The synergistic use of AIRS and MODIS for atmospheric sounding algorithm at AIRS single FOV spatial resolution is outlined in Figure 5.7. The main input data include AIRS, MODIS Level-1B (L1B) measurements and MODIS cloud mask product. Following the procedure as described in *Liu et al.* [2008], the AIRS clear-sky procedure is applied for those AIRS FOV with $CldFrac = 0$ because the redundant MODIS clear BTs reduce the retrieval

accuracy. The AIRS cloudy alone procedures is applied for those AIRS FOVs with $CldFrac \geq 0.99$, because there is very limited or no MODIS clear measurements within the AIRS FOV. For those AIRS FOVs have $0 < CldFrac \leq 0.01$ or $0.01 < CldFrac < 0.99$, the synergistic AIRS and MODIS clear procedure or cloudy procedure are used, respectively.

Table 5.4 The predictors and predictands in the synergistic use of AIRS and MODIS retrievals. Units are specified in the table.

Element No.	Predictors
1 – 1443	Used AIRS radiances [mW/m^2/cm^{-1}/ster] for PCR
1444	Surface pressure [hPa]
1445 – 1455	Averaged MODIS clear brightness temperature [K]
1456 – 1466	Quadratic of averaged MODIS clear brightness temperature
Element No.	**Predictands**
1 – 101	Temperature [K]
102 – 202	Moisture mixing ratio [g/kg]
203 – 303	Ozone mixing ratio [ppmv]
304	Surface skin temperature [K]
305	Cloud top pressure [hPa]
306	Cloud optical thickness at 0.55 μm
307	Effective cloud particle size in diameter [μm]

The synergistic use of AIRS and MODIS for atmospheric sounding algorithm at AIRS single FOV spatial resolution is outlined in Figure 5.7. The main input data include AIRS, MODIS Level-1B (L1B) measurements and MODIS cloud mask product. Following the procedure as described in *Liu et al.* [2008], the AIRS clear-sky procedure is applied for those AIRS FOV with $CldFrac = 0$ because the redundant MODIS clear BTs reduce the retrieval accuracy. The AIRS cloudy alone procedures is applied for those AIRS FOVs with $CldFrac \geq 0.99$, because there is very limited or no MODIS clear measurements within the AIRS FOV. For those AIRS FOVs

have $0 < CldFrac \leq 0.01$ or $0.01 < CldFrac < 0.99$, the synergistic AIRS and MODIS clear procedure or cloudy procedure are used, respectively.

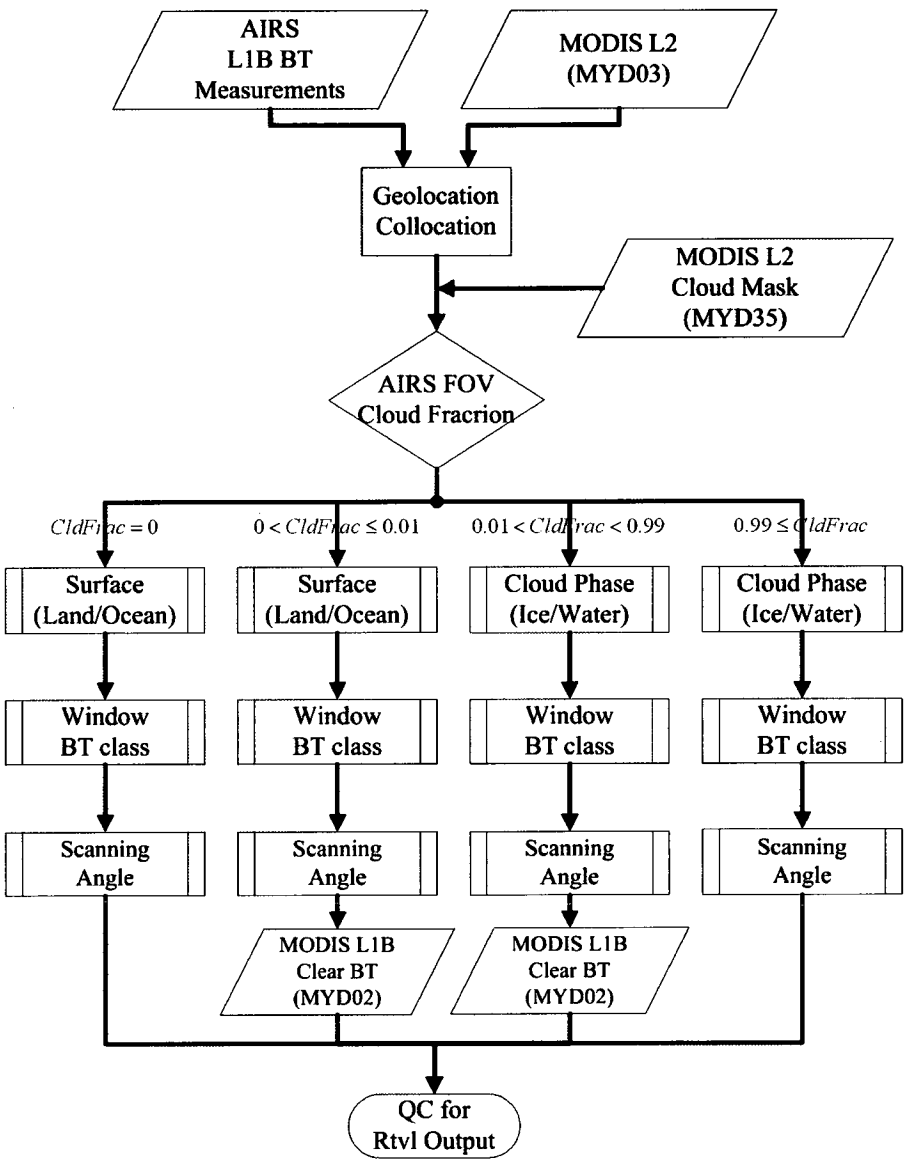

Figure 5.7 Flowchart of the AIRS/MODIS synergistic atmospheric profile algorithm.

If the AIRS footprint is clear, then the clear regression coefficients are applied to the brightness temperature spectrum, and the clear-sky retrieval is obtained. If the footprint is cloudy, a cloud phase detection method based on an IR technique [*Strabala et al.*, 1994] is applied to the AIRS brightness temperature spectrum for identifying ice clouds, water clouds or mixed phase clouds. After the cloud phase is determined, the appropriate set of coefficients is applied for cloudy sounding retrieval. The clouds are treated as ice clouds if the footprint is identified as mixed phase. For clear skies, or if the retrieved COT is less than 1.5 (i.e., optically thin cloud), the sounding parameters, including temperature, humidity and ozone profiles as well

Table 5.5 The MODIS predicators and their uncertainty at reference temperature 285 K used in the MODIS clear alone, and synergistic AIRS and MODIS regression procedures. BT is brightness temperature and has the unit in Kelvin [K].

MODIS Predicator	Noise / Uncertainty
Band-25–24	0.75 K
Band-27	0.75 K
Band-28	0.75 K
Band-29	0.189 K
Band-30	0.75 K
Band-31	0.167 K
Band-32	0.192 K
Band-33	0.75 K
Band-34	0.75 K
Band-35	0.75 K
Band-36	1.05 K

as surface skin temperature and surface emissivities at 10 infrared wavenumbers, are output from the top of the atmosphere down to the surface. In all other cloud cases (i.e., optically thick clouds), the sounding parameters are retrieved down to the CTP level.

To analyze the information contribution from various predicators to the retrieval, a simulation study was performed. In the simulation, 90% of the NOAA-88 profile data samples were used for training, while radiances calculated from the remaining 10% were used for testing the retrieval algorithm. The noise added in the AIRS simulation is the same as the noise given in the NESDIS AIRS ATBD (see Chapter 5.1), while the noise included for MODIS clear BT is from operational algorithm for *Aqua* (see Table 5.5). Figure 5.8 shows the root-mean-error (RMSE) of retrieved vertical profiles of atmospheric temperature, moisture and ozone mixing ratio compared with the actual profiles at 101 pressure levels. The AIRS clear alone algorithm (black curves) has the lowest RMSE in temperature and moisture retrievals, and this is the desired purpose from the high spectral resolution sounder. The AIRS cloudy alone algorithm (blue curves) has larger RMSE than the AIRS cloudy alone algorithm in the simulations due to the strong absorptions in the clouds. The RMSE for synergistic AIRS and MODIS algorithm has improvement due to the inclusion of MODIS clear information, and is comparable to that from AIRS alone clear scheme, where the RMSE is approximately 1 K and increases to 2 K near the surface. Moisture retrieval accuracy decreases with height from an RMSE maximum 15% at the lowest levels. The RMSE for the ozone profiles reaches a maximum of 0.775 ppmv at the highest levels. The impacts due to the addition of the MODIS clear data are mainly below 200 hPa for both temperature and moisture retrievals. The RMSE for MODIS clear alone algorithm is shown for comparison, and is similar to the work for EOS *Terra* MODIS by *Seemann et al.* [2003].

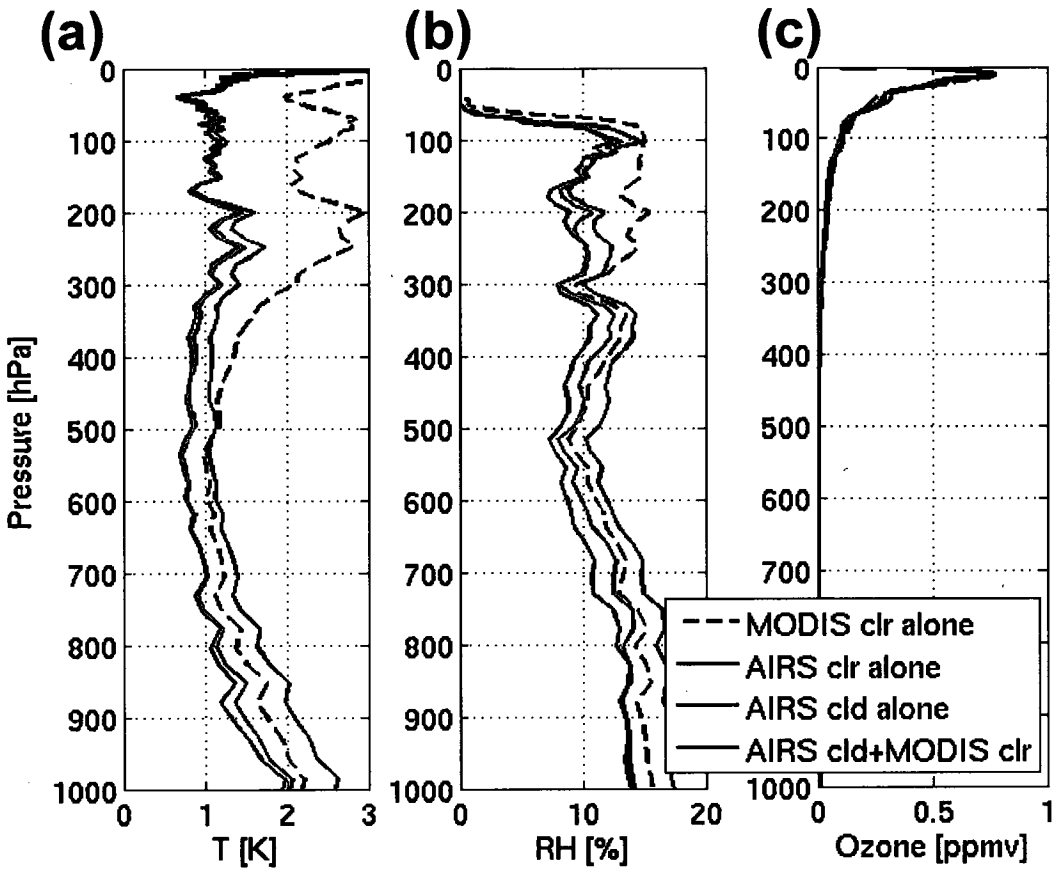

Figure 5.8 RMSE of actual profile compared with retrieved profiles using MODIS clear (dashed black curves), AIRS clear alone (solid black curves), AIRS cloudy alone (blue curves), and synergistic use of AIRS and MODIS (red curves) algorithms of temperature [K] (a), relative humidity [%] (b), and ozone [ppmv] (c). Profiles were taken from an independent sample of 10% of the NOAA-88 data and retrieved on radiances computed from each profiles.

5.4 Results and Preliminary Validation

The root-mean-square difference (RMSD) and bias between single FOV sounding retrievals (from AIRS-alone and synergistic AIRS/MODIS algorithms), and 6-hour ECMWF analysis are calculated to assess the performance of algorithms. Only AIRS footprints within one hour of ECMWF analysis are used for these statistical comparisons. Both Figures 5.9(a)

and 5.9(b) show the RMSD and bias of temperature and column precipitable water, respectively, of three atmospheric layers for thin ice cloud over water surface where the atmosphere, surface, and cloud properties are assumed homogeneous within the AIRS single FOV. The synergistic algorithm has both lower RMSD and smaller bias than the AIRS-alone method. There is an increasing trend of RMSD and larger bias when the cloud fraction increases, as the clear-sky MODIS pixels provide less information about the AIRS single FOV cloudy scene. Increasing the cloud fraction within AIRS single FOV causes alternations of the weighting functions from the clear scene values. Synergistic use of MODIS information not only reduces the RMSD but also minimizes the bias in cloudy sounding, especially in the boundary layer.

Daytime AIRS and MODIS observations on 09 May 2003, which contains a mesoscale frontal system [Figure 5.10(a)], was chosen to further illustrate the retrieval results. A cross-section from south to north is examined and evaluated by comparing the MODIS true color composited image of the scene [Figure 5.10(c)]), with the green line showing the location of the cross-section of retrieved relative humidity profiles. The soundings are only displayed to the CTP levels when optically thick clouds are present. Although AIRS-alone method [Figure 5.11(b)] can retrieve a moist layer approximately at 550 hPa between latitudes 34.5° and 35.5°, the synergistic AIRS and MODIS [Figure 5.11(c)] method retrieves profiles through an area identified as broken clouds in the MODIS true color image [Figure 5.10(c)] and MODIS cloud mask [Figure 5.10(b)].

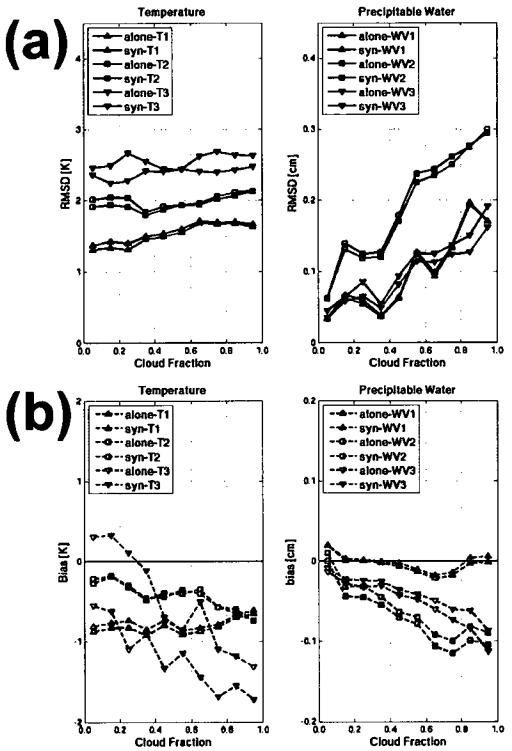

Figure 5.9 Global statistics of room-mean-square (a) difference (RMSD) and (b) bias between AIRS alone (blue curves), synergistic (red curves) retrievals (2571 profiles) and 6-hour ECMWF analysis fields of temperature (left panels) and column precipitable water (right panels) on 15 Aug 2007 over the water and thin ice cloud condition with respect to AIRS SFOV cloud fraction at 0.1 binning of three atmospheric layers. The legends of T1, T2, and T3 (WV1, WV2, and WV3) are the statistics at atmospheric layers for temperature (column precipitable water) at 75–200 hPa (300–700 hPa), 200–800 hPa (700–900 hPa), and 800 hPa (900 hPa) to surface level respectively.

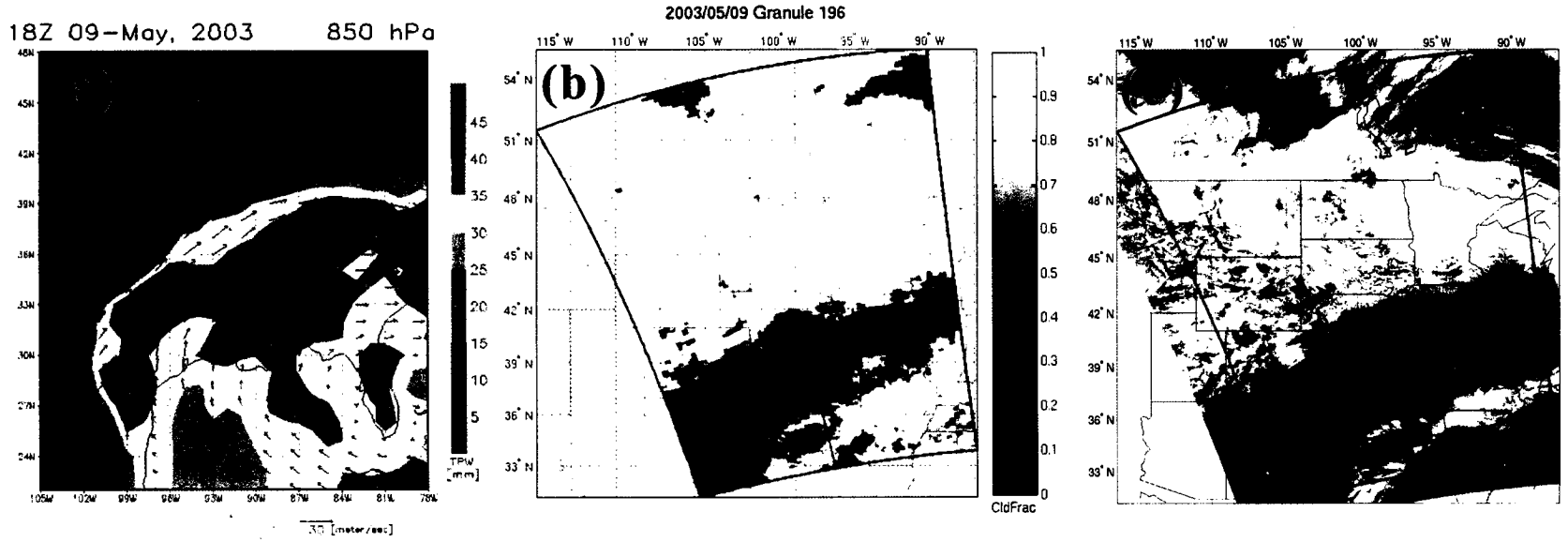

Figure 5.10 (a) The 850 hPa wind vector overlaid on the total precipitable water (TPW) in color from NCEP analysis at 18 UTC 09 May, 2003. (b) The derived cloud fraction of AIRS granule 196 from MODIS 1-km spatial resolution cloud mask product (MYD35) on the same day. (c) Composited true color using *Aqua* MODIS reflectance from 1935–1945 UTC 09 May 2003. Relative humidity vertical cross sections along the green line are shown in Figure 5.10. The red cross in (b) denotes the location of ARM SGP site.

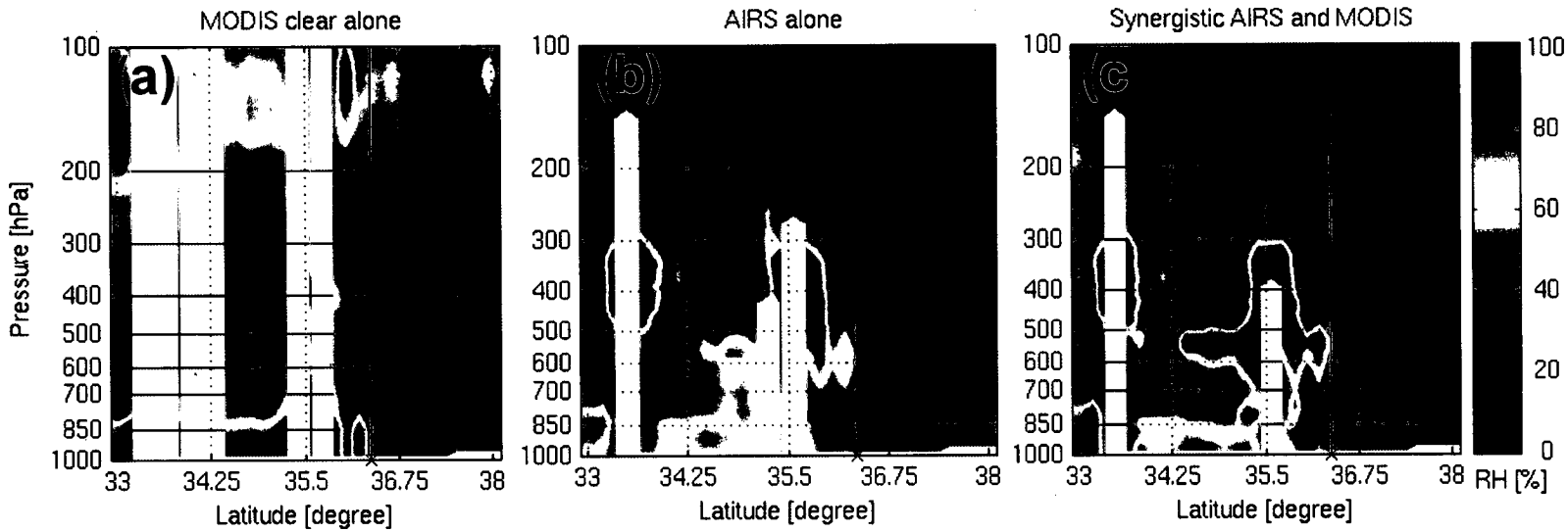

Figure 5.11 The transect cross-sections of relative humidity retrieval alone the green line in Figure 5.9 from (a) MODIS alone algorithm, (b) AIRS-alone algorithm, and (c) synergistic AIRS and MODIS algorithm

The retrieved profiles are compared with a radiosonde measurement at 2230 UTC launched at the Southern Great Plains (SGP) Cloud And Radiation Testbed (CART) site at Lamont, Oklahoma. For this particular cloudy scene, the retrieved temperature profile is not significantly affected by adding MODIS clear radiance information when compared with that from both AIRS cloudy alone and synergistic methods in Figure 5.12(a). However, for water vapor the synergistic method captures more details in the vertical profile than the AIRS-alone

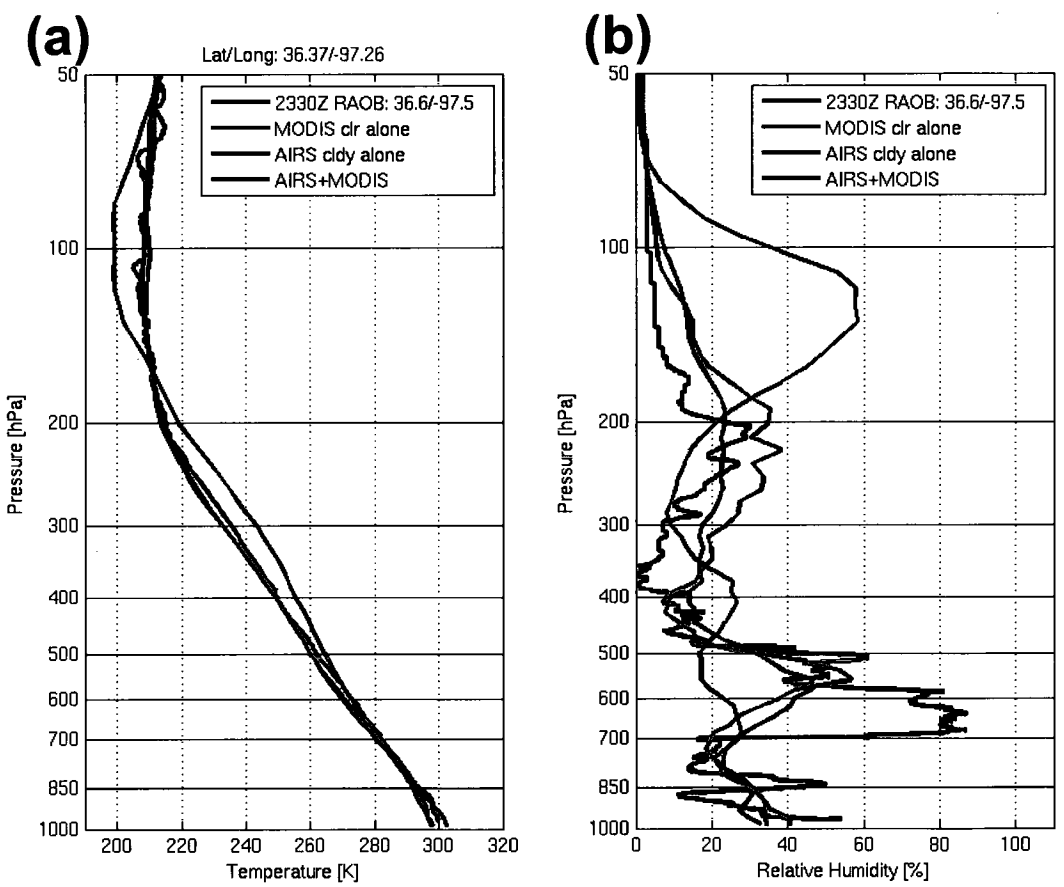

Figure 5.12 The retrieved (a) temperature and (b) moisture sounding profiles (green, blue and red lines refer to the result from MODIS clear alone, AIRS cloudy alone, and synergistic AIRS and MODIS retrieval methods, respectively) compared with one co-located SGP CART radiosonde measurement (black) denoted as the location (black solid lines) in Figure 5.11.

method [Figure 5.12(b)]. The cloud layer and an upper level moist layer (relative humidity of approximately 40%) around 200 hPa levels [Figure 5.12(b)] are consistence with the in-situ radiosonde observations. The combined AIRS/MODIS retrieval also better represents the relative humidity in the lowest layer. Differences between the retrievals and radiosonde observations are partly caused by the spatial and temporal differences in the comparisons.

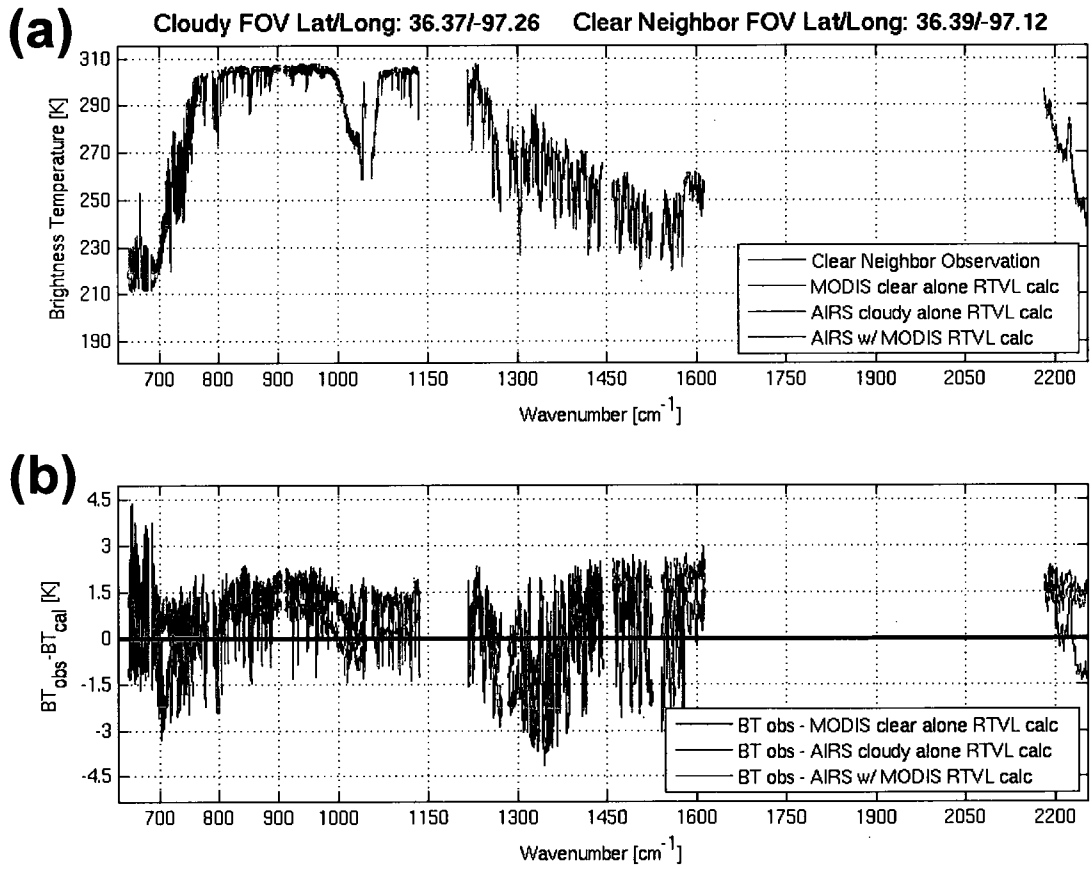

Figure 5.13 (a) Comparisons between observed AIRS clear-sky neighbor (blue) and calculated SARTA clear brightness temperatures by using MODIS clear alone (green), AIRS cloudy alone (red), synergistic AIRS and MODIS (cyan) retrievals. (b) Brightness temperature differences for the neighboring clear-sky observation and the clear-sky calculations.

To further investigate the performance of the sounding retrieval algorithms, the calculated AIRS clear brightness temperature using the retrieved surface parameters and profiles are compared with nearby clear-sky observations [Figure 5.13]. The calculated top-of-atmosphere (TOA) BTs, among the three methods are all close to the clear-sky observations, but the synergistic method has the smallest BT differences (BTDs) in the carbon dioxide (CO_2) absorption, window and ozone spectral regions. The BTDs of the synergistic method are also close to the atmospheric spectral natural variability (not shown) for any two clear adjacent FOVs within the granule. Larger BTDs for MODIS alone retrievals in 650–750 cm^{-1} CO_2 and 1000–1100 cm^{-1} ozone channels demonstrate errors in the atmospheric temperature clear-sky case retrieval [Figure 5.13(b)]. The –2 K BTD in the channels between 1300 to 1600 cm^{-1}, which have high- to mid-levels moisture weighting function peaks, correspond to the upper-level moist layer (~200 hPa) or the cloud (~550 hPa) altitudes mentioned previously.

5.5 Summary

Synergistic use of AIRS and MODIS measurements, including the MODIS cloud products improve atmospheric profile estimation. Using MODIS cloud mask to derive the AIRS SFOV cloud fraction and the collocated MODIS clear pixel radiance measurements as additional predictors based on an eigenvector regression to retrieve the atmospheric state and surface parameters, the synergistic AIRS and MODIS method improves in the comparison with either AIRS or MODIS stand-alone method, especially in atmospheric boundary layer.

The synergistic retrieval method is developed using sets of regression coefficients from a dataset containing more than 15000 atmospheric profiles. The retrieval products include temperature, humidity, and ozone from 0.005 hPa to either the surface in clear skies and cloudy skies with broken clouds, or to the cloud-top level when optically thick clouds are present. Comparison with a co-located radiosonde measurement at the SGP CART site is used for validation of the sounding products. The accuracy and capability of the synergistic algorithm by comparisons of the retrievals and in-situ observations is promising. In addition, clear-sky spectra BT calculations using synergistic method retrievals have lower BT differences when compared with the adjacent clear neighbor AIRS BT measurements, and this suggests the retrievals are stable for synergistic scheme.

Simulations shows that (1) optimally choosing the used eigenvectors could reduce the dimension of the regression problem, eliminate the impact due to random noise, and conduct the best estimation of the retrieved parameters [Figures 5.4 and 5.5]; (2) the RMSE of cloudy high spectral resolution retrievals could be improved to the accuracy of the clear-sky retrievals when the method incorporates high spatial resolution imager data (Figure 5.8). These enhancements are demonstrated through the comparison between the retrieved profiles and model analysis fields as well as preliminary validation with co-located radiosonde observations (RAOB) in Chapter 5.4. The UT levels in general have higher retrieval accuracy than in the atmospheric boundary layer [Figures 5.8 and 5.9]. It may provide an opportunity that the information embedded in the upper troposphere, in particular during the pre-storm stage, could be revealed using the atmospheric profiles from high spectral resolution measurements.

Chapter 6 Application to Short Term Severe Storms

This chapter presents the utilization of retrieved profile information to study the state of the upper troposphere (UT). The first section discusses the advantage of using high spectral resolution infrared measurements to analyze upper tropospheric phenomena. Such advantages include how the fine vertical resolution and high accuracy of the sounding profiles can be used to derive the stability of the UT, in particular, of the pre-storm stage. Clouds that penetrate the tropopause have characteristic spectral signatures which require high spectral resolution observation to detect; the detection scheme is given in the second section. The third section concludes with a discussion on the associated rainfall rate estimation and tropopause penetrating convection (TPC).

6.1 Upper Tropospheric Stability in the Pre-storm Stage

Inferring the high vertical resolution atmospheric profiles is the first step for estimating the state of the UT. Details on high vertical resolution atmospheric profiling algorithms are given in Chapter 5. In this study, the retrieved profiles obtained from the synergistic retrieval algorithm [Chapter 5.3] are used to explore the relationship between the state of the UT and mesoscale weather. The derived buoyancy frequency squared (Brunt–Väisälä frequency squared; N^2) from the retrieved profile and accumulation of hourly rainfall rate will be used as proxy variables for the state of the UT and mesoscale convective storms, respectively.

The buoyancy frequency squared (N^2) of the atmosphere at given geometric height z may therefore be expressed as

$$N^2(z) = \frac{g}{\theta_z}\left(\frac{\partial \theta_z}{\partial z}\right) \quad , \tag{6.1}$$

where θ_z is potential temperature at z, and g is the local acceleration of gravity. Equation (6.1) may be further derived at pressure level in the form of

$$N^2(p) = -\frac{g}{\theta_p}\frac{p^\kappa}{T_p}\frac{\kappa g}{R}\left(\frac{\partial \theta_p}{\partial p^\kappa}\right) \quad , \tag{6.2}$$

where κ is the ratio of the gas constant of air (R) and the specific heat capacity at a constant pressure (c_p), T is the air temperature, and subscript p stands for the given physical quantity at pressure level p. By rearrangement of Equation (6.2), the estimation of N^2 at pressure coordinates directly from the retrieved profile while avoiding the complication of the introduction of uncertain air density ρ.

A case study is used to study the relationship of the state of the UT to a historical rainfall/flooding event: the rainfall and flooding of historical proportions that struck parts of the upper Mississippi River valley on 18th August, continuing through 19th August, 2007. Rainfall in excess of 250 to 300 mm (10 to 12 inches) fell in some areas with the main swath of heaviest rain centered along a line from Claremont and Rochester in Minnesota, to La Crosse, Viroqua, and Muscoda in Wisconsin. The synoptic weather was due to a warm front extended across northern Iowa and central Illinois on 18th August, continued to sit there through 20th August, 2007. From this, a very moist and warm air mass rose up and over this area, providing the fuel

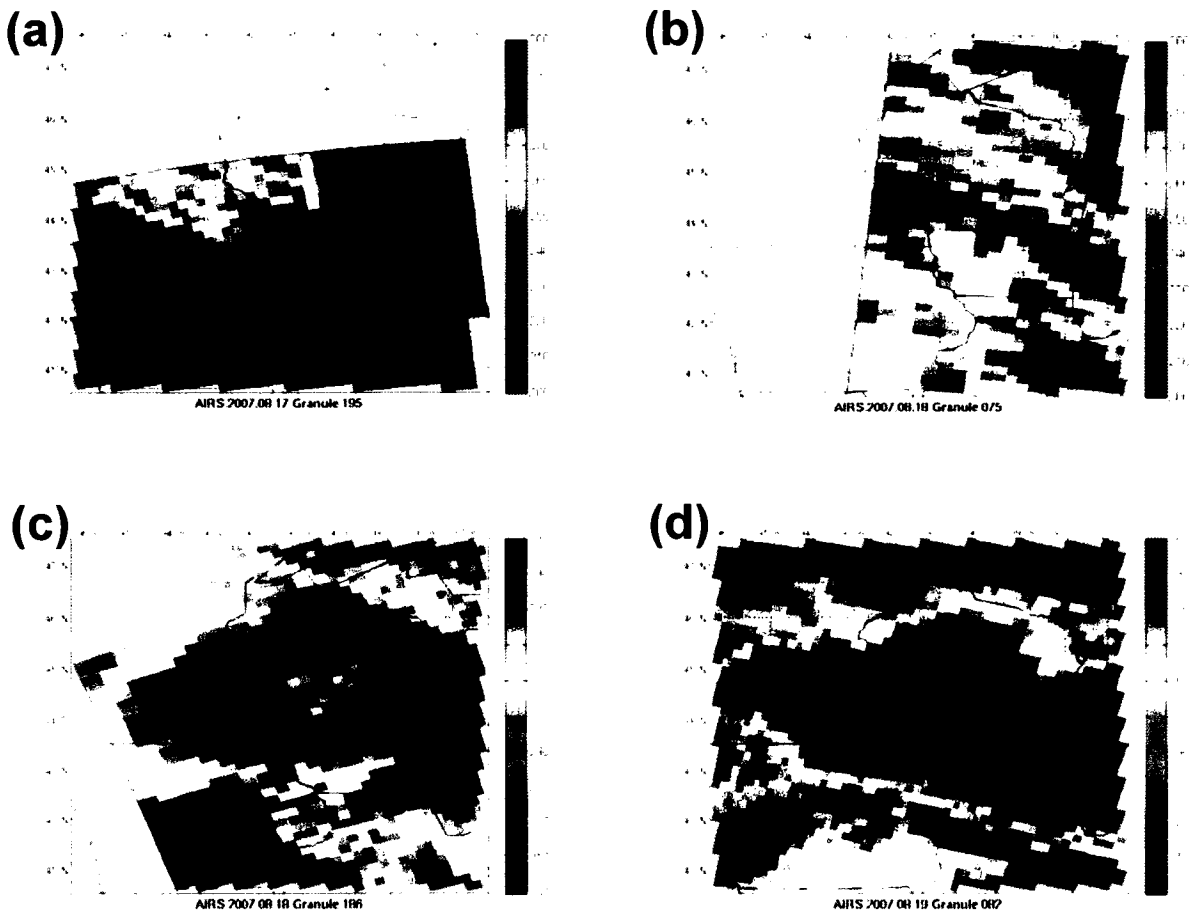

Figure 6.1 The AIRS longwave window channel brightness temperature images at wavenumber 911 cm^{-1} for (a) granule 195 (daytime) 17th August, 2007, (b) granule 075 (nighttime) 18th August, 2007, (c) granule 186 (daytime) 18th August, 2007, and (d) granule 082 (nighttime) 19th August, 2007. The dot in each panel is the location of La Crosse, Wisconsin.

for showers and thunderstorms. The depth of the warm layer as well as the considerable amount of moisture set the stage for heavy rainfall. Thus, the strong precipitation developed on 18th August, eventually orientating into a west-to-east moving line from the northern Plains through southern Minnesota, and then into southwest Wisconsin at midnight of the same day. However, this severe precipitation was not fully captured in NCEP 6-hr forecasts.

There were four of NASA's EOS *Aqua* overpasses in the historical rainfall and flooding region, and the AIRS and MODIS observations provide the detailed UT analysis at different stages of the event. Figure 6.1 shows the AIRS window channel BT images at 911 cm^{-1} on 17th August granule 195 (daytime), 18th August granule 075 (nighttime), 18th August granule 186

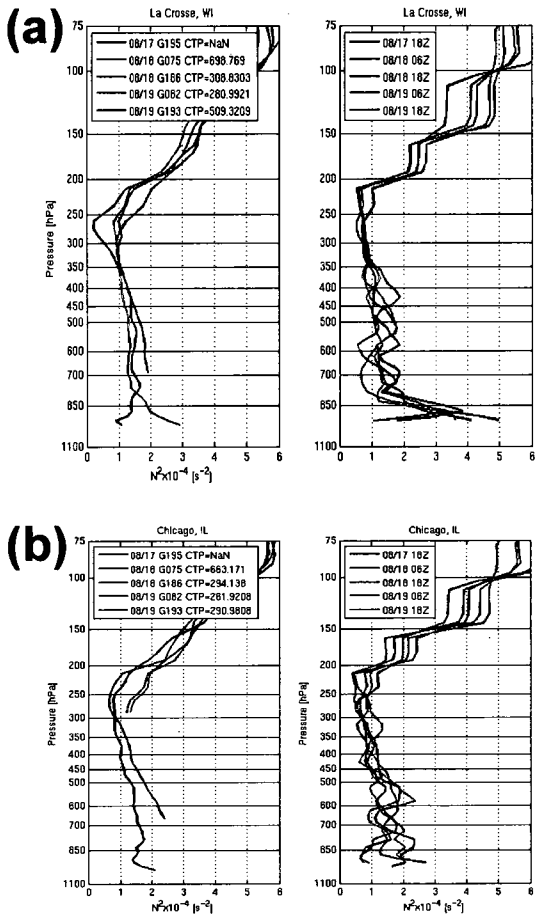

Figure 6.2 The vertical distribution of the buoyancy frequency squared (N^2) [s^{-2}] from AIRS retrieved products (left panels) and NCEP reanalysis field at different stages of the storm as indicated in the legend for (a) La Crosse, Wisconsin, and (b) Chicago, Illinois.

(daytime), and 19th August granule 082 (nighttime) as before the storm, pre-storm, storm developing, and storm mature stages, respectively. Since La Crosse, Wisconsin, is located at the center of the heavy rainfall, while Chicago, Illinois, is at the edge of the storm system, the states of the UT from the synergistic retrieval profiles and model forecasts over these two locations at different storm stages are selected for the comparisons as shown in Figure 6.2. An existing low stability layer (i.e., smaller N^2 values) in the upper troposphere (the layer between 250 and 300 hPa) at the pre-storm stage is found above La Crosse, but this is not identified in Chicago at different storm stages. Due to the relatively low vertical resolution above the atmospheric boundary layer of model forecasts, the analyzed N^2 in the right panels of Figure 6.2(a) and 6.2(b) are only for reference. It is assumed that the relative low UT stability may responsible for the enhancement of the precipitation.

The along-track transects of the retrieved and 6-hr model forecast temperature field at pre-storm stage are shown in Figure 6.3(a) and 6.3(d). The clear and cloudy soundings are comparable to the temperature field from the model forecast in UT altitude. However, the derived buoyancy frequency squared N^2 shows the different patterns in Figure 6.3(b) and 6.3(e). The model has a discrete distribution of N^2 due to coarser vertical resolution, while the N^2 value from the retrieved profiles has more detail distribution both vertically and horizontally. It is commonly accepted that N^2 varies from values $1.0\times10^{-4}\,s^{-2}$ (near the surface) to $2.0\times10^{-4}\,s^{-2}$ or more (at higher altitudes), with $N^2 \approx 1.44\times10^{-4}\,s^{-2}$ for average tropospheric conditions, and increases to values larger than $4\times10^{-4}\,s^{-2}$ in the stratosphere [*Peixoto and Oort*, 1992; *Holton*, 2004]. A lower value of N^2 corresponds to a lower stability, and vice versa. A layer of low

stability in the upper troposphere (~ 250 to 300 hPa) spanning from 41° N to 44° N may be responsible for accelerating the lifted moisture air parcels to a higher altitude, as well as resulting in more condensation and severer precipitation. From 43° N toward to 45° N, the levels with low stability have slant decreasing altitudes from 300 hPa to approximately 500 hPa. This is correlated with the frontal lifting mechanism. The above information is embedded

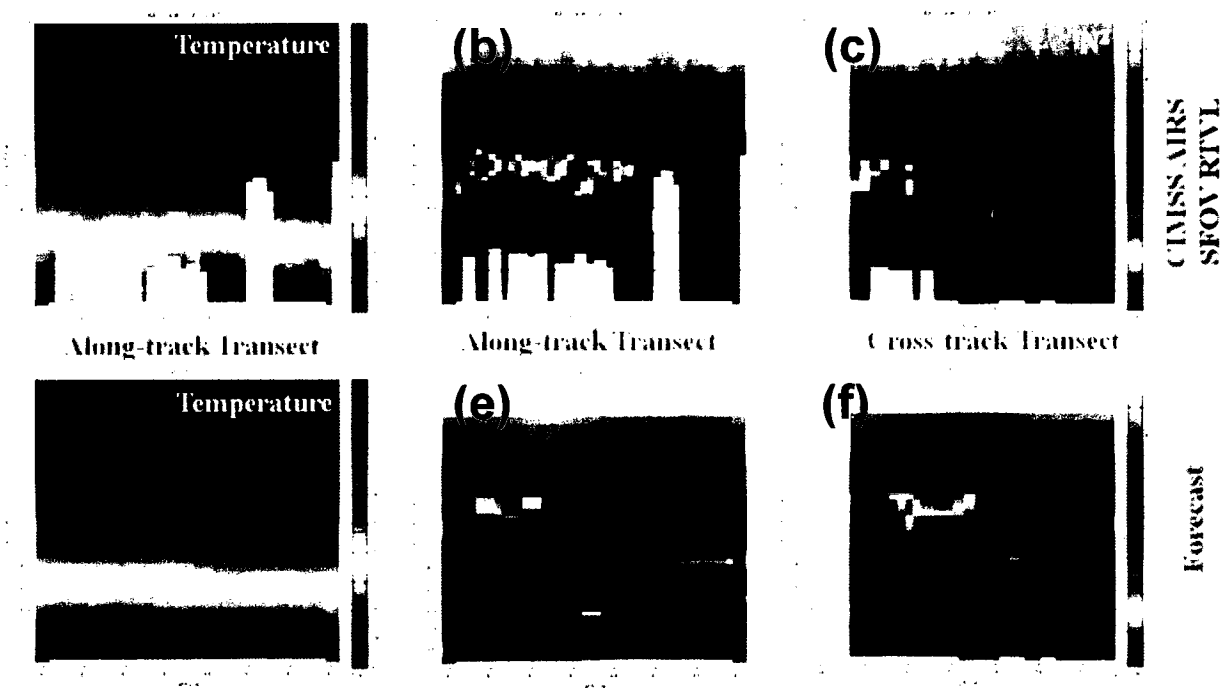

Figure 6.3 The alone-track vertical transects of (a) AIRS retrieved temperature [K], and (b) derived buoyancy frequency squared (N^2) [s^{-2}] from footprint 87 AIRS granule 075 (nighttime) 18th August, 2007. Panel (c) is the cross-track transect of N^2 from scan-line 76 same granule. The lower panels (d) through (f) are from NCEP 6-hr forecasts at AIRS footprints for the same analysis in (a) through (c). Note the N^2 in panels (b), (c), (d), and (f) is not in a linear scale as shown in the colorbar on the right.

within the retrieval products and may not be completely identified from the NWP model output. Similar signatures are also shown in the cross-track transects in Figure 6.3(c). The location of

La Crosse, Wisconsin, is around 43.8° N and 91.2° W, where the low UT stability in the pre-storm stage is identified in both Figure 6.3(b) and 6.3(c).

Further study of the relationship between the state of the UT and storm activities has been conducted. The hourly precipitation data from NCEP is accumulated for 12- and 6-hr separately, in correspondence with NASA's EOS *Aqua* satellite overpasses, as shown in Figure 6.4. The NCEP hourly precipitation dataset is a synergistic product from radar and rain gauge at approximately a 4 by 4 km grid spatial resolution over the contiguous United States (CONUS)

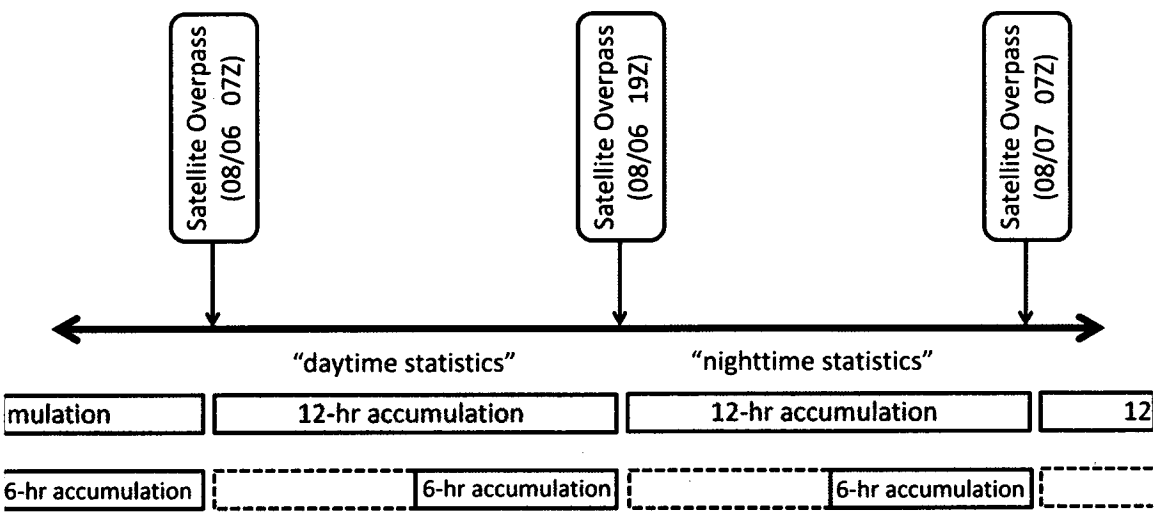

Figure 6.4 Sample 12- and 6-hr precipitation accumulation windows in between satellite overpasses. The daytime statistics are the accumulated NCEP hourly precipitation between 07UTC and 19UTC paired with the NASA EOS *Aqua* satellite 07 UTC descending overpass, and the nighttime statistics are the accumulated precipitation between 19 UTC and 07 UTC the following day paired with the 19 UTC satellite ascending overpass. The 6-hr accumulation window is similar to 12-hr window but does not include the accumulation during the first 6 hours of each 12-hr window.

[*Lin and Mitchell*, 2005]. The accumulated precipitation is used as a proxy variable for the mesoscale convective storms in this study. In general, *Aqua* satellite has descending 07 UTC and ascending 19 UTC overpasses across the central, as well as eastern part of CONUS, which is the region of highest storm frequency, as shown in Figure 6.7. The 12-hr accumulation of hourly precipitation is broken between the two overpasses as shown in Figure 6.4. The 6-hr accumulation is similar to 12-hr accumulation but only for the last 6-hr within the 12-hr window. To identify major convective storm clusters, a criteria was set for regions with 12-hr accumulation precipitation greater than 10-mm within a minimum of 50 grid boxes. These identified precipitation clusters were then paired with the derived stability parameter from Equation (6.2) using the retrieved profile information from hyperspectral resolution infrared soundings.

The N^2 is also examined at the UT level from synergistic retrieved products from combined AIRS and MODIS in both clear and cloudy skies at the AIRS single FOV spatial resolution, which is about 13.5 km at nadir view. Meanwhile, 12-hr accumulated hourly rainfall rate in the month of August 2009 over CONUS was performed to identify major convective storm clusters as well. Figure 6.5 is a scatterplot between 12-hr accumulated precipitation of identified mesoscale convective storms and the corresponding N^2 at UT 300-hPa level at the beginning of the 12-hr accumulation window. In terms of mesoscale convective storms, it is apparent from Figure 6.5 that a low stability UT is highly associated with accumulated precipitation of 30-mm and higher. The scatter pattern of the identical analysis for the 6-hr accumulation in Figure 6.6 is similar to Figure 6.5, except with a generally larger precipitation accumulation in the 12-hr statistics. This suggests not only that these storms have the largest

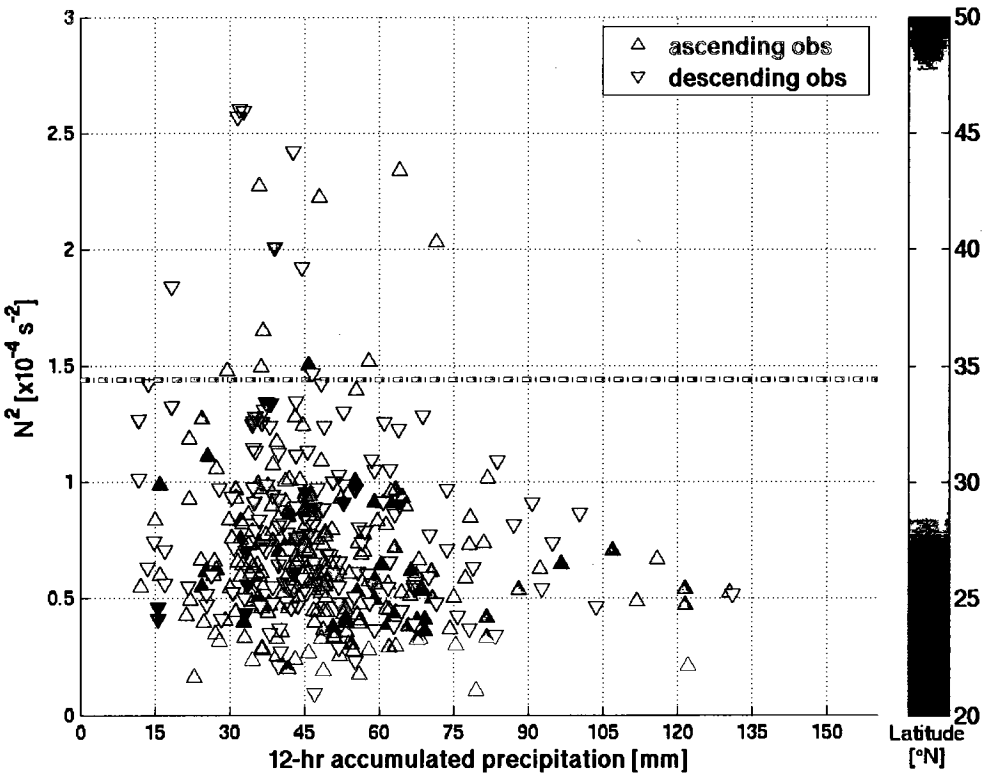

Figure 6.5 Scatterplot between 300-hPa buoyancy frequency squared N^2 [s^{-2}] from AIRS retrieved profile and NCEP 12-hr accumulated precipitation [mm] (471 identified mesoscale convective clusters in the month of August 2009). Latitudes are shown in the color scale, and satellite ascending, descending observations are labeled with different symbols, as seen in the legend. Green dashed line is the average tropospheric conditions N^2 for comparison.

precipitation intensity in the last half of the 12-hr window, but also the UT low stability state is favorable for either the development or maintenance of some convective storms. The limited convective cases associated with a stable UT, i.e., dots with higher values of N^2 than the reference 1.44×10^{-4} s^{-2} in Figures 6.5 and 6.6, tend to occur in the more northern latitudes of the region (represented as warm colors in the scatter diagram). This suggests the need to include

other mechanisms for heavy precipitation diagnosis in the analysis, such as atmospheric baroclinity, which is common in the extratropics.

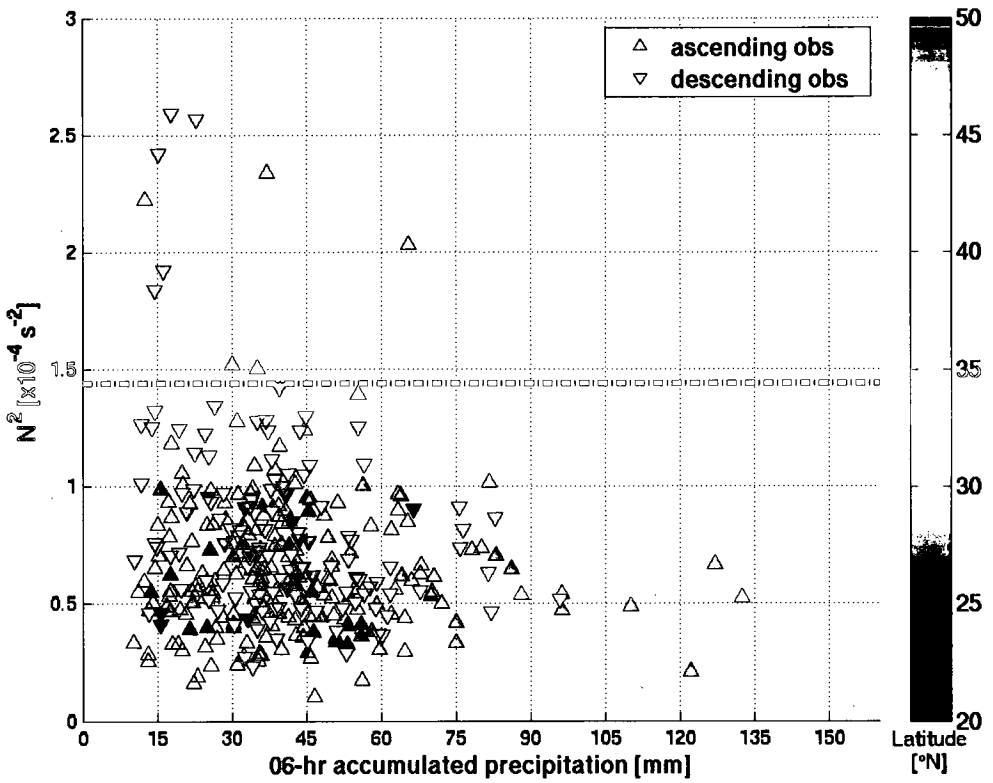

Figure 6.6 Same as Figure 6.5 but for 6-hr accumulation precipitation from 6 hours after satellite overpass.

The central geographical locations and the spatial size of identified convective clusters are shown in Figure 6.7. The distribution is widely spread between latitudes of 25° and 50°N, with a concentration in the Midwest and Eastern CONUS. Little or no identified clusters appear in

the Rocky Mountains and west coast, since few convective systems met our size and accumulated precipitation criteria in these regions. The spatial distribution of these storms is similar to *Velasco and Fritsch* [1987] in Figure 6.8. From the cross-comparisons between the UT stability with 12-hr precipitation accumulation and storm sizes in Table 6.1, there is a correlation that a lower stability of the UT is related to larger size and stronger mesoscale storms, while this relationship is not significant in a synoptic scale precipitation pattern. This yields the pronounced UT stability on mesoscale convection cluster study.

Table 6.1 Averaged buoyancy frequency squared N^2 [$\times 10^{-4} s^{-2}$] of identified storms in Figure 6.7 at 300-hPa level versus 12-hr precipitation accumulation (R) and storm pixel number (n) classifications. For storms with $n \geq 800$ are considered as synoptic scale in this study and shaded in the most right column. Daytime statistics are in the parentheses.

12-hr precipitation accumulation (R) [mm]	Storm pixel number (n)			
	$n < 150$	$150 \leq n < 400$	$400 \leq n < 800$	$n \geq 800$
$R < 30$	0.7497 (0.7208)	0.6746 (0.5997)	0.5969 (-)	[illegible]
$30 \leq R < 60$	0.5234 (0.6847)	0.6620 (0.6608)	0.6403 (0.6540)	[illegible]
$R \geq 60$	- (-)	0.6469 (0.6172)	0.5461 (0.5745)	[illegible]

Further comparisons between the locations of storm clusters and their ambient environment UT stability at same 300-hPa level have been conducted and are shown in Figure 6.9. Since the majority of scatter dots fall within the lower right panel, it is revealed that a lower stability over the storm cluster location than the storm ambient environment in the UT level frequently occurs. This indicates a pre-existing low UT stability may be favorable for storm development approximately 6- to12-hrs later. This is supported by Figure 6.9 with Figures 6.5, 6.6.

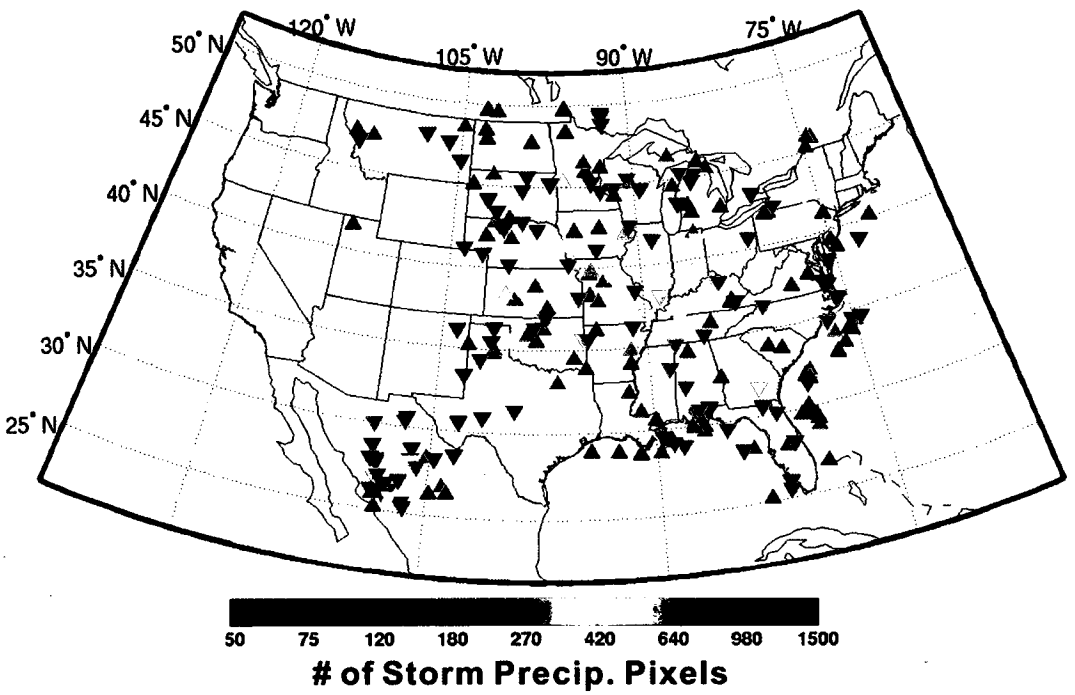

Figure 6.7 The central geographic locations of those identified mesoscale convective clusters. The numbers of storm precipitation pixels in the accumulation dataset in the month of August 2009 are shown in color scale. Corresponding satellite ascending, descending observations are labeled in the same manner as Figure 6.5.

Although AIRS offers new insight into the atmospheric stability of the UT and storms, there is a limitation to the study that warrants mention. The approximate 1:30 AM/PM equatorial crossing time of the EOS *Aqua* satellite indicates that important phases of the diurnal cycle of the mesoscale convection are not sampled. Different stages of convection experience various diurnal phases [*Machado et al.*, 1998], and this is more significant over land than over ocean since continental deep convection has a pronounced peak during late afternoon [*Soden*, 2000; *Liu and Zipser*, 2005; *Luo et al.*, 2008]. Therefore, the statistics of the storm pixel

numbers classified in Table 6.1 should be considered tentative and is expected to be altered when sampling a whole stage of mesoscale convection systems (e.g., *Li et al.* [2009]).

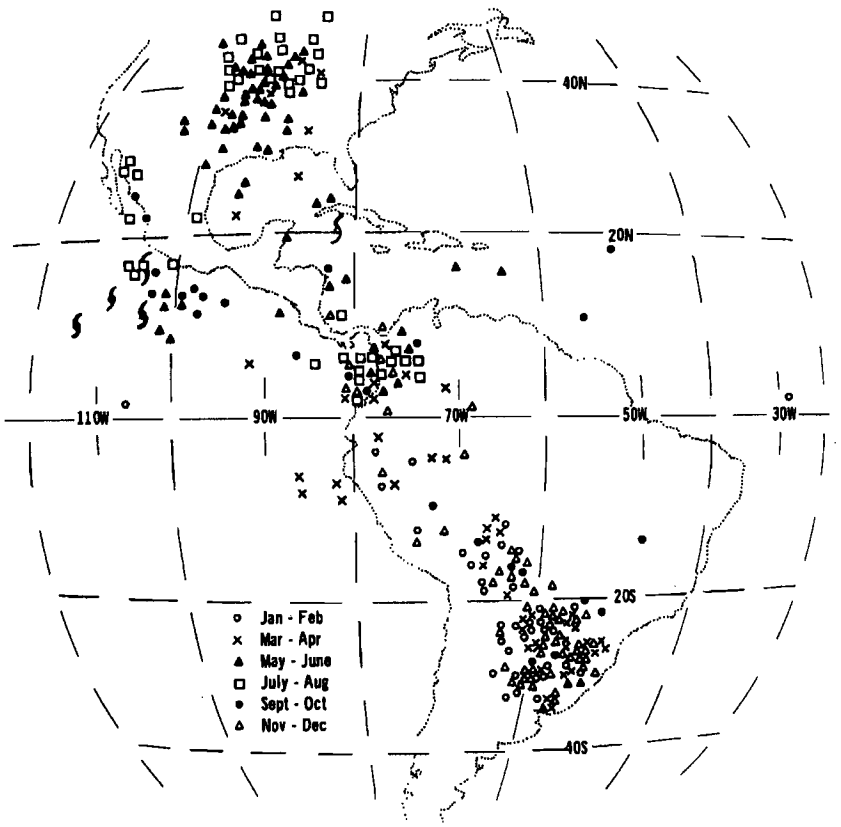

Figure 6.8 Geographic and monthly distribution of mesoscale convective complexes (MCCs) in and around the Americas. Locations are for the MCC cold-cloud shields at the time of maximum extend. Duration of MCCs over the United States, low-latitudes, and mid-latitude South America. U.S. sample is from 1978 and 1981; mid-latitude South American population is for the November-April periods of 1981-1982 and 1982-1983; low-latitude population is from May 1981 to April 1983. Hurricane symbols indicate an MCC that developed into a tropical storm (After *Velasco and Fritsch*, [1987]).

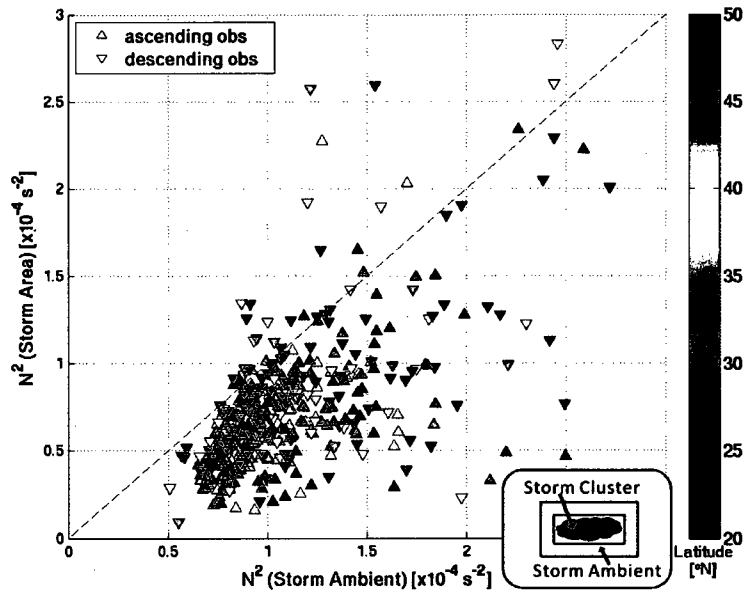

Figure 6.9 Comparison of storm area with storm ambient buoyancy frequency squared N^2 [s^{-2}] at 300-hPa level. The black dashed line shows a 1-to-1 correspondence between storm cluster and ambient N^2. Note that the storm ambient is defined as 3° outward from the identified storm cluster border as the sketch diagram shown in the insert.

Although this sub-sampling could be somewhat improved with additional sensors, such as IASI, a hyperspectral resolution infrared sounder in a geostationary orbit, hourly UT state could be obtained and this limitation will be eliminated [Schmit *et al.*, 2009].

Many past studies have focused on various atmospheric boundary layer convergence types or surface instabilities [e.g., *Wilson and Schreiber*, 1986; and several following articles] as we contribute their distinct work as "*known*" factors analysis. Limited research has been conducted for those initiated convective systems without "*known*" factors for many reasons, and the percentage of those initiated convective storms due to "*unknown*" factor(s), in particular nocturnal convection systems, is more than 43% in *Wilson and Schreiber* [1986]. One may

assume that the 12-hr windows after the satellite ascending and descending passes are represented by nighttime and daytime precipitation accumulation, respectively. Neither Figure 6.5 nor Figure 6.6 shows statistically significant differences between daytime and nighttime UT stability with respect to storm activities. The lack of a day/night difference suggests that low UT stability could be a storm initiation mechanism in storms without a well defined forcing in the boundary layer, especially in the absence of surface heating, distinct nighttime boundary convergence, and low instability near the surface.

6.2 The Detection of Troposphere Penetrating Convection (TPC)

Attempts to determine signatures of severe weather activity from satellite data have been under investigation for many years. *Riehl and Schleusner* [1962] first attempted to determine the appearance of well-defined cloud streets to indicate convective hailstorms. *Merritt and Smith* [1969] correlated the size of a convective storm's cirrus anvil with the severity of the convective activity. Since the launch of the SMS/GOES series of satellite, extremely cold cloud tops (11 μm BT < 210 K) were first seen in the earliest GOES data, and *Reynolds* [1980] identified that there is a correlation of the cloud tops colder than 210 K with extreme storms, including severe flooding and massive hail as the correlation shown in Figure 6.10. Troposphere penetrating convections (TPCs) have been identified as localized source of lower-stratosphere water vapor through cloud-resolving NWP modeling (e.g., *Wang* [2003]; *Chemel et el.* [2008]), and weather satellite observation inferences [*Setvak et al.*, 2008], which have important implications for both monitoring the area with potential local natural hazards and earth's radiative balance and climate.

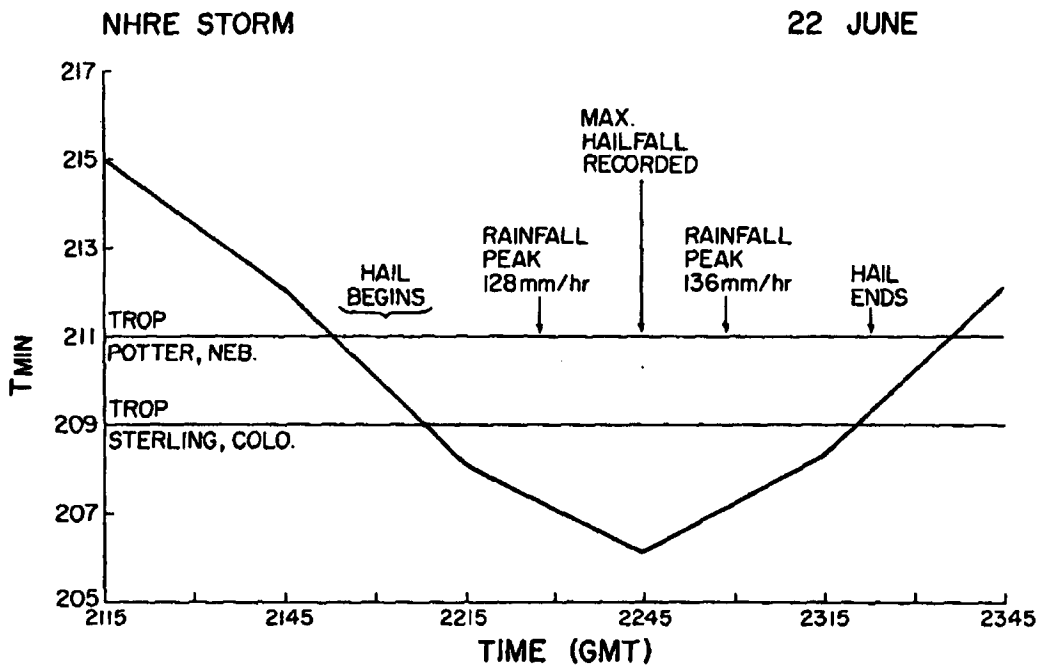

Figure 6.10 Time history of minimum cloud top temperature in relation to tropopause temperature for storm within the National Hail Research Experiment (NHRE; 1976) grid. Times of major weather events are noted (After *Reynolds* [1980]).

Fritz and Laszlo [1993] simulated that for cold cloud tops with a higher BT in water vapor band than the IR window band by High Resolution Infrared Sounder (HIRS) as the result of stratospheric emission against a cold background of a thick cloud. *Ackerman et al.* [1996] identified that occurrences of negative differences (i.e., $(BT_{11\mu m} - BT_{6.7\mu m}) < 0$) correlate highly with expected regions of convection within 50 degrees of the equator using the observation from HIRS/2 during January 1994 and July 1993. Similarly, *Schmetz et al.* [1997] monitored deep convection and convective overshooting with IR window (10.5 – 12.5 μm) and the water vapor absorption band (5.7 – 7.1 μm) from METEOSAT, and revealed that the brightness temperature

in the water vapor channel can be larger than the IR channel by as much as 6 – 8 K. Meanwhile, *Martin et al.* [2008] suggested a BT difference (BTD) less than –1 K is related to the presence of overshooting in 4-km GOES-12 imagery. Based on the MODIS 1-km imagery study by *Bedka et al.* [2010], the BTD method would detect a substantial portion of the anvil in addition to overshooting pixels, resulting in a larger number if false alarms. A BTD value of –2 K is shown to be a better threshold for using this high spatial resolution imagery.

In the study by *Aumann and Gregorich* [2006], large thunderstorms can be identified in the AIRS data as areas where the brightness temperature of the 1231 cm^{-1} (BT_{1231}; ~8.12 μm) atmospheric window channel in non-polar areas is less than 210 K. The study also points out that about 6000 large thunderstorms are identified by this test each day, almost exclusively within 30 degrees of the equator. Since the size of the AIRS footprint at nadir is 13.5 km, a brightness temperature of less than 210 K indicates that the top of the anvil of the thunderstorm protrudes well into the tropopause if a reversal in weak water lines near 1600 cm^{-1} (~6.25 μm) [*Aumann et al.*, 2009]. This signature requires high resolution observation for identifying the convection that penetrates the tropopause from high thick clouds.

In this study, the chosen channel to distinguish the tropopause penetrating convection (TPC) from thunderstorm anvils is the strong water vapor line at 1419 cm^{-1} (~7.05 μm). When presenting a brightness temperature reversal between this water vapor line and the atmospheric window at 1231 cm^{-1} (i.e., $BT_{1231} - BT_{1419} < 0$), the AIRS footprint is considered within the existence of TPC because the air parcel at the cold cloud top is brought to the lower stratosphere by an updraft overshooting, and the sensitivity of BT_{1419} is from the relatively warmer

stratosphere. Meanwhile, the averaged BT in the longwave window channels, which are eleven channels centered at 910 cm^{-1}, lower than 220 K threshold in the non-polar latitudes is applied as well. This test is similar to *Aumann et al.* [2009], while the TPC cloud tops are within 20 hPa of the cold point tropopause.

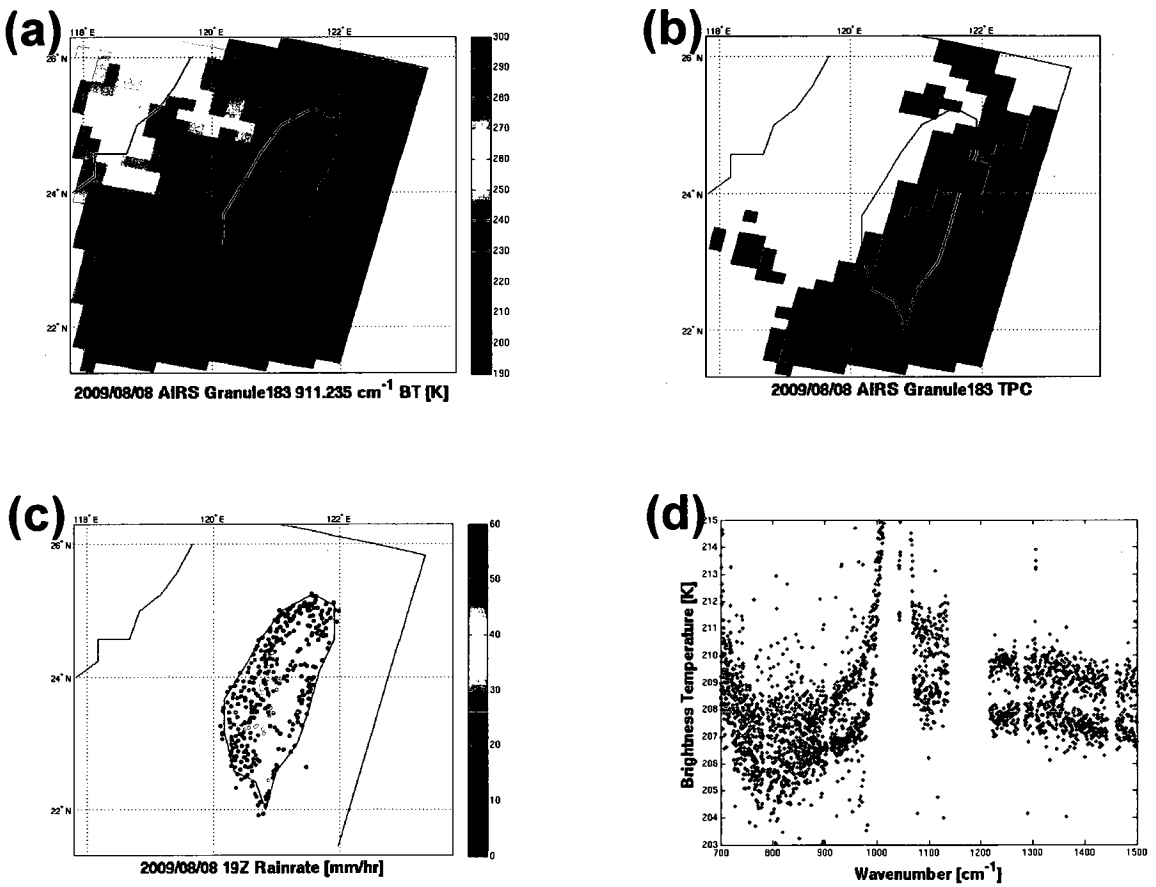

Figure 6.11 (a) The AIRS granule 183 longwave window channel brightness temperature images at wavenumber 911 cm^{-1} for Typhoon Morakot on 8th August, 2009. (b) The identified TPCs (red) and cold cloud tops (blue) within the same AIRS granule in (a). (c) The hourly precipitation for 19 UTC on 8th August, 2009. (d) Two sample brightness temperature spectra for TPC (red) and its adjacent cold cloud pixel (black).

A case shows that cluster of TPCs are highly associated with heavy rainfall. Figure 6.11(a) shows the 911cm^{-1} AIRS granule 183 window channel BT image of Typhoon Morakot on 8th August 2009, while Figure 6.11(b) indicates the TPC and cold cloud tops from the detection test in red and blue regions, respectively. Figure 6.11(c) is the image of 19 UTC hourly rainfall rate, which corresponds to the AIRS observation time. It is apparent that the major precipitation is in southern Taiwan where the TPC area is collocated in Figure 6.11(b). Two spectra from the adjacent AIRS observations with identified TPC and cold cloud top are shown in red and black respectively in Figure 6.11(d). Although the cold cloud top spectra has a lower longwave window channel BTs, the TPC spectra does represent high potential of strong conviction.

6.3 The Rainfall Rate Estimation of the TPC

Estimation of convective rainfall from visible and window infrared satellite data has been studied to support a variety of applications. These include climatology, hydrology, flash flood identification, input to agricultural models, verification of NWP, and the study of convective systems (e.g., *Griffith et al.* [1978, 1981]; *Scofield and Oliver*, [1977]; *Stout et al.* [1979]; *Arkin* [1979]; *Reynolds and Smith* [1979]; *Wylie and Laitsch* [1983]). *Wylie* [1979] used precipitable water differences and one-dimensional cloud model output differences to partially account for the variation in cloud-rain relationships between a tropical and a mid-latitude region. *Griffith et al.* [1981] used a rain parameter calculated from a one-dimensional cloud model to adjust rain estimates in the United States High Plains made with empirical relations derived in Florida, while *Adler and Nergi* [1988] proposed a technique by using GOES IR imager (10.5 –

12.6 μm) to distinguish between mesoscale convective and stratiform cloud systems as Convective-Stratiform-Technique (CST) during four days of the second Florida Area Cumulus Experiment (FACE), and had a general agreement with radar and rain gauge observed rainfall. *Goldenberg et al.* [1990] adopted CST and obtained the rainfall rate (RR) in associate convective cloud systems in Winter Monsoon Experiment (WMONEX) (around South China Sea; 0° – 7° N, 108° – 115° E) as

$$\ln(RR) = a \cdot (TB_{11\mu m}) + b \quad , \tag{6.3}$$

with empirical constants $a = -0.0157$ and $b = 4.76$. *Li et al.* [1993] followed similar approach over East China (28° – 35°N, 105° – 120°E), and had the similar relationship in Equation (6.3) with the coefficients $a = -0.0257$ and $b = 7.068$.

Using high spectral resolution observations for testing whether the footprint is TPC has been given in Chapter 6.2. The TPC correlated rainfall rate estimation from the collocated high spectral sounder and high spatial imager observation has been performed in this section. The AIRS footprints with detected TPC are collocated both temporally and spatially with NCEP rainfall rate data in the month of August 2009 over CONUS. Figure 6.12 shows the scatterplot between the hourly rainfall rate in logarithm scale with respect to averaged AIRS window region BTs. The red line suggests the linear least square y-fit regression in the study and gives the coefficients $a = -1.0521$ and $b = 220.3520$. Both constants are deviated and are different from the results of either *Goldenberg et al.* [1990] or *Li et al.* [1993], which are shown as black solid and dashed lines in Figure 6.12. The result is somewhat an overestimate or underestimate of the rainfall rate if the observed AIRS window BT is too cold or warm, respectively. It should

be noted that only TPCs with latitudes between 25° N and 35° N are included in Figure 6.12 because 25° N is approximately the lower limit in the NCEP precipitation rate, while 30° N to 35° N are the latitudes used in the study by *Li et al.* [1993].

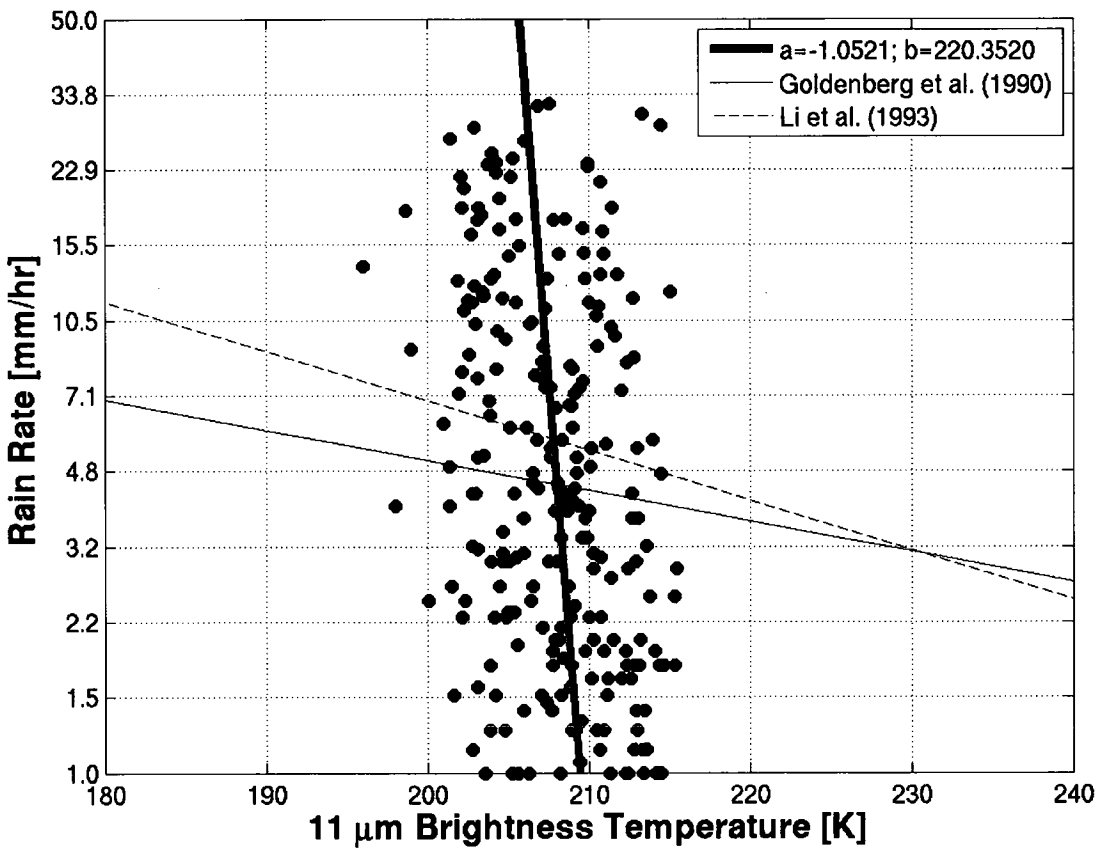

Figure 6.12 Scatter between the NCEP hourly rainfall rate [mm/hr] and AIRS averaged window BT [K] center at 910 cm^{-1} of identified TPC AIRS footprints in the month of August 2009. Only data points with latitudes lower than 35°N (but higher than approximately 25°N due to the lower boundary coverage in the precipitation data) are shown in the scatterplot. The red line is the least square regression fit line. The regression fit lines from *Goldenberg et al.* [1990] and *Li et al.* [1993] are overlaid for comparisons as black solid and black dashed lines, respectively.

Collocated MODIS infrared observations at 1-km spatial resolution (MYD02), in particular Band 31 (11 μm), within the identified AIRS TPCs are also studied following the same procedure as mention above. There are about 150 or more MODIS pixels within one collocated AIRS footprint as shown in Figure 4.3. Figure 6.13(a) is the scatterplot between the rainfall rates and the MODIS Band 31 BTs. It is supposed that the precipitation within the identified AIRS TPC footprint is not evenly distributed, and large precipitation pixels may be located at the core center of the storm cluster, while the edge or downstream of the TPC MODIS pixels may not be represented in the major rain area. For these reasons, those MODIS pixels with rainfall rate lower than 3 mm/hr are excluded in the statistics. Figure 6.13(b) shows the normalized frequency of the scatter data points occurrence in Figure 6.13(a). In general, when having a MODIS 11 μm BT greater than 215 K, the rainfall rate is about less than 4 mm/hr, however, when the BT is less than 210 K, the rainfall rate climbs up to 7 mm/hr. This is consistency with past studies by *Goldenberg et al.* [1990] and *Li et al.* [1993]. The linear least square y-fit regression using the 11 μm BT against the rainfall rate using Equation (6.3) gives the constants $a = -0.0337$ and $b = 8.9297$ as the red line shows in Figure 6.13(b). Both constants are close to their results as the black solid and dashed lines depicted in Figure 6.13(b), while the discrepancy may due to the imager data acquisition are on geostationary orbit with approximately 5-km spatial resolution. It should be mentioned that MODIS has warmer 11 μm BT than past studies at the same precipitation intensity. This is primarily because the minimum BT is chosen within the convection cluster for obtaining the relationship using Equation (6.3) in the past studies, while the MODIS rainfall rate estimation in this study is executed at each single pixel within the TPC cluster.

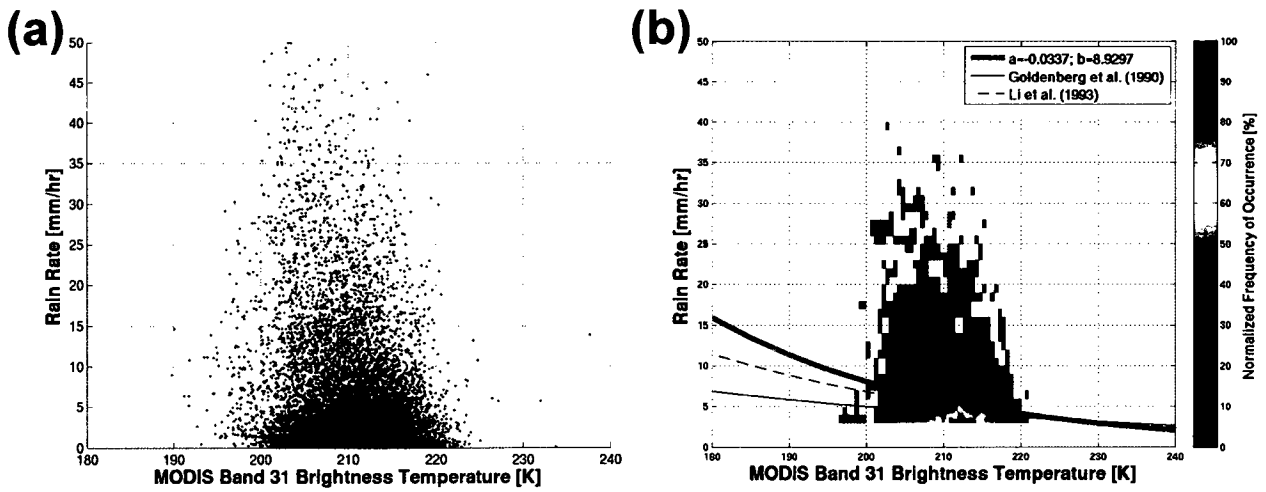

Figure 6.13 (a) Scatter between the hourly rainfall rate [mm/hr] and the collocated MODIS 1-km pixels 11 μm (Band 31) BT [K] within the identified TPC in Figure 6.12. (b) The normalized frequency of data points occurrence in 1 K and 1 mm/hr grid box in (a). The least square regression fit lines are overlaid, and the color and pattern are used as in Figure 6.12.

In summary, the utilization of the AIRS spectral signature can identify TPC through the BT difference between window and water vapor channels simultaneously. The TPC is commonly associated with flash floods and other natural hazards due to heavy precipitation. The estimated rainfall rate from AIRS footprints does show some limitation due to the large spatial resolution. Nevertheless, the collocated MODIS observations within those identified AIRS TPC footprints may give a possibility to estimate the rainfall rate more accurately than the estimation from AIRS BTs due to the high spatial resolution of MODIS IR measurements.

Chapter 7 Conclusions and Future Perspectives

The goal of this dissertation was to gain a better understanding of the upper troposphere by utilizing the high spectral resolution AIRS measurements. Handling high spectral resolution AIRS data is important because only less than 10% of AIRS footprints have being completed clear due to its relatively poor spatial resolution which is 13.5 km at nadir view. The new approach to remove the cloud effect was developed through optimally using the collocated MODIS Level-1B observation along with Level-2 product at 1-km spatial resolution. The optimal cloud-clearing algorithm on cloudy AIRS spectra can increase the clear-equivalence footprints, and the cloud-cleared radiances can be utilized in variety applications, such as direct clear-sky sounding and treat as clear radiances in the numerical weather simulations.

Case study shows the optimal cloud-clearing using multiple imager infrared bands has advantages over the traditional single-band N^* cloud-clearing approach. For example, the convolved AIRS cloud-cleared radiances have a 0.25 K low bias and 0.5 K small root-mean-squared difference (RMSD) when compared with collocated clear-sky MODIS infrared radiance observations. The case also demonstrated that more than 24% cloudy AIRS footprints were successfully cloud-cleared when applying the optimal cloud-clearing approach. The successful rate is greater than 40% of party cloudy footprints.

However, analyzing the state of upper troposphere under clear or clear-equivalence footprints may not represent the signature completely. Therefore, the clear and cloudy soundings were developed and enhanced in this dissertation as well. Both clear and cloudy high

spectral resolution infrared retrievals were based on a principle component regression scheme. The principle component number used in the retrievals has to be chosen optimally from both the reconstruct radiances and the retrieval performance. The simulations show using more than 40 but less than 100 principle components can substantially reduce the random noise in the reconstruct radiances. The retrieval performance has significant improvement when the leading 20 principle components were applied, and the improvement of accuracy is about saturated for over 60 principle components are used This concludes a retrieval scheme using 80 principle components in this dissertation.

The retrieval method is developed using a set of regression coefficients from a dataset containing more than 15000 atmospheric profiles. The retrieval products include temperature, moisture, and ozone from 0.005 hPa to either the surface in clear or optically thin clouds (i.e., COT < 1.5), or to cloud-top level when optically thick clouds are present. This AIRS alone retrieval scheme can be enhanced through the collocated MODIS clear-sky infrared observations along with the quadric terms as additional predicators. The synergistic use of AIRS and MODIS algorithm can improve AIRS cloudy-sky sounding to close the accuracy in AIRS clear-sky retrievals in the simulation. It shows higher accuracy in the UT levels than in the atmospheric boundary layer with the inter-comparison between the retrieved profiles and ECMWF model analysis fields as well as preliminary validation with co-located RAOB. This provides an opportunity to explore the goal of this dissertation.

One month of collocated AIRS and MODIS data along with hourly precipitation record were analyzed in an effort to add new insight into the understanding of the mesoscale convections. Emphasis was placed upon exploiting derived UT stability from high accuracy and

fine vertical resolution high spectral resolution infrared soundings, in conjunction with heavy precipitation (both with and without "*known*" initiation factors). The EOS *Aqua* satellite has descending 1:30 AM and ascending 1:30 PM local time equatorial crossing passes, which provides some capability to explore day/night differences, and thus the role of surface heating during daytime. The following upper tropospheric signatures of storms were observed: 1) The UT stability analysis indicated that a pre-existing low buoyancy frequency squared is a prominent feature in association with the initiated convective storms; 2) A relatively low stability over the storm locations compared to the ambient areas at UT level; 3) Stronger mesoscale storm activities, in terms of more intensive precipitation and greater coverage, was associated with lower UT stability. These signatures seem to lack a diurnal difference.

A considerable percentage of storms do not have well defined boundary convergence initiation mechanisms. This dissertation strives to explore the mesoscale storm with a top down perspective using enhanced synergistic atmospheric profiling algorithm from both AIRS and MODIS measurements. Even though the low UT stability correlates positively and significantly with mesoscale convective storms, the atmospheric boundary moisture plume provides the major source of precipitation. A very stable UT may limit and inhibit the growth of convective systems as studies have shown that large-scale descent can prevent convection even with the existence of large convective available potential energy (CAPE) and conditionally unstable environments [*Stensrud and Maddox*, 1988, *Richter and Bosart*, 2002]. Regardless of the storms initiation process, the presence of low UT stability could be favorable for rising parcels of air to reach the level of free convection (LFC), and responsible for organizing and intensifying storms.

For the convection with very strong updrafts, which the overshooting cloud tops may be higher than the tropopause, is detectable from high spectral resolution observation. These tropopause penetrating convections (TPCs) can be identified from the reversal of the brightness temperature between strong water vapor line at 1419 cm^{-1} and atmospheric window channel at 1231 cm^{-1} ($BT_{1231} - BT_{1419} < 0$) in the non-polar latitudes. Case study showed these TPCs were usually associated with heavy rainfall. The detection of TPC has the advantage of using high spectral resolution than the imager due to its spectral resolution, which the estimation of the rainfall rate using sounder has a limitation because of its spatial resolution. This TPC detection scheme using high spectral resolution sounder is very efficient compared to the detection using broadband imager which is a time-consuming process to distinguish convections from stratiform clouds. However, the estimated precipitation intensity using imager observations within the identified TPC footprints has a good agreement with past studies. This is also the advantage of synergistic use of multiple instruments.

Future research plans include additional validation of the retrievals, improvement for cases that contains mixed phase clouds, and a high spectral emissivity spectrum enhancement [*Li et al.*, 2007] using an iterative physical retrieval at AIRS SFOV resolution. The improvement of the retrievals due to the classification of surface and cloud properties, scan angles has to be quantified. The estimated precipitation intensity is subject to further validation using better dataset (e.g., 10-min precipitation, or finer gird with high reliability precipitation datasets). Several studies have applied the combination use of sounder and imager for cloud property retrieval [*Li et al.*, 2004, 2005a]. It may have the possibility for the detection of low stability in the upper troposphere from high spectral resolution infrared observations because the

spectra signature may be different from the stable UT. The long-term approach is to apply the methodology to other instrument like IASI, AVHRR onboard LEO satellite and also to support the development of synergistic algorithm for GEO ABI (Advanced Baseline Imager) [*Schmit et al.*, 2005] and LEO high-spectral IR sounders.

One may suggest that the utilization of space-borne microwave measurements and products for the state of upper troposphere study. Currently, there are very limited microwave sounder channels that have the weighting function in peaks in upper tropospheric levels. The results shown in this dissertation is based on AIRS spatial resolution, while A NASA's EOS *Aqua* AMSU observation covers about 3 by 3 AIRS footprints. The error will be introduced when remap AMSU data on AIRS spatial resolution. The utilization of microwave alone and synergistic use of infrared and microwave data should be studied in the future research.

One of the challenges of completing this dissertation was collecting, storing, and processing the AIRS granules. Currently, an AIRS Level-1B radiances data is about 60MB per granule. An AIRS granules usually needs up three MODIS granules for geolocation collocation process. A MODIS Level 1-B radiances (MYD02), Level-2 geolocation information (MYD03), and Level-2 cloud mask products (MYD35) are approximately 160 MB (daytime), 30 MB, and 3 MB per granule, respectively. There are more than 25 AIRS granules to cover CONUS per day. It takes about 2GB and 5GB computer storage per day for AIRS and MODIS data in this dissertation, respectively. If using the physical-based AIRS retrieval scheme, 4 to 8 hours processing time is needed for an AIRS granule. It will be a time-consuming process for conducting this study if the physical-based scheme was followed. Study shows significant difference for the upper troposphere N^2 analysis is not found when using physical-based

iteration scheme or the regression retrievals because the calculation of N^2 is based on the relative gradient for temperatures on two pressure levels. The future perspective should include the upper tropospheric N^2 analysis using profiles from physical-based retrievals, especially under cloudy footprints.

References

Ackerman, S. A. (1996), Global satellite observations of negative brightness temperature differences between 11 and 6.7 mm. *J. Atmos. Sci.*, **53**, 2803–2812.

Ackerman, S. A., K. I. Strabala, W. P. Menzel, R. A. Frey, C. C. Moeller, and L. E. Gumley (1998), Discriminating clear-sky from clouds with MODIS, *J. Geophys. Res.*, **103**, 32,141–32,157.

Ackerman, S. A., R. E. Holz, R. Frey, E. W. Eloranta, B. Maddux, and M. McGill (2008), Cloud detection with MODIS. Part II: Validation, *J. Atmos. Oceanic Technol.*, **25**, 1073– 1086.

Adler, R. F., and A. J. Negri (1988), A Satellite Infrared Technique to Estimate Tropical Convective and Stratiform Rainfall, *J. Appl. Meteor.*, **27**, 30-51.

Aoki, T. (1985), A method for matching the HIRS/2 and AVHRR pictures of TIROS-N satellites, paper presented at the *2nd International TOVS Study Conference,* Coop. Inst. for Meteorol. Satell. Study, Igls, Austria.

Arkin, P. A. (1979), The relationship between fractional coverage of high cloud and rainfall accumulations during GATE over B-scale array, *Mon. Wea. Rev.*, **107**, 1382-1387.

Aumann, H.H., M.T. Chahine, C. Gautier, M. Goldberg, E. Kalnay, L. McMillin, H. Revercomb, P.W. Rosenkranz, W. L. Smith, D. H. Staelin, L. Strow and J. Susskind (2003), AIRS/AMSU/HSB on the Aqua Mission: Design, Science Objectives, Data Products and Processing Systems, *IEEE Transactions on Geoscience and Remote Sensing*, Vol.41.2. pp.253-264

Aumann, H. H., and D. Gregorich (2006), AIRS observations of deep convective clouds, *Proc. SPIE*, 6301, 63010J, doi: 10.1117/12.681201.

Aumann, H. H., A. Ruzmaikin, and Sergio M. DeSouza-Machado (2009), Clusters of Tropopause Penetrating Convective Systems and the Correlation with Hurricanes and Typhoons, submitted to *J. Climate*.

Barnes, G. (2001), Severe Local Storms in the Tropics, *Severe Convective Storms*, C. A. Doswell III, Ed., American Meteorological Society, Boston, MA, 359 – 431.

Bedka, K., J. Brunner, R. Dworak, W. Feltz, J. Otkin, and T. Greenwald (2010), Objective Satellite-Based Detection of Overshooting Tops Using Infrared Window Channel Brightness Temperature Gradients. *J. Appl. Meteor. Climatol.*, **49**, 181–202.

Bikos, D. E., J. F. Weaver, and B. C. Motta, 2002: A satellite perspective of the 3 May 1999 Great Plains Tornado Outbreak within Oklahoma. *Wea. Forecasting*, **17**, 635–646.

Borbas, E., S. Seemann, H.-L. Huang, J. Li, and W. P. Menzel (2005), Global profile training database for satellite regression retrievals with estimates of skin temperature and emissivity, *14th International ATOVS Study Conference*, NASA, Beijing.

Bluestein, H. B., and K. W. Thomas (1984), Diagnostic of a jet streak in the vicinity of a severe weather outbreak in the Texas panhandle, *Mon. Wea. Rev.*, **112**, 2449-2520.

Byers, H. R., and R. R. Braham Jr. (1949), *The Thunderstorm*, U.S. Government Printing Office, 287pp.

Chahine, M. T., et al. (2006), AIRS: Improving weather forecasting and providing new data on greenhouse gases, *Bull. Am. Meteorol. Soc.*, **87**, 911– 926.

Chemel, C., M. R. Russo, J. A. Pyle, R. S. Sokhi, and C. Schiller (2008), Quantifying the imprint of a severe hector thunderstorm during ACTIVE/SCOUT-O3 onto the water content in the upper troposphere/lower stratosphere. *Mon. Wea. Rev.*, **137**, 2493–2514.

English, S. J., R. J. Renshaw, P. C. Dibben, A. J. Smith, P. J. Rayer, C. Poulsen, F. W. Saunders, and J. R. Eyre (2000), A comparison of the impact of TOVS and ATOVS satellite sounding data on the accuracy of numerical weather forecasts, *Quarterly Journal of the Royal Meteorological Society*, Berkshire, England, 126, 569, 2911-2931.

Fetzer, E. J., L. McMillin, D. Tobin, H. H. Aumann, M. R. Gunson, W. W. McMillan, D. E. Hagan, M. D. Hofstadter, J. Yoe, D. Whiteman, J. Barnes, R. Bennartz, V. Walden, M. Newchurch, P. Minnett, R. Atlas, F. Schmidlin, E. T. Olsen, M. Goldberg, S. Zhou, H. Ding, W. Smith, Sr., H Revercomb (2003), AIRS / AMSU / HSB Validation, *IEEE Transactions Geosci. and Remote Sensing*, **41**, 418-431.

Frey, R. A., S. A. Ackerman, Y. Liu, K. I. Strabala, H. Zhang, J. R. Key, and X. Wang (2008), Cloud detection with MODIS, part I: Improvements in the MODIS cloud mask for collection 5, J. *Atmos. Oceanic Technol.*, **25**, 1057–1072.

Fritz, S., and I. Laszlo, 1993: Detection of water vapor in the stratosphere over very high clouds in the tropics. *J. Geophys. Res.*, **98** (D12), 22 959–22 967.

Goldenberg, S. B., R. A. Houze, Jr., and D. D. Churchill (1990), Convective and Stratiform Components of a Winter Monsoon Cloud Cluster Determined from Geosynchronous Infrared Satellite Data, *J. of the Meteorological Soc. of Japan*, 68, 37–63

Goldberg, M. D., Y. Qu, L. M. McMillin, W Wolf, L. Zhou, and M. Divakarla (2003), AIRS Near-Real-Time Products and Algorithms in Support of Operational Numerical Weather Prediction, *IEEE Transactions on Geoscience and Remote Sensing*, **41**, 379-389

Griffith, C. G., W. L. Woodley, and P. G. Grube (1978), Rain Estimation from Geosynchronous Satellite Imagery—Visible and Infrared Studies, *Mon. Wea. Rev.*, **106**, 1153-1171.

Griffith, C. G., J. A. Augustine, and W. L. Woodley (1981), Satellite rain estimation in the U.S. High Plains, *J. Appl. Meteor.*, **20**, 53-66.

Hannon, S., L. L. Strow, and W. W. McMillan (1996), Atmospheric infrared fast transmittance models: A comparison of two approaches, *Proc. SPIE Int. Soc. Opt. Eng.*, **2830**, 94– 105.

Heymsfield, A. J., S. Matrosov, and B. A. Baum (2003), Ice water path–optical depth relationships for cirrus and precipitating cloud layers. *J. Appl. Meteor.*, **42**:1369–1390.

Holton, J. R. (2004), *An Introduction to Dynamic Meteorology*, Fourth Edition (The International Geophysics Series, Vol 88), Elsevier Academic Press, Burlington, MA, 529 pp.

Huang, H.-L., and P. Antonelli (2001), Application of principal component analysis to high-resolution infrared measurement compression and retrieval. *J. Appl. Meteor.*, **40**, 365–388.

Huang, H.-L., and W. L. Smith (2004), Apperception of clouds in AIRS data, paper presented at the *ECMWF Workshop on Assimilation of High Spectral Resolution Sounders in NWP*, Reading, U. K. 28 June– 1 July.

Huang, H.-L., L. E. Gumley, K. Strabala, J. Li, E. Weisz, T. Rink, K. C. Baggett, J. E. Davies, W. L. Smith, and J. C. Dodge (2004), International MODIS and AIRS Processing Package (IMAPP): a direct broadcast software for the NASA earth observing system, *Bull. Amer. Meteor. Soc.*, **85**, 159-161

Johnson, R. H., and B. E. Mapes (2001), Mesoscale Processes and Severe Convective Weather, *Severe Convective Storms*, C. A. Doswell III, Ed., American Meteorological Society, Boston, MA, 71– 122.

King, M. D., Coauthors (2003), Cloud and aerosol properties, precipitable water, and profiles of temperature and water vapor from MODIS. *IEEE Trans. Geosci. Remote Sens.*, **41**:442–458.

Li, J., L. Y. Wang, and F. X. Zhou (1993), Convective and stratiform rainfall estimation from geostationary satellite data. Advances *in Atmospheric Sciences*, **10**, 475 - 480.

Li, J. and H.-L. Huang (1999), Retrieval of atmospheric profiles from satellite sounder measurements by use of the discrepancy principle, *Appl. Opt.*, **38**, 916-923.

Li, J., W. Wolf, W. P. Menzel, W. Zhang, and T. Achtor (2000), Global sounding of the atmosphere from ATOVS measurements: The Algorithm and validation, *J. Appl. Meteorol.*, **39**, 1248-1268.

Li, J., W. P. Menzel, F. Sun, T. J. Schmit, and J. Gurka (2004), AIRS subpixel cloud characterization using MODIS cloud products, *J. Appl. Meteorol.*, **43**, 1083– 1094.

Li, J., C.-Y. Liu, H.-L. Huang, T. J. Schmit, X. Wu, W. P. Menzel, and J. J. Gurka (2005a), Optimal cloud-clearing for AIRS radiances using MODIS, *IEEE Trans. Geosci. Remote Sens.*, **43**, 1266– 1278.

Li, J., H.-L. Huang, C.-Y. Liu, P. Yang, T. J. Schmit, H. Wei, E. Weisz, L. Guan, and W. P. Menzel (2005b), Retrieval of cloud microphysical properties from MODIS and AIRS, *J. Appl. Meteorol.*, **44**, 1526– 1543.

Li, J., J. Li, E. Weisz, and D. K. Zhou (2007), Physical retrieval of surface emissivity spectrum from hyperspectral infrared radiances, *Geophys. Res. Lett.*, **34**, L16812, doi:10.1029/2007GL030543.

Li, Z., J. Li, W. P. Menzel, J. P. Nelson III, T. J. Schmit, E. Weisz, and S. A. Ackerman (2009), Forecasting and nowcasting improvement in cloudy regions with high temporal GOES sounder infrared radiance measurements, *J. Geophys. Res.*, **114**, D09216, doi:10.1029/2008JD010596.

Lin, Y., and K. E. Mitchell (2005), The NCEP Stage II/IV hourly precipitation analyses: development and applications, paper presented at the *19th Conference on Hydrology*, San Diego, CA 9-13 January 2005, American Meteorological Society, and data available online at http://data.eol.ucar.edu/codiac/dss/id=21.093

Liu, C., and E. J. Zipser (2005), Global distribution of convection penetrating the tropical tropopause, *J. Geophys. Res.*, **110**, D23104, doi:10.1029/2005JD006063.

Liu, C.-Y., J. Li, E. Weisz, T. J. Schmit, S. A. Ackerman, and H.-L.Huang (2008), Synergistic use of AIRS and MODIS radiance measurements for atmospheric profiling, *Geophys. Res. Lett.*, **35**, L21802, doi:10.1029/2008GL035859.

Liu, Yinghui; Key, Jeffrey R.; Frey, Richard A.; Ackerman, Steven A. and Menzel, W. Paul. Nighttime polar cloud detection with MODIS. *Remote Sensing of Environment*, **92**, 2004, 181-194.

Luo, Z., G. Y. Liu, and G. L. Stephens (2008), CloudSat adding new insight into tropical penetrating convection, *Geophys. Res. Lett.*, **35**, L19819, doi:10.1029/2008GL035330.

Machado, L. A. T., W. B. Rossow, R. L. Guedes, and A. W. Walker (1998), Life cycle variations of mesoscale convective systems over the Americas, *Mon. Weather Rev.*, **126**, 1630– 1654.

Merritt, W. S., and W. P. Smith (1969), Satellite-observed characteristics of severe local storms, Preprints *Sixth Conference Severe Local Storms*, Chicago, American Meteorological Soc., 208-217.

Moller, A. R. (2001), Severe Local Storm Forecasting, *Severe Convective Storms*, C. A. Doswell III, Ed., American Meteorological Society, Boston, MA, 433– 480.

Nagel, F. W. (1998), The Association of Disparate Satellite Observation, *Second Symposium of Integrated Observing System*, Phoenix, AZ, The American Meteorological Society. Jan., 11–16 1998, pp. 49–52.

Pagano, T. and co-authors (2001), Operational Readiness for the Atmospheric Infrared Sounder (AIRS) on the Earth Observing System Aqua spacecraft, paper presented at the *SPIE 46th Annual Meeting*, San Diego, CA, and online at http://hdl.handle.net/2014/12879

Peixoto, J. P, and A. H. Oort (1992), *Physics of Climate*, American Institute of Physics, New York, 520pp.

Platnick, S., M. D. King, S. A. Ackerman, W. P. Menzel, B. A. Baum, and R. A. Frey (2003), The MODIS cloud products: Algorithms and examples from Terra. *IEEE Trans. Geosci. Remote Sens.*, **41**:459–473.

Purdom, J.F. (1976), Some Uses of High-Resolution GOES Imagery in the Mesoscale Forecasting of Convection and Its Behavior, *Mon. Weather Rev.*, **104**, 1474– 1483.

Purdom, J.F. (1982), Subjective Interpretation of Geostationary satellite Data for Nowcasting, *Nowcasting*, K. Browning, Ed., Academic Press, 149- 166.

Reynolds, D. W., and E. A. Smith (1979), Detailed analysis of composited digital radar and satellite data, *Bull. Amer. Metero. Soc.*, **60**, 1024-1307.

Reynolds, D. W. (1980), Observations of damaging hailstorms from geosynchronous satellite digital data. *Mon. Wea. Rev.*, **108**, 337–348.

Richter, H., and L.F. Bosart (2002), The Suppression of Deep Moist Convection near the Southern Great Plains Dryline. *Mon. Weather Rev.*, **130**, 1665– 1691.

Riebsame, W.E., H.F. Diaz, T. Moses, and M. Price (1986), The Social Burden of Weather and Climate Hazards. *Bull. Amer. Meteor. Soc.*, **67**, 1378– 1388.

Riehl, H., and R. A. Schleusner (1962), On identification of hail-bearing clouds from satellite photographs, *Atmos. Sci. Pap.* No. 27, Colorado State University, 7pp.

Rodgers, C. D. (2000), *Inverse Methods for Atmospheric Sounding: Theory and Practice*. World Scientific, Singapore, 238pp.

Schmetz, J., S. A. Tjemkes, M. Gube, and L. van de Berg (1997), Monitoring deep convection and convective overshooting with METEOSAT. *Adv. Space Res.*, **19**, 433–441.

Schmit, T. J., M. M. Gunshor, W. Paul Menzel, J. Gurka, J. Li, and S. Bachmeier (2005), Introducing the next-generation advanced baseline imager (ABI) on GOES-R, *Bull. Am. Meteorol. Soc.*, **86**, 1079–1096.

Schmit, T. J., Li, J., S. A. Ackerman, J. J. Gurka (2009), High spectral and high temporal resolution infrared measurements from geostationary orbit, *J. Atmospheric and Oceanic Technology*, **26**, 2273 - 2292.

Schreiber, W. E. (1986), Case studies of thunderstorms initiated by radar-observed convergence lines, *Mon. Wea. Rev.*, **114**, 2256-2266.

Scofield, R. A., and V. J. Oliver (1977), A Scheme for estimating convective rainfall from satellite imagery, *NOAA Tech. Memo.* NESS 86, 47pp.

Seemann, S. W., J. Li, W. P. Menzel, and L. E. Gumley (2003), Operational retrieval of atmospheric temperature, moisture, and ozone from MODIS infrared radiances, *J. Appl. Meteorol.*, **42**, 1072–1091.

Setvak, M., D.T.Lindsey, R. M. Rabin, P. K. Wang, and A. Demeterova (2008), Indication of water vapor transport into the lower stratosphere above midlatitude convective storms: Meteosat Second Generation satellite observations and radiative transfer model simulations. *Atmos. Res.*, **89**, 170–180.

Smith, W. L., and H. M. Woolf, 1976: The use of eigenvectors of statistical covariance matrices for interpreting satellite sounding radiometer observations. *J. Atmos. Sci.*, **33**, 1127–1140.

Smith, W. L., H. M. Woolf, C. M. Hayden, D. C. Wark, and L. M. McMillin (1979), TIROS-N operational vertical sounder, *Bulletin of the American Meteorological Society*, **60**, 1177-1187.

Smith, W. L., D. K. Zhou, H.-L. Huang, J. Li, X. Liu, and A. M. Larar (2004), Extraction of profile information from cloud contaminated radiances, paper presented at the *ECMWF Workshop on Assimilation of High Spectral Resolution Sonder in NWP*, Reading, U. K., 28 June– 1 July 2004.

Smith,W. L., D. K. Zhou, H.-L. Huang, H. E. Revercomb, A. M. Larar, and C. Barnett (2005), Ultra high spectral satellite remote sounding—Results from aircraft and satellite measurements, paper presented at the *14th International TOVS Study Conference*, NASA, Beijing.

Soden, B. J. (2000), The diurnal cycle of convection, clouds, and water vapor in the tropical upper troposphere, *Geophys. Res. Lett.*, **27**, 2173– 2176.

Stensrud, D.J., and R.A. Maddox (1988), Opposing mesoscale circulations: A case study. *Wea. Forecasting*, **3**, 189- 204.

Strabala, K. I., S. A. Ackerman, and W. P. Menzel (1994), Cloud properties inferred from 8 –12 micron data, *J. Appl. Meteorol.*, **33**, 212– 222.

Strow, L. L., S. E. Hannon, S. De Souza-Machado, H. E. Motteler, and D. Tobin (2003), An overview of the AIRS radiative transfer model, *IEEE Trans. Geosci. Remote Sens.*, **41**, 303–313.

Stout, J. E., D. W. Martin, and D. N. Sikdar (1979), Estimating GATE rainfall with geosynchronous satellite image, *Mon Wea. Rev.*, **107**, 595-598.

Susskind, J., C. D. Barnet, and J. M. Blaisdell, (2003), Retrieval of atmospheric and surface parameters from AIRS/AMSU/HSB data in the presence of clouds, *IEEE Trans. Geosci. Remote Sensing*, **41**, 390–409

Szoke, E. J., M. L. Weisman, J. M. Brown, F. Caracena, and T. W. Schlatter (1984), A sub-synoptic analysis of the Denver tornado of 3 June 1981, *Mon. Wea. Rev.*, **112**, 790-808.

Tobin, D. C., et al. (2006a), Radiometric and spectral validation of Atmospheric Infrared Sounder observations with the aircraft-based Scanning High-Resolution Interferometer Sounder, *J. Geophys. Res.*, **111**, D09S02, doi:10.1029/2005JD006094.

Tobin, D. C., H. E. Revercomb, C. C. Moeller, and T. S. Pagano (2006b), Use of Atmospheric Infrared Sounder high–spectral resolution spectra to assess the calibration of Moderate resolution Imaging Spectroradiometer on EOS Aqua, *J. Geophys. Res.*, **111**, D09S05, doi:10.1029/2005JD006095.

Uccellini, L. W. and D. R. Johnson (1979), The coupling of upper- and lower-tropospheric jet streak and implications for the development of severe convective storms, *Mon. Wea. Rev.*, **107**, 682-703.

Velasco, I., and J. Fritsch (1987), Mesoscale Convective Complexes in the Americas, *J. Geophys. Res.*, **92**(D8), 9591-9613.

Wang, P. K. (2003), Moisture plumes above thunderstorm anvils and their contributions to cross-tropopause transport of water vapor in midlatitudes. *J. Geophys. Res.*, **108**, 4194, doi:10.1029/2002JD002581

Weaver,J. F. (1982), Subjective interpretation of geostationary satellite data for nowcasting. *Nowcasting*, K. A. Browning, Ed., Academic Press, 149–166.

Weaver, J. F. W. Purdom, and E. J. Szoke (1994), Some mesoscale aspects of the 6 June 1990 Limon, Colorado, tornado case. *Wea. Forecasting*, **9**, 45–61

Weaver, J. F. Dostalek, B. C. Motta, and J. F. W. Purdom (2000), Severe thunderstorms on 31 May 1996: A satellite training case. Natl. *Wea. Dig.*, **23**, 3–19.

Weaver, J. A. Knaff, D. E. Bikos, G. Wade, and J. M. Daniels (2002), Satellite observations of a severe supercell thunderstorm on 24 July 2000 made during the GOES-11 science test. *Wea. Forecasting*, **17**, 124–138.

Weaver, J.F., and D. Lindsey (2004), Some Frequently Overlooked Severe Thunderstorm Characteristics Observed on GOES Imagery: A Topic for Future Research. *Mon. Wea. Rev.*, **132**, 1529–1533.

Wei, H., P. Yang, J. Li, B. B. Baum, H.-L. Huang, S. Platnick, Y. Hu, and L. Strow (2004), Retrieval of semitransparent ice cloud optical thickness from Atmospheric Infrared Sounder (AIRS) measurements, *IEEE Trans. Geosci. Remote Sens.*, **42**, 2254– 2267.

Wilson, J. W., and R. Carbone (1984), Nowcasting with Doppler radar: The forecaster-computer relationship. *Nowcasting II*, K. Browning, Ed., European Space Agency, 177-186.

Wilson, J.W., and W.E. Schreiber (1986), Initiation of Convective Storms at Radar-Observed Boundary-Layer Convergence Lines, *Mon. Weather Rev.*, **114**, 2516– 2536.

Weisz, E., H.-L. Huang, J. Li, E. E. Borbas, K. Baggett, P. Thapliyal and G. Li (2007a), International MODIS/AIRS Processing Package: AIRS Applications and Products, *Journal of Applied Remote Sensing*, **1**, 1 – 23.

Weisz, E., J. Li, J. Li, D. K. Zhou, H.-L. Huang, M. D. Goldberg, and P. Yang (2007b), Cloudy sounding and cloud-top height retrieval from AIRS alone single field-of-view radiance measurements, *Geophys. Res. Lett.*, **34**, L12802, doi:10.1029/2007GL030219.

Weisz, E., J. Li, P. Menzel, A. Heidinger, B. H. Kahn, and C.-Y. Liu (2007c), Comparison of AIRS, MODIS, CloudSat and CALIPSO cloud top height retrievals, *Geophys. Res. Lett.*, **34**, L17811, doi:10.1029/2007GL030676.

Wylie, D. P. (1979), An application of a geostationary satellite rain estimation technique to an extratropical area, *J. Appl. Meteor.*, **18**, 1640-1648.

Wylie, D. P., and D. Laitsch (1983), The impacts of different satellite data on rain estimation schemes, *J. Climate Appl. Meteor*, **22**, 1270-1281.

Yang, P., K. N. Liou, K. Wyser, and D. Mitchell (2000), Parameterization of the scattering and absorption properties of individual ice crystals. *J. Geophys. Res.*, **105**:4699–4718.

Yang, P., B. A. Baum, A. J. Heymsfield, Y. X. Hu, H-L. Huang, S-C. Tsay, and S. Ackerman, (2003), Single-scattering properties of droxtals. J. *Quant. Spectrosc. Radiat. Transfer*, 79-80:1159–1180.

Zhou, D. K., W. L. Smith, X. Liu, A. M. Larar, S. A. Mango, and H.-L. Huang (2007), Physically retrieving cloud and thermodynamic parameters from ultraspectral IR measurements, *J. Atmos. Sci.*, **64**, 969– 982.

WMO (1953), *World Distribution of Thunderstorm Days*, WMO No. **21**, TP. 6 and supplement.